UCLouvain

epl

École polytechnique de Louvain

First-principles modelling of WTe_2 and graphene/WTe_2 bilayer heterostructures

Author: **Benjamin LIEGEOIS**
Supervisors: **Jean-Christophe CHARLIER, Simon DUBOIS**
Readers: **Jean-Christophe CHARLIER, Simon DUBOIS, Benoit HACKENS**
Academic year 2018–2019
Master [120] in Physical Engineering

Abstract

In this dissertation, the structural, electronic, topological and spin-related properties of monolayer WTe_2 and WTe_2/graphene bilayer heterostructures are investigated theoretically. Monolayer WTe_2 is a layered transition metal dichalcogenide with a distinctive highly anisotropic atomic structure which was recently confirmed as a quantum spin Hall material. It was further shown to display gate-tunable low-density superconductivity as well as non-trivial geometric properties and is predicted to feature high spin-orbit coupling and non-trivial spin-textures. The interplay between these outstanding properties might be of great interests in various fields such as quantum computation, spintronics or dissipationless electronic devices. A natural question is whether one can transfer these properties to other layered materials by forming Van der Waals heterostructures. In particular, WTe_2/graphene bilayers offer the prospect of proximity-induced spin-orbit coupling in graphene. This could effectively lead to non-trivial spin-textures and topological phases in this material, which would offer great perspectives for the integration of graphene in spin-based electronics.

In particular, this thesis sheds light on the most stable structural phase adopted by monolayer WTe_2 in free-standing conditions. It further predicts a giant spin-orbit proximity effect in graphene, which displays sizable anisotropy and largely preserves the linear semimetallic behaviour. Moreover, computations reveal the presence of an electric dipole moment in the bilayer heterostructure, which should affect spin-textures in the structure and provide a way to control them via electric means. Although these findings certainly require further confirmation, this investigation also potentially suggests that monolayer WTe_2 induces a canted spin-texture in the conduction bands of the Dirac cone as well as a topological phase in graphene.

Acknowledgments

First, I would like to thank my supervisors Prof. Jean-Christophe Charlier and Simon M.-M. Dubois for their precious guidance throughout this project. In addition to learning a lot from their expertise in the field, I truly enjoyed our discussions and they made this thesis a thoroughly pleasant and interesting experience. I would also like to thank Aurélie Champagne, Guillaume Brunin and Matteo Giantomassi for taking the time to answer many of the questions that puzzled me throughout this project. Finally, I would like to thank Prof. Benoit Hackens in advance for taking the time to read this dissertation.

Computational resources have been provided by the supercomputing facilities of the Université catholique de Louvain (CISM/UCL) and the Consortium des Équipements de Calcul Intensif en Fédération Wallonie Bruxelles (CÉCI) funded by the Fond de la Recherche Scientifique de Belgique (F.R.S.-FNRS) under convention 2.5020.11. The present research also benefited from computational resources made available on the Tier-1 supercomputer of the Fédération Wallonie-Bruxelles, infrastructure funded by the Walloon Region under the grant agreement n°1117545.

Contents

1. Introduction

1.1. Introduction and motivation.

One of the great successes of condensed matter physics was the description of electrons in crystalline solids through their classical energy-momentum dispersion relation or band structures. This has in particular allowed the distinction between metals, insulators as well as semiconductors and sufficed to generate much of the technology used today in electronics and optoelectronics. This picture is nevertheless highly incomplete and generally only captures a tiny fraction of the potential offered by the solid state when it does not fail to describe it entirely.

First, the quantum nature of electrons in solids implies that a complete description of their state is only captured by their so-called wavefunction. Whereas the dispersion relation only accounts for the energy and momentum associated with the latter, the wavefunction displays a myriad of other properties of fundamental interest. A crucial topic in modern condensed matter physics is the study of the global (or topological) properties of the wavefunction. When non-trivial, these features give rise to exotic phases of matter such as the quantum spin Hall state and topological insulators. These phases exhibit robust edge states which oftentimes display protected transport, offering for instance great perspectives for the realization of dissipationless devices. Equally important is a local property of the wavefunction called the Berry curvature, which is at the heart of the mechanisms responsible for a wide range of phenomena.

Second, the underlying assumption of the band structure picture is the absence of interaction. Yet, interactions between electrons are decisive to explain the occurrence of phases of matter in which electronic correlations play an important role. A shining example of such phases is the superconducting phase. Although there are ways around this problem to fall back to the dispersion relation description of superconductors, these rely on assumptions that may not be valid for more unconventional superconductors.

Finally, although relativistic corrections to the classical picture of solids are supposedly very small, the consequences of the relativistic nature of our universe on electrons in solids are critical to our understanding of the underlying physics of an important number of phenomena. They have known an increasing interest with the discovery of topological insulators and the prospects offered by spin-based electronics or spintronics, a new paradigm of electronics based on the manipulation of the electron spin rather than its charge. The principles of relativity imply that electrons moving in an electrostatic potential experience a magnetic field coupling their spin to their motion. Referred to as spin-orbit coupling (SOC throughout this report), this phenomenon allows the manipulation of spin via electric means, providing a perfect tool for the realization of spintronics.

Given these considerations, it is interesting to ask whether one can find materials whose underlying physics cannot be entirely described through classical band diagrams. In particular, the recent discovery of graphene has opened the door to the exploration of layered materials, which can be thinned down to a single atomic layer. In addition to their intrinsic extreme compact nature and the fact that these materials often exhibit outstanding properties, stacking layers of several of these atomically-thin materials into so-called Van-der-Waals heterostructures offers the possibility to combine their features at will, partially realizing the long-time dream of Richard Feynman expressed in his famous lecture "There's Plenty of Room at the Bottom". A wide family of so-called 2D materials has attracted much interest in recent years for their mechanical, optical and electronic properties: transition metal dichalcogenides (TMDs throughout this report). These compounds all feature strong SOC, many of them display superconductivity and they may well constitute the future of electronics and optoelectronics altogether.

Yet, one TMD stands out: WTe_2. To begin with, this compound naturally possesses a strongly anisotropic crystalline structure distinct from that of other TMDs in its monolayer form. More, not only did recent experimental evidence for the quantum spin Hall state in monolayer WTe_2 at record high temperature link the fields of two-dimensional materials and topological physics, the presence of gate-tunable superconductivity was also confirmed experimentally. Although highly sought after, the simultaneous natural occurrence of topology and correlations in a single layered material is unprecedented. The intersection of superconductivity and topological insulators hosts a fertile landscape of interesting quantum phenomena, including elementary excitations of the system known as non-Abelian anyons (often referred to as Majorana fermions), which offer high prospects for the realization of robust quantum computation. Whereas the realization of the quantum spin Hall state has demonstrated the nontrivial topology of the electron wavefunctions of monolayer WTe_2, the geometrical properties of the wavefunction, such as the Berry curvature, have recently been shown to be non-trivial as well. Moreover, the compound is predicted to feature strong spin-orbit coupling, non-trivial spin textures and outstanding magnetotransport properties. This exceptional combination of topology, geometry, correlations and non-trivial relativistic phenomena establish monolayer WTe_2 as a prototype material to study novel physics which cannot be described through the classical band diagram picture.

Of course, graphene itself offers tremendous fundamental and technological prospects. Beyond the wonder of the mere existence of atomically-thick materials, its fascinating attributes such as relativistic electrons with ultra-high mobilities, transparency and unmatched mechanical strength position it as a key material of the future. Moreover, graphene's low spin-orbit coupling allows the preservation of the electron spin over great distances, establishing it as a perfect platform for spin transport. Further enabling the manipulation of the spin state of electrons in graphene would however offer the possibility to make graphene-only spintronic devices, making manufacturing much easier while allowing the use of graphene's exceptional properties. Hence, it is of crucial importance to investigate whether one can import properties such as spin-orbit coupling or topological features in graphene - for example through its stacking on TMDs.

Hence, while the exploration of graphene/WTe_2 heterostructures naturally triggers fundamental interest, it also offers great hopes for the integration of graphene in spintronics. Furthermore, recent experimental evidence have established WTe_2 as an outstanding platform to study the interplay between topology, geometry, non-trivial spin textures and superconductivity. Besides, WTe_2 offers great prospects with regards to the realization of quantum computation, dissipationless transport as well as spin-based electronics. All these reasons motivate the study of monolayer WTe_2 and graphene/WTe_2 heterostructures, which constitute the subject of this study.

1.2. Aim

This thesis aims at investigating WTe_2 and WTe_2/graphene heterostructures from an ab initio perspective. In particular, this study will focus on the investigation of structural, electronic, topological and spin-related properties of these materials and structures as well as computational aspects of their modelling.

1.3. Outline

After establishing the theoretical background needed to understand the basics of spin-orbit coupling phenomena and quantum spin Hall states, this work first reviews in more detail some of the key features of graphene, TMDs and WTe_2 and the various relevant heterostructures already investigated in prior studies. Then follows the presentation and discussion of the first-principle investigations of this study. Finally, some concluding remarks are provided.

2. Background

2.1. Symmetries and degeneracies

Symmetries are crucial to the understanding of phenomena involving spin-orbit coupling. Two symmetries in particular play a central role in these considerations, namely time-reversal symmetry and inversion symmetry. This section focuses more specifically on their effect on spin-resolved energy diagrams and derives central results concerning the degeneracies that are implied by their presence.

2.1.1 Time-reversal symmetry

Let us define a system with time-reversal symmetry from $U(t)\Theta = \Theta U(-t)$ where $U(t) = e^{-iHt/\hbar}$ is the time-evolution operator and Θ the time-reversal operator. For infinitesimal evolution $U(\delta t) \approx 1 - iH\delta t/\hbar$, which leads to $-iH\Theta = \Theta iH$. Wigner's theorem states that operators preserving the absolute value of the inner product are either unitary or antiunitary. Requiring that H be bounded from below imposes for Θ to be antiunitary [1]. One can therefore write Θ in the form $\Theta = U_T K$ where U_T is unitary and K is a complex conjugation operator $Kz = z^*K\ \forall z \in \mathbb{C}$ (antilinearity) such that $H\Theta = \Theta H$.

In particular, inner products and matrix elements involving Θ satisfy the following relations

$$\langle \Theta\alpha|\Theta\beta\rangle = \langle\beta|\alpha\rangle = \langle\alpha|\beta\rangle^* \text{ and } \langle\beta|\mathcal{A}|\alpha\rangle = \langle\Theta\alpha|\Theta\mathcal{A}^\dagger\Theta^{-1}|\Theta\beta\rangle \tag{1}$$

Proof. Assuming a basis $\{|n\rangle\}$ of the relevant Hilbert space such that $K|n\rangle = |n\rangle$, one can write

$$|\Theta\alpha\rangle = U_T K\left(\sum_n |n\rangle\langle n|\right)|\alpha\rangle = \sum_n \langle n|\alpha\rangle^* U_T|n\rangle \Rightarrow \langle\Theta\beta| = \sum_m \langle m|\beta\rangle\langle m|U_T^\dagger$$

$$\Rightarrow \langle\Theta\beta|\Theta\alpha\rangle = \sum_{m,n}\langle m|U_T^\dagger U_T|n\rangle\langle\alpha|n\rangle\langle m|\beta\rangle = \sum_{m,n}\delta_{m,n}\langle\alpha|n\rangle\langle m|\beta\rangle = \langle\alpha|\beta\rangle = \langle\beta|\alpha\rangle^*$$

Defining $|\gamma\rangle \equiv \mathcal{A}^\dagger|\beta\rangle$, one finds, using the preceding argument

$$\langle\beta|\mathcal{A}|\alpha\rangle = \langle\gamma|\alpha\rangle = \langle\Theta\alpha|\Theta\gamma\rangle = \langle\Theta\alpha|\Theta\mathcal{A}^\dagger|\beta\rangle = \langle\Theta\alpha|\Theta\mathcal{A}^\dagger\Theta^{-1}|\Theta\beta\rangle$$

□

The action of Θ on spinless states/wavefunctions can be deduced as follows (using antilinearity)

$$\Theta|\psi\rangle = \Theta\int d^3r\,|\mathbf{r}\rangle\langle\mathbf{r}|\psi\rangle = \int d^3r\,|\mathbf{r}\rangle\langle\mathbf{r}|\psi\rangle^* \Rightarrow \langle\mathbf{r}|\Theta|\psi\rangle = \langle\mathbf{r}|\psi\rangle^* \Leftrightarrow \psi(\mathbf{r}) \xrightarrow{\Theta} \psi^*(\mathbf{r})$$

This can be interpreted as $\mathbf{k} \xrightarrow{\Theta} -\mathbf{k}$ for Bloch states (assuming non-degeneracy) [2]

$$T_{\mathbf{R}}\psi^*_{n\mathbf{k}}(\mathbf{r}) = T_{\mathbf{R}}\psi^*_{n\mathbf{k}}(\mathbf{r}+\mathbf{R}) = e^{-i\mathbf{k}\cdot\mathbf{R}}\psi^*_{n\mathbf{k}}(\mathbf{r}) \Rightarrow \psi^*_{n\mathbf{k}}(\mathbf{r}) = \psi_{n,-\mathbf{k}}(\mathbf{r})$$

Similarly, the action on two-spinors (spin-1/2) is given by [1]

$$\Theta = -i\sigma_y K = \begin{pmatrix} 0 & -1 \\ 1 & 0 \end{pmatrix} K$$

where σ_y is the second Pauli matrix.

Proof. Considering the angular momenta operators as the generators of rotations, one has that the eigenstates of the spin operator component along $\hat{n}$ can be expressed in terms of the spin up eigenstate along $\hat{z}$ as follows

$$|\hat{n}+\rangle = e^{-i\phi S_z/\hbar}e^{-i\theta S_y/\hbar}|+\rangle \text{ and } |\hat{n}-\rangle = e^{-i\phi S_z/\hbar}e^{-i(\theta+\pi)S_y/\hbar}|+\rangle$$

Spin is an angular momentum, it should thus be odd under time-reversal $\Theta\mathbf{S}\Theta^{-1} = -\mathbf{S}$, which implies $\Theta e^{-iS_\alpha}\Theta^{-1} = e^{-iS_\alpha}$ (complex conjugation compensates the sign change). Using the latter property and the corresponding transformation of eigenstates, one finds

$$\begin{aligned}
\Theta|\hat{n}+\rangle = |\hat{n}-\rangle \quad &\Leftrightarrow \quad \Theta e^{-i\phi S_z/\hbar}e^{-i\theta S_y/\hbar}|+\rangle = e^{-i\phi S_z/\hbar}e^{-i(\theta+\pi)S_y/\hbar}|+\rangle \\
&\Leftrightarrow \quad \Theta e^{-i\phi S_z/\hbar}\Theta^{-1}\Theta e^{-i\theta S_y/\hbar}\Theta^{-1}\Theta|+\rangle = e^{-i\phi S_z/\hbar}e^{-i(\theta+\pi)S_y/\hbar}|+\rangle \\
&\Leftrightarrow \quad \Theta|+\rangle = e^{-i\pi S_y/\hbar}|+\rangle = e^{-i\pi S_y/\hbar}(K|+\rangle) = -i\sigma_y K|+\rangle \\
&\Rightarrow \quad \Theta = -i\sigma_y K
\end{aligned}$$

Note that the presence of K is necessary for Θ to be antiunitary. □

For spin-1/2 Bloch states, this translates to [2]

$$\Theta\begin{pmatrix}\psi_{\mathbf{k}\uparrow}\\ \psi_{\mathbf{k}\downarrow}\end{pmatrix} = \begin{pmatrix}-\psi^*_{\mathbf{k}\downarrow}\\ \psi^*_{\mathbf{k}\uparrow}\end{pmatrix} \text{ with } \Theta^2 = -1$$

The presence of time-reversal symmetry in a system implies the so-called Kramers degeneracy between time-reversal conjugate states

$$\begin{cases}[H,\Theta] &= 0\\ H|\psi\rangle &= \epsilon|\psi\rangle\end{cases} \Rightarrow \begin{cases}\langle\psi|\Theta\psi\rangle &= 0\\ H(\Theta|\psi\rangle) &= \Theta H|\psi\rangle = \epsilon(\Theta|\psi\rangle)\end{cases} \Leftrightarrow \begin{cases}\epsilon_{\Theta\psi} &= \epsilon_\psi\\ \Theta\psi &\perp \psi\end{cases}$$

Proof. Orthogonality is directly obtained from (1) and $\Theta^2 = -1$ as $\langle\psi|\Theta\psi\rangle = \langle\Theta\Theta\psi|\Theta\psi\rangle = -\langle\psi|\Theta\psi\rangle$ □

For spin-polarized Bloch states, this naturally implies

$$\epsilon_{n\mathbf{k}\uparrow} = \epsilon_{n-\mathbf{k}\downarrow} \tag{2}$$

2.1.2 Inversion symmetry

Inversion symmetry π can be defined from its action on position eigenstates

$$\pi|\mathbf{r}\rangle \equiv |-\mathbf{r}\rangle$$

In particular, it commutes with the lattice translation operator $T_{\mathbf{R}}$

$$T_{\mathbf{R}}\pi|\mathbf{r}\rangle = T_{\mathbf{R}}|-\mathbf{r}\rangle = |-\mathbf{r}+\mathbf{R}\rangle = \pi|+\mathbf{r}-\mathbf{R}\rangle = \pi T_{-\mathbf{R}}|\mathbf{r}\rangle \Rightarrow T_{\mathbf{R}}\pi = \pi T_{-\mathbf{R}}$$

Its action on Bloch states can be found as follows

$$T_{\mathbf{R}}(\pi|\psi_{n\mathbf{k}}\rangle) = \pi T_{-\mathbf{R}}|\psi_{n\mathbf{k}}\rangle = e^{-i\mathbf{k}\cdot\mathbf{R}}(\pi|\psi_{n\mathbf{k}}\rangle) \Rightarrow (\pi|\psi_{n\mathbf{k}}\rangle) = |\psi_{n-\mathbf{k}}\rangle \Leftrightarrow \mathbf{k} \xrightarrow{\pi} -\mathbf{k}$$

In particular, a system with inversion symmetry $[\pi, H] = 0$ satisfies

$$\epsilon_{n\mathbf{k}s} = \epsilon_{n-\mathbf{k}s} \tag{3}$$

Proof.

$$[H,\pi]|\psi_{\mathbf{k}}\rangle = H\pi|\psi_{\mathbf{k}}\rangle - \pi H|\psi_{\mathbf{k}}\rangle = H|\psi_{-\mathbf{k}}\rangle - \epsilon_{\mathbf{k}}\pi|\psi_{\mathbf{k}}\rangle = (\epsilon_{-\mathbf{k}} - \epsilon_{\mathbf{k}})|\psi_{-\mathbf{k}}\rangle = 0 \;\forall\mathbf{k}\in\mathcal{B}_1$$

On Bloch wavefunctions, inversion symmetry acts as □

$$\pi\psi_{n\mathbf{k}}(\mathbf{r}) = \psi_{n-\mathbf{k}}(\mathbf{r}) = \psi_{n\mathbf{k}}(-\mathbf{r}) \text{ and } \pi u_{n\mathbf{k}}(\mathbf{r}) = u_{n-\mathbf{k}}(\mathbf{r}) = u_{n\mathbf{k}}(-\mathbf{r}) \tag{4}$$

where u denotes the lattice-periodic part of the Bloch state.

Proof. In addition to being unitary ($\pi^2 = \mathbb{I}$), the parity operator is also Hermitian

$$\langle \mathbf{r}'|\pi|\mathbf{r}\rangle = \langle \mathbf{r}'|-\mathbf{r}\rangle = \delta(\mathbf{r}'+\mathbf{r}) = \langle -\mathbf{r}|\mathbf{r}'\rangle = \langle \mathbf{r}'|\pi|\mathbf{r}\rangle^*$$

This leads directly to

$$\langle \mathbf{r}|\pi|\psi_{n\mathbf{k}}\rangle = \langle \mathbf{r}|\psi_{n-\mathbf{k}}\rangle = \langle -\mathbf{r}|\psi_{n\mathbf{k}}\rangle$$

which yields the desired result. The same relations naturally holds for $u_{n\mathbf{k}}$. □

Unitarity $\pi^2 = \mathbb{I}$ implies that there is only two observable values (eigenvalues) of parity $\zeta = \pm 1$, which correspond respectively to even and odd states

$$\pi\,|\psi\rangle = \pm 1\,|\psi\rangle \Leftrightarrow \langle \mathbf{r}|\pi|\psi\rangle = \pm\,\langle \mathbf{r}|\psi\rangle \Leftrightarrow \pm\,\langle -\mathbf{r}|\psi\rangle = \langle \mathbf{r}|\psi\rangle$$

2.1.3 Two-fold degeneracy and time-reversal invariant momenta

In the presence of both time-reversal and space inversion symmetries, one finds, combining (2) and (3)

$$[H,\pi] = [H,\Theta] = 0 \Rightarrow \epsilon_{n\mathbf{k}s} = \epsilon_{n-\mathbf{k}-s} = \epsilon_{n\mathbf{k}-s}$$

When inversion symmetry is absent, this two-fold degeneracy is preserved at time-reversal-invariant momenta, which shall be referred to as TRIMs.

$$\text{TRIMs} \equiv \{\mathbf{k} \mid \mathbf{k} = -\mathbf{k} + \mathbf{G}\} \Rightarrow \forall \mathbf{k} \in \text{TRIMs},\ \epsilon_{n\mathbf{k}s} = \epsilon_{n-\mathbf{k}-s} = \epsilon_{n-\mathbf{k}+\mathbf{G}-s} = \epsilon_{n\mathbf{k}-s}$$

Hence, a time-reversal symmetric system displays crossing spin up and down bands at TRIMs. Figure 1 illustrates the presence of this two-fold degeneracy for time-reversal symmetric systems in the presence and absence of inversion symmetry.

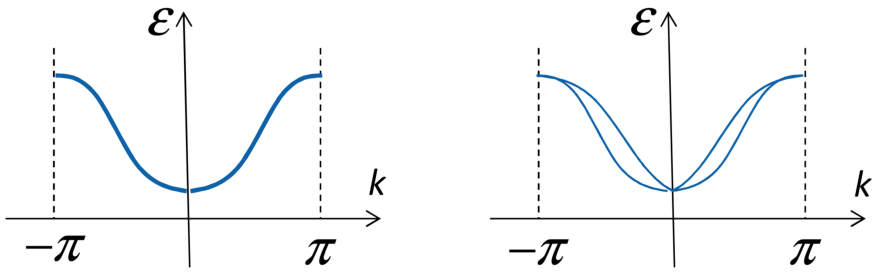

Figure 1: Two-fold degeneracy in a 1D system with a unit lattice constant. (Right) The presence of time-reversal symmetry ensures crossing (*i.e.* two-fold degeneracy) of spin up and spin down bands at time-reversal momenta $\{0, \pm\pi\}$ and symmetry between positive and negative momenta. (Left) Adding space inversion symmetry guaranties two-fold degeneracy over the whole Brillioin zone.

2.2. Spin-orbit coupling

Spin-orbit coupling is central to this dissertation. In this section, a brief review of the nature, strength and consequences of this effect is provided. Additionally, a common type of spin-orbit coupling is presented.

Spin-orbit coupling. On the atomic level, spin-orbit coupling (SOC) arises as a relativistic correction stemming from the effective magnetic field felt by electrons with a non-zero angular momentum moving in the electrostatic potential created by an atomic nucleus, which naturally couples to its spin [3]. In general, any moving charge with spin in an electrostatic potential experiences this effect. The microscopic form of this correction is given by

$$H_{SO} = \frac{1}{4m_e c^2}(\nabla V \times \mathbf{p}) \cdot \mathbf{S}$$

The case of a spherically-symmetric potential V makes explicit the fact that spin-orbit coupling couples angular momentum and spin.

$$H_{SO} = \left(\frac{1}{4m_e c^2}\frac{1}{r}\frac{dV}{dr}\right) \mathbf{L}\cdot\mathbf{S} \text{ where } \mathbf{L} = \mathbf{r}\times\mathbf{p}$$

Strength. The strength of this effect in atoms and solids is generally found to be proportional to the fourth power of the atomic number of the ions, *i.e.* $H_{SO} \propto Z^4$ [4].

Effects. Because this coupling depends explicitly on spin, it generally allows the lifting of spin degeneracy. In addition, the presence of SOC implies that the spin polarization $\langle\mathbf{S}\rangle$ varies with the direction of $\nabla V \times \mathbf{p}$, and in particular with crystal momentum $\mathbf{k}$. In particular, this implies that the spin polarization is a vector field in momentum space. Representations of this field are called spin-textures.

Rashba SOC. Different symmetries (for V) allow different types of spin-orbit coupling. A particular common case in two-dimensional solids is the presence of a broken out-of-plane inversion symmetry, *i.e.* $z \to -z$ asymmetry. This is in particular the case in asymmetric quantum wells, in layered materials deposited on substrates or in the presence of out-of-plane electrical fields. The SOC associated with this type of configuration is called Rashba SOC [5,6] and is typically of extrinsic nature. In toy Hamiltonians, it often takes the form

$$H_{\mathrm{R}} = \alpha(\boldsymbol{\sigma}\times\mathbf{k})\cdot\hat{z}$$

where α is the Rashba coupling and is typically proportional to the field strength E_z in the presence of an out-of-plane electric field. According to this expression, when Rashba SOC is dominant, spin-configurations with exclusively in-plane components perpendicular to pseudo-momentum have the lowest energy. Additionally, it should induce momentum-dependant ($\propto k$) band splittings for opposite spins. This type of configuration is illustrated in momentum space in figure 2.

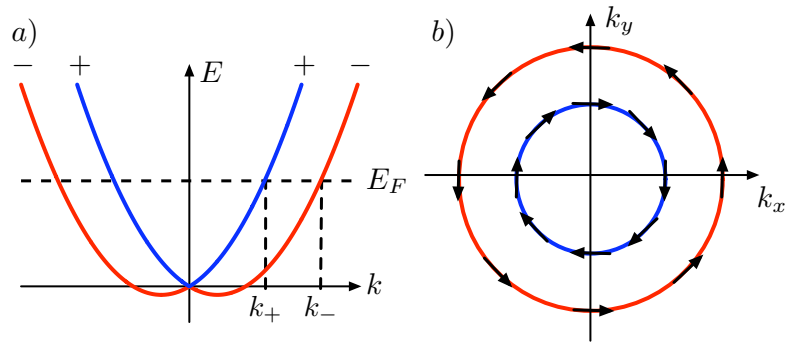

Figure 2: Illustration of typical (a) band splitting and (b) associated spin-texture induced by Rashba SOC.

2.3. The quantum spin Hall state.

Given the fact that a more thorough review of some of the theory (within the framework of topological band theory) and phenomenology of two-dimensional topological insulators was the subject of previous work, a brief summary of the main results needed to understand these phases of matter is given here.

Topological equivalence of insulating electronic phases within the framework of topological band theory. Two band insulators characterized by two (bulk) Bloch Hamiltonians $H_1(\mathbf{k})$ and $H_2(\mathbf{k})$ are said to be topologically equivalent if the latter can be mapped continuously (through arbitrary continuous perturbations) onto each other without closing the gap of the associated band structure. Symmetry-protected

topological equivalence is defined similarly with the additional constraint that a particular symmetry be preserved (time-reversal symmetry throughout this report) [7]. Topological equivalence classes are characterized by topological invariants that are insensitive to perturbations that continuously preserve the presence of the gap (while preserving a given symmetry in the case of symmetry-protected topological phases). These topological invariants are global properties of the electronic wavefunction.

Bulk-boundary correspondence. An interface between two materials or between a material and the void may be thought as a continuous deformation of the (local) Bloch Hamiltonian. If this interface distinguishes topologically distinct insulating phases of matter, the gap must close at some point along the interface according to our definition of topological equivalence. Hence, the interface should host metallic states - referred to as edge states in two-dimensional systems - as long as the phases across the interface have distinct topological invariants. This feature makes these edge states robust against small perturbations preserving the gap (and a given symmetry). Since one can deduce the presence of edge states from topological properties of the bulk, this principle is referred to as bulk-boundary correspondence [7] and is illustrated in figure 3.

Quantum spin Hall state. The so-called quantum Spin Hall state is a topological insulating two-dimensional electronic phase protected by time-reversal symmetry and characterized by the so-called $\mathbb{Z}_2$-invariant. The latter only takes two values: 0 and 1, corresponding respectively to the trivial and topological phases. The presence of time-reversal symmetry ensures that edge states come in time-reversal pairs [8], referred to as helical edge states. Since time-reversal symmetry reverses both spin and crystal momentum, this implies that opposite spins in these helical edge states have opposite crystal momenta, enabling the possibility of net (and potentially pure) spin currents [9,10], which may be very interesting from a technological point of view. It can also be shown that time-reversal symmetry protects these edge states from backscattering, a feature potentially paving the way for low-dissipation devices. The sole observation of these edge states in transport measurements should hence lead to a quantized conductance twice that of the quantum Hall effect. Transport-based applications at room temperature would however require the presence of a large bandgap in order to effectively suppress bulk conduction and observe exclusively the outstanding properties of the boundary modes. In particular, room-temperature transport measurements of the edge states associated with the quantum spin Hall state have not yet been realized experimentally. Note that a signature of protection by time-reversal symmetry is the effective suppression of the edge states in the presence of a magnetic field.

Band inversion. The basic mechanism behind the non-trivial band topology in the quantum spin Hall state is the band inversion between two orbital bands, which can in particular be driven by spin-orbit coupling [11]. Typically, a gap is created by spin-orbit coupling between two (or more) bands that would otherwise (in the absence of SOC) be crossing (or close in energy) at a particular point in the first Brilloin zone, as illustrated in figure 3. Note that the crossing might occur at an intermediate point in the perturbative process. Nevertheless, the occurrence of the quantum spin Hall state is hence often accompanied by the presence of strong spin-orbit coupling, which might make a number of those two-dimensional topological insulators attractive for spintronics applications.

Experimental realization of the quantum spin Hall state. Only a few materials and material structures have been shown to exhibit the quantum spin Hall state. The first realizations were obtained in HgTe [12,13] and InAs/GaSb [14,15] quantum wells at very low temperatures. A number of alternative platforms were subsequently discovered, including bismuthene on a SiC substrate [16], the layered compound $Bi_{14}Rh_3I_9$ [17] and graphene decorated with $BiSe_3$ nanoparticles (where $BiSe_3$ is a well known three-dimensional topological insulator). Observation of the hallmarks of the quantum spin Hall state in these systems is however difficult either due to complex geometry, the buried nature of the interface systems (*e.g.* in quantum wells), the strong substrate interactions (*e.g.* in Bi-based surface systems [16,18]), the extremely low temperatures required or the significant material engineering needed to synthesize them.

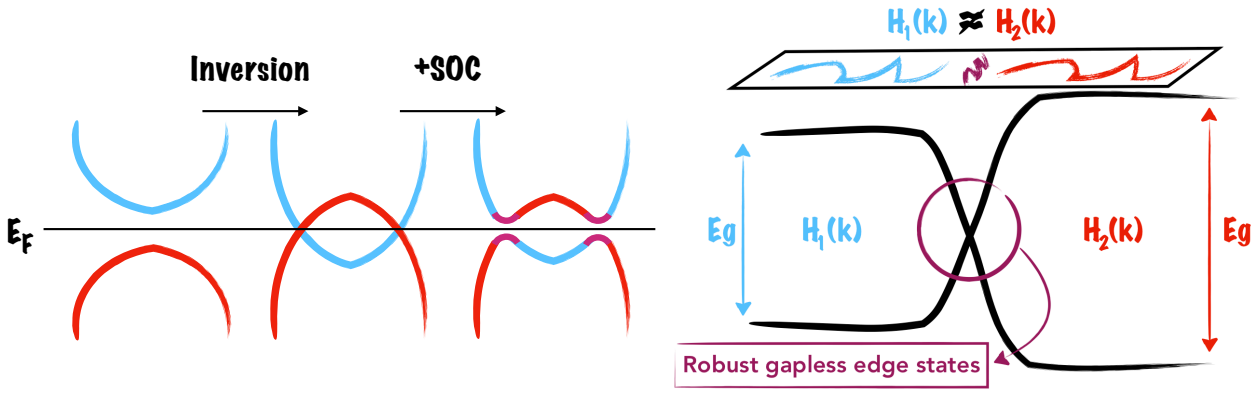

Figure 3: (Left) Illustration of the band inversion mechanism leading to quantum spin Hall states. Following a reversal of the band ordering, SOC creates a gap at the Fermi level which leads to a topological phase. (Right) Illustration of the concept of bulk-boundary correspondence. From the definition of topological equivalence, the interface between two topologically-inequivalent insulating phases hosts robust gapless modes.

Majorana fermions. Majorana fermions in solid state physics are zero-energy boundary modes predicted to appear at the interface between topological insulators and superconductors [19–22]. The name fermion is somewhat misleading given the fact that these excitations can feature non-Abelian statistics in two dimensions, different from that of fermions or bosons. This stems from the fact that the braiding group is non-trivial in bidimensional systems, meaning that exchanging two identical quasiparticles leads to an inequivalent configuration. Therefore exchanging these topologically-protected pseudoparticles through electrical means (commonly referred to as *braiding* in reference to the formation of braids in spacetime) provides a way to encode information non-locally, which is thought to offer great prospects with respect to the realization of fault-tolerant quantum computing [23].

2.4. Graphene

In this section, a brief review of the main structural, electronic and spin-related features of graphene is provided. In particular, graphene is a monolayer sp^2-hybridized carbon honeycomb lattice. The remaining p_z orbitals perpendicular to the plane overlap to form a system of delocalized conducting π electrons which are shown to display linear dispersion close to the Fermi level. Finally, graphene hosts exceptionally small spin-orbit coupling.

Crystalline structure. Graphene has point group $P6/mmm$, which is centrosymmetric. The honeycomb lattice is not a Bravais lattice. Therefore, graphene must be described in terms of two equivalent sublattices effectively related through parity. These sublattice are represented in yellow and blue in figure 4 and shall be labelled respectively by A and B. Let δ_i denote the vectors connecting nearest neighbours and a their length. Aligning the x axis with δ_i, a suitable choice for the primitive lattice vectors $\mathbf{a}_{1,2}$ and the corresponding reciprocal lattice vectors $\mathbf{b}_{1,2}$ is found as

$$\begin{cases} \mathbf{a}_{1,2} &= \dfrac{\sqrt{3}a}{2} & (\sqrt{3}, \pm 1) \\ \mathbf{b}_{1,2} &= \dfrac{2\pi}{3a} & (1, \pm\sqrt{3}) \\ \pm\mathbf{K} &= \dfrac{2\pi}{3a} & \left(1, \pm\dfrac{1}{\sqrt{3}}\right) \end{cases}$$

where $\pm K$ are the two (inequivalent) corners of the first Brillioin zone displayed in figure 4.

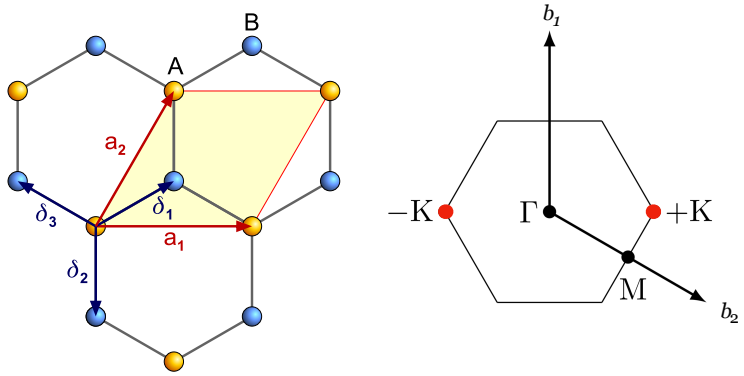

Figure 4: (Left) Honeycomb lattice and its primitive cell, containing one atom of each sublattice A (yellow) and B (blue). (Right) Two-dimensional first Brilloin zone of the honeycomb lattice with highlighted high-symmetry points.

Low-energy theory and emergence of Dirac fermions. Considering only nearest-neighbour hopping for spinless π electrons, the following tight-binding Hamiltonian is obtained in second quantization formalism

$$H = -t \sum_{\langle \mathbf{R}A, \mathbf{R}'B \rangle} \left(a_A^\dagger(\mathbf{R}) a_B(\mathbf{R}') + h.c. \right) = -t \sum_{\mathbf{R}} \left(a_A^\dagger(\mathbf{R}) a_B(\mathbf{R}) + a_A^\dagger(\mathbf{R}) a_B(\mathbf{R} - \mathbf{a}_1) + a_A^\dagger(\mathbf{R}) a_B(\mathbf{R} - \mathbf{a}_2) + h.c. \right)$$

where $\mathbf{R}$ and $\mathbf{R}'$ identify specific unit cells and $\langle \cdot, \cdot \rangle$ denotes nearest-neighbour atomic sites. $a_A^\dagger(\mathbf{R})$ is the fermionic creation operator in the Wannier basis associated with the A sublattice in unit cell $\mathbf{R}$ and $a_B(\mathbf{R})$ the corresponding annihilator associated with sublattice B. Additionally, $h.c.$ stands for Hermitian conjugate. The Wannier basis and the Bloch basis are related by a Fourier transform.

$$\begin{cases} a_A^\dagger(\mathbf{R}) & \equiv & \dfrac{1}{\sqrt{N}} \displaystyle\sum_{\mathbf{k}} e^{-i\mathbf{k}\cdot\mathbf{R}} a_{\mathbf{k},A}^\dagger \\ a_B(\mathbf{R}) & \equiv & \dfrac{1}{\sqrt{N}} \displaystyle\sum_{\mathbf{k}'} e^{+i\mathbf{k}'\cdot\mathbf{R}} a_{\mathbf{k},B} \end{cases}$$

Using this relation, one finds the following form for the Hamiltonian

$$\Rightarrow \quad H = -\frac{t}{N} \sum_{\mathbf{R}} \sum_{\mathbf{k}\mathbf{k}'} \left(\gamma^*(\mathbf{k}) e^{i(\mathbf{k}-\mathbf{k}')\cdot\mathbf{R}} a_{\mathbf{k},A}^\dagger a_{\mathbf{k}',B} + h.c. \right) = -t \sum_{\mathbf{k}\mathbf{k}'} \left(\gamma^*(\mathbf{k}) \frac{1}{N} \left[\sum_{\mathbf{R}} e^{i(\mathbf{k}'-\mathbf{k})\cdot\mathbf{R}} \right] a_{\mathbf{k},A}^\dagger a_{\mathbf{k},B} + h.c. \right)$$

$$= -t \sum_{\mathbf{k}} \left(\gamma^*(\mathbf{k}) a_{\mathbf{k},A}^\dagger a_{\mathbf{k},B} + h.c. \right) = \sum_{\mathbf{k}} \begin{pmatrix} a_{\mathbf{k},A}^\dagger & a_{\mathbf{k},B}^\dagger \end{pmatrix} \begin{pmatrix} 0 & -t\gamma^*(\mathbf{k}) \\ -t\gamma(\mathbf{k}) & 0 \end{pmatrix} \begin{pmatrix} a_{\mathbf{k},A} \\ a_{\mathbf{k},B} \end{pmatrix} = \sum_{\mathbf{k}} h(\mathbf{k})$$

where the Bloch basis has been organised into pseudospinors for a reason that will become apparent at a later stage. Diagonalizing $h(\mathbf{k})$ gives the dispersion relation of π electrons in graphene within the first-neighbour hopping approximation

$$\epsilon(\mathbf{k}) = \pm t|\gamma(\mathbf{k})| = \sqrt{1 + 4\cos\left(\frac{3k_x a}{2}\right)\cos\left(\frac{\sqrt{3}k_y a}{2}\right) + 4\cos^2\left(\frac{\sqrt{3}k_y a}{2}\right)}.$$

The corresponding energy spectrum is displayed in figure 5.

In particular, the energy levels are degenerate at $\pm\mathbf{K}$. A Taylor expansion around those points $\mathbf{k} = \pm\mathbf{K} + \mathbf{q}$ shows that the dispersion in their vicinity is linear. The effective low-energy theory is given by

$$\mathbf{k} \approx \pm\mathbf{K} \Rightarrow \gamma(\mathbf{k}) \approx -\hbar v_F(iq_x \pm q_y) \Rightarrow H_{\text{eff}} = \hbar v_F \begin{pmatrix} 0 & -iq_x \pm q_y \\ iq_x \pm q_y & 0 \end{pmatrix} = \hbar v_F(q_x\sigma_y + \tau q_y\sigma_x),$$

where $v_F \equiv 3ta/2\hbar$, $\tau = \pm 1$ and $\sigma_{x,y}$ are the first and second Pauli matrices acting on Bloch pseudospinors. Note that the Bloch pseudospinor basis is here implicit. Interestingly, the effective Hamiltonian derived here takes the form of a two-dimensional massless Dirac Hamiltonian in which the sublattice degree of freedom in graphene has replaced the spin degree of freedom in the original Dirac equation. Hence, this degree of freedom is termed *pseudospin*. Note that an additional degree of freedom is found in τ, which identifies about which corner of the Brilloin zone the low-energy theory is derived. In particular, those points correspond to the valence band maxima and conduction band minima - also called *valleys* - at half filling since the valence and conduction bands are effectively degenerate at these points. Hence τ corresponds to the valley degree of freedom in graphene. The resulting dispersion features linear cones and should be valid close to the Fermi level as can be observed in figure 5.

Effect of spin-orbit coupling. The quantum spin Hall effect was first theorized in graphene and although zigzag graphene nanoribbons were effectively predicted to host helical edge state [24], intrinsic spin-orbit coupling in graphene is too weak [25] for such states to be experimentally realized. Indeed, due to the particularly small atomic number of carbon, spin-orbit coupling in graphene is supposedly exceptionally small, hinting at especially high spin relaxation times. Long spin relaxation lengths on the scale of μm were indeed experimentally observed at room temperature [26–30]. Intrinsic SOC in graphene, often referred to as Kane-Mele SOC, is predicted to be of the order of $\sim 10\mu eV$ [25, 31] and should open a small gap at the Dirac point and induce a small quadratic character in the band dispersion around this point. In model Hamiltonians, Kane-Mele SOC typically takes the following form

$$H_{KM} = \lambda_{KM}\tau\sigma_z s_z$$

where σ_z acts on pseudospin and s_z on spin. In particular, inducing a more robust quantum spin Hall state in graphene requires the presence of $z \to -z$ symmetric SOC, which excludes Rashba SOC [32]. Note that centrosymmetry excludes the presence of bands splittings according to section 2.1.3.

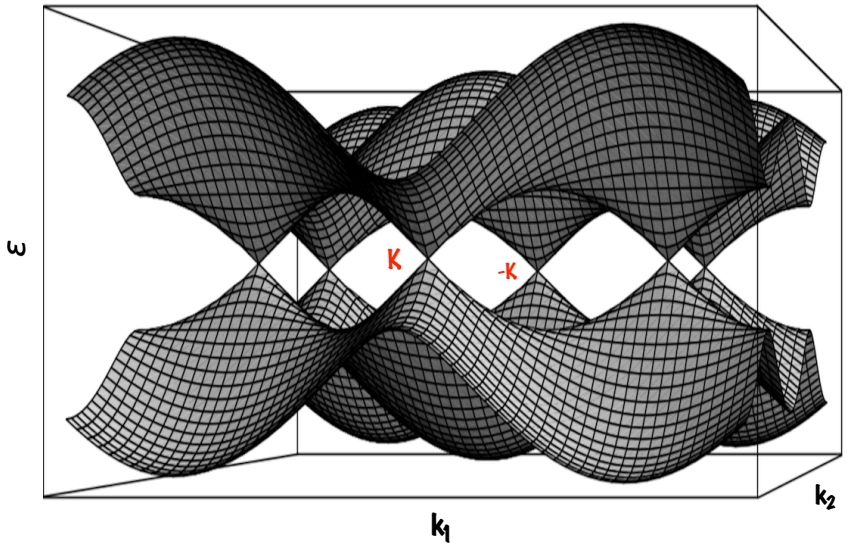

Figure 5: Energy spectrum of the π-electron system in graphene within the nearest-neighbour tight-binding formalism. Close to the Fermi level, the dispersion forms linear cones at the two inequivalent corners of the first Brilloin zone $\pm K$.

2.5. Transition metal dichalcogenides

Transition metal dichalcogenides (TMDs) are compounds of chemical formula MX_2 where M is a transition metal, *i.e.* a member of the *d*-block in Mendeleev's table, and X is a chalcogen, *i.e.* a member of the chemical group 16 (usually excluding oxygen) such as $X = (S, Se, Te)$. TMDs exhibit a unique combination of atomic-scale thickness, strong spin–orbit coupling and favourable electronic and mechanical properties, which make them interesting for fundamental studies and for applications in high-end electronics, spintronics, optoelectronics and more. In particular, this section reviews some of the key structural, electronic, topological and spin-related features of this family of materials.

Crystalline structure. Group 6 transition metals such as those with $M = (Mo, W)$ constitute an important class of materials with a layered crystal structure. These materials possess a variety of polymorphic structures in the monolayer form such as $1H$, $1T$, and $1T'$ and $1T_d$ shown in figure 6. The most studied $1H$ structure is a sandwich of three planar of triangular lattices X-M-X in an ABA hexagonal stacking configuration. In this structure, M atoms are trigonal-prismatically coordinated by six X atoms, which results in the P6m2 space-group. The two-dimensional first Brilloin zone is identical in shape to that of graphene (cfr. figure 4). An important difference with graphene is the fact that the structure breaks inversion symmetry (which corresponds to the sublattice symmetry in graphene).

The M atoms in the monolayer $1T$ structure are in contrast octahedrally coordinated with the closest six X atoms, leading to ABC stacking and the P3m1 space group. It has been known that the inversion-symmetric $1T$ structure in MX_2 is often found to be metastable in free-standing conditions and to undergo a spontaneous Peierls-like lattice distortion driven by electron-phonon interactions [33] in the x-direction to form a 2×1 superlattice structure, which results either in the inversion-symmetric $1T'$ phase or the (highly similar) inversion-breaking $1T_d$ structure, which will both be described in greater detail further along in the discussion [34]. Note that although monolayer WTe_2 has been predicted to be the only candidate of the group 6 to be more stable in the $1T'$ phase than in the $1H$ phase, computational evidence of the existence of a large ($> 1\text{eV}/MX_2$) energy barrier between $1T'$ and $1H$ suggests all TMDs considered here could be stabilized in the $1T'$ phase [35]. Since bulk WTe_2, and $MoTe_2$ crystallize in the bulk $1T_d$ phase [36] (resulting from ABA stacking of $1T_d$ monolayers into an orthorhombic unit cell), they are both naturally found through exfoliation in the monolayer-$1T'$ phase (or potentially the highly similar monolayer $1T_d$ phase). This is in contrast with other bulk TMDs, which crystallize in the bulk $2H$ structure, resulting from the ABA stacking of $1H$ monolayers. Recent evidence shows that monolayer WSe_2 has nevertheless been successfully stabilized in the $1T'$ phase [37, 38].

Electronic properties. $1T$ and $1H$-MX_2 have very different electronic properties: the former is metallic while the latter is a large direct gap semiconductor. As for the case of graphene, valence band maxima and conduction band minima in the 1H-phase occur at the two inequivalent high-symmetry points $\pm K$, leading to valley degree of freedom τ similar to that of graphene. In contrast, The $1T'$ and $1T_d$ are predicted to either be small-gap semiconductors or slightly semimetallic. [35]

Effect of spin-orbit coupling. In contrast with graphene, the simultaneous presence of non-centrosymmetry in TMD $2H$-monolayers and large spin-orbit coupling (stemming from the large atomic numbers of the transition metal) in addition to the fact that $\pm K$ are not TRIMs allows the presence of significant band splittings at those points [34]. Since these points are time-reversal conjugates, they should display opposite band splittings, allowing valley-dependant spin physics. This property is referred to as spin-valley locking or spin–valley coupling [39] and implies the immediate translation of the valley polarization of charge carriers into effective spin polarization. This intrinsic property of $2H$-TMDs may be used to design spintronic devices that do not involve magnetic materials. Analogous to the Zeeman-splitting, the dominant SOC term in $2H$-TMDs is named Valley-Zeeman SOC because the effective Zeeman fields are valley-dependent. It is very similar to Kane-Mele SOC but embodies the crucial inversion-breaking of $2H$-TMDs. In particular, Valley-Zeeman

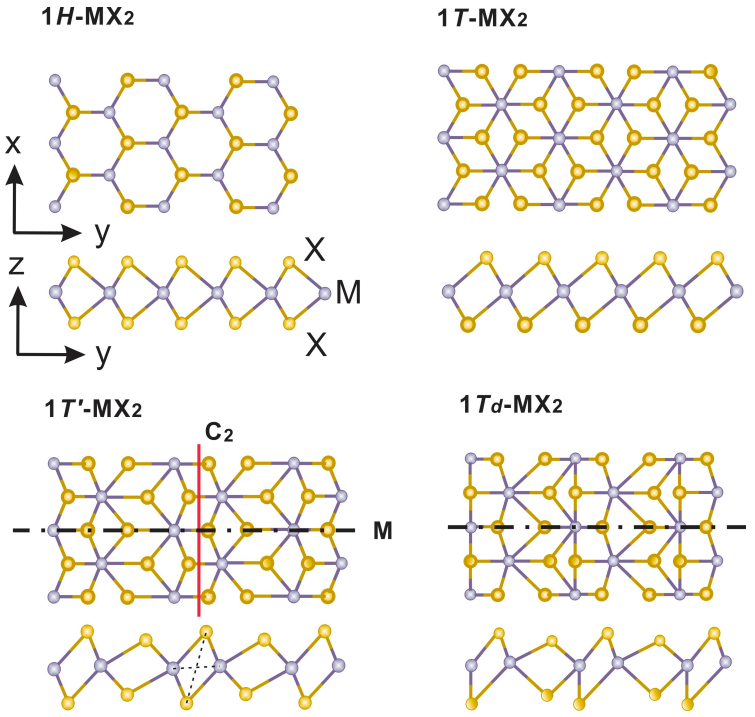

Figure 6: Illustration of the possible structural phases of group 6 monolayer TMDs. The $1T$phase is typically unstable and relaxes through a Peierls-like transition either to the $1T'$ or the $1T_d$ phase. $1H$ and $1T_d$ break inversion symmetry, they can therefore display band splittings. In contrast, $1T'$ and $1T$ are centrosymmetric, which ensures spin-degeneracy. The $1H$ phase is a large-gap semiconductor while the $1T$ phase is metallic. The $1T'$ and $1T_d$ phases are predicted to be either small-gap semiconductors or slightly semi-metallic. The $1T'$ phase (and most likely the highly similar $1T_d$ phase) is predicted to lead to quantum spin Hall states.

SOC is $z \to -z$ symmetric and typically takes the form [40]

$$H_{\mathrm{VZ}} = \lambda_{\mathrm{VZ}} \tau s_z$$

This SOC provokes the spin splitting of degenerate bands, with out-of-plane spin polarization at K and $-K$ points, and an opposite spin-splitting in different valleys. Analogous to the Zeeman-splitting, the SOC is named Valley-Zeeman SOC because the effective Zeeman fields are valley-dependent.

Topological features. Both the $1T$ and $1H$ phases are topologically trivial. [41] However, all TMDs in the $1T'$ phase are predicted to be topological [35], which has been confirmed for WTe_2 and recently for $1T'$-WSe_2 [37,38]. The latter has been reported as a large gap material hosting an in-gap edge state at the boundary. The polymorphic flexibility of monolayer WSe_2 can be used to study topological states at highly ordered phase boundaries, which significantly increases quantitative access to these states via microscopy. This is in contrast with buried systems or layered materials displaying high degree of structural disorder in their edges (such as WTe_2).

Note that, contrary to common belief, the topological nature of the $1T'$ phase in group 6 TMDs is not a result of the conventionally assumed d-p inversion, where the chalcogen (X) p_x band moves above the metal (M) d_{xy}. Rather, recent predictions show [41] that in $1T'$-MS_2 and $1T'$-MSe_2, the X-p band is pulled down below the M-d band before the topological phase transition and a p-d band inversion supposedly occurs (*i.e.* the opposite of a d-p inversion). The case of $1T'$-MTe_2 is somewhat particular because it reportedly (also) involves the inversion between two different d-bands, which is referred to as d-d band inversion.

2.6. Graphene/TMD heterostructures

This section reviews the technological interest and key features predicted to occur in graphene/TMD heterostructures.

Interest. Enabling the manipulation of electronic spin in graphene offers the possibility to make graphene-only spintronic devices, in which both control and preservation of spin are possible. While the enhancement of SOC in graphene may be realized through functionalization with adsorbates or doping with impurities, proximity effects have the advantage of potentially preserving the outstanding properties of graphene. Given their strong SOC, TMDs are naturally great candidates and therefore graphene/2H-TMD bilayer heterostructures, including graphene on MoS_2, WS_2, WSe_2 and $MoSe_2$ have been investigated intensively over the past few years, both on theoretical and experimental basis.

Strength of proximity SOC. In particular, these substrates were shown to induce large SOC in graphene. Experimental evidence for this includes the observation of the spin Hall effect at room temperature in bilayer heterostructures [42–45], which paves the way for graphene-based spin field effect transistors [46]. Further confirmation was brought by measurements of weak antilocalization [47–50], which confirm the proximity induced SOC in graphene in the range of 1 to 10 meV. Some discrepancies appear in the magnitude of the proximity-induced SOC, notably the fact that it seems to be 10 times weaker in MoS_2 than WSe_2 and WS_2 [32], indicating that tungsten-based TMDs may have a better chance at inducing large spin-orbit couplings in graphene. Similarly, bulk 2H-TMDs reportedly induce SOC 10 times weaker than their monolayer counterparts [32].

Origins and symmetries. Beyond the amplitudes, the origins and symmetries of the proximity-induced SOC in graphene are equally interesting. On the one hand, $z \to -z$ asymmetric SOC is expected in realistic experimental configurations. In particular, the observation of significant charge-to-spin conversion has been reported in these systems [51], which be traced back to the presence of strong Rashba SOC. On the other hand, $z \to -z$ symmetric SOC would pave the way for the realization of the quantum spin Hall state in graphene. Notably, weak antilocalization measurement can distinguish $z \to -z$ symmetric and asymmetric contributions of SOC and have been able to identify the former as the dominant form of spin-orbit interaction [32]. Hence, SOC may take the form of enhanced Kane-Mele SOC or Valley-Zeeman SOC, which has been predicted to appear in graphene/2H-TMD bilayers [52,53]. Note that the latter effectively breaks the sublattice symmetry of graphene. One of the important consequences of the Valley-Zeeman SOC is the highly anisotropic spin relaxation, which has been revealed by recent first principle calculation and experimental studies [54–56]. If these predictions are true, the induction of spin-valley locking in graphene on TMDs could moreover allow for optical spin injection into graphene [57–59]. Valley-Zeeman SOC is also expected to yield robust topologically-unprotected edge states, *i.e.* present in topologically trivial systems [60].

Computational predictions. Further computational predictions [40, 57, 61] point out that graphene's Dirac point in these structures consistently lies within the semiconducting gap of the TMDs (and shifted towards the valence bands of the TMD with increasing chalcogen atomic number) and displays an orbital gap due to the effective staggered potential linked to the asymmetric potential felt by the two sublattices in graphene. They also report bands splittings due to SOC and inversion-breaking up to 3meV (highest for WSe_2) at the Dirac cones and predict an inverted band structure for the Dirac cones of graphene on WSe_2, which reportedly hosts helical edge states distinct from those in the Kane-Mele model [24] when modelled in a zigzag nanoribbon geometry, holding many similarities with the predictions of topologically-unprotected edge states [60]. Additionally, they report small dipole moments (~ 0.6 Debye) pointing towards graphene, which can be tuned electrically to control the band offsets between graphene and the TMDs. They further identify the metal (d-orbitals) atoms in TMDs to be responsible for the enhancement of SOC. Figure 7 illustrates the effects of valley-Zeeman SOC on the band structures and spin textures of 2H-TMD/graphene heterostructures based on these computational studies, in the case of WS_2 [40].

Other ab initio studies have reported inverted band structures for all four substrate platforms and emphasized the strong dependence of band structures and proximity-SOC on twist-angles between graphene and the $2H$-TMDs. These investigations predicted dramatic increases in the proximity-induced valley-Zeeman and Rashba SOC, whose relative magnitudes can be tuned via the twist angle, as well as in the corresponding bandgaps and band splittings (up to 10 times that of the non-rotated geometry). They have also pointed out the high sensitivity of the band splittings in the Dirac cone to the relative band energies of graphene and the TMD. In particular, these splitting are predicted to rise sharply when the graphene's Dirac point is shifted toward the TMDs bands by applying a gate voltage [62].

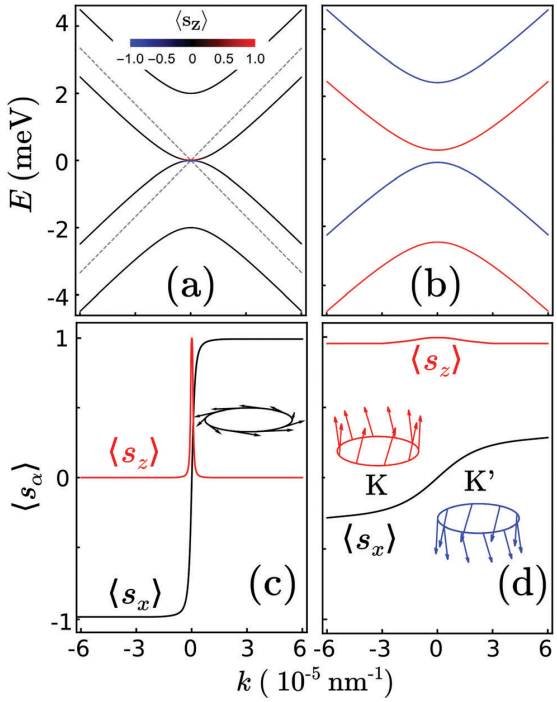

Figure 7: Band structure of graphene (a) with only Rashba SOC (b) in proximity to WS_2, where the color indicates the out-of-plane spin component. The dashed lines show the linear band structure of pristine single-layer graphene. The band structures are quite similar but due to the presence of valley-Zeeman SOC there is a noticeable change in the spin texture, which is shown in panel (c) for Rashba SOC and panel (d) for the WS_2 substrate. The insets show the spin-texture at a given Fermi energy for both cases.

2.7. WTe_2

In this section, a review of the structural, electronic, topological and spin-related properties of WTe_2 (with a focus on the monolayer form) is provided. In addition, a brief description of other notable properties including behaviour under strain is reproduced here.

2.7.1 Crystalline structure

Bulk WTe_2 possesses a layered structure. The naturally-occurring phase is the so-called bulk $1T_d$ phase, which can be thought of as a distorted bulk $1T'$ phase, both illustrated in figure 8. It is distorted in the sense that its unit cell becomes upright ($\beta = 90°$), resulting in an orthorhombic crystal structure. Such a distortion breaks both the in-plane two-fold rotational symmetry $\mathcal{C}_{2a}$ and inversion symmetry present in the bulk $1T'$ phase. These symmetry breakings can be visualized in the following way: the cross-sectional view in the bc-plane illustrated in figure 8 allows for the distinction between two quadrilaterals in both the $1T'$ and $1T_d$ phases, namely a narrow and a wide quadrilateral in each of the layers. As we change from bulk $1T'$ phase

to bulk T_d phase, these quadrilaterals slightly deviate from perfect parallelograms, effectively breaking $\mathcal{C}_{2a}$. More, in the bulk $1T_d$ phase, the centers of these quadrilaterals do not form rectangles in contrast to the unit cell (cfr. solid grey line in figure 8 (a)), which effectively shows that inversion symmetry is broken as well. On the other hand, quadrilaterals in the bulk $1T'$ phase form perfect parallelograms whose centers also form a parallelogram with sides parallel to those of the unit cell. Whereas the transition to bulk $1T_d$ breaks some symmetries of bulk $1T'$, the distortion also gives rise to additional symmetries, including a glide mirror plane $\mathcal{C}_b$ and the out-of-plane two-fold screw rotational symmetry $\mathcal{C}_{2c}$. In short, bulk T_d is an inversion breaking, orthorhombic phase, whose first Brilloin zone is displayed in figure 8. Table 1 gathers the main information concerning the structural phases bulk $1T'$ and $1T_d$.

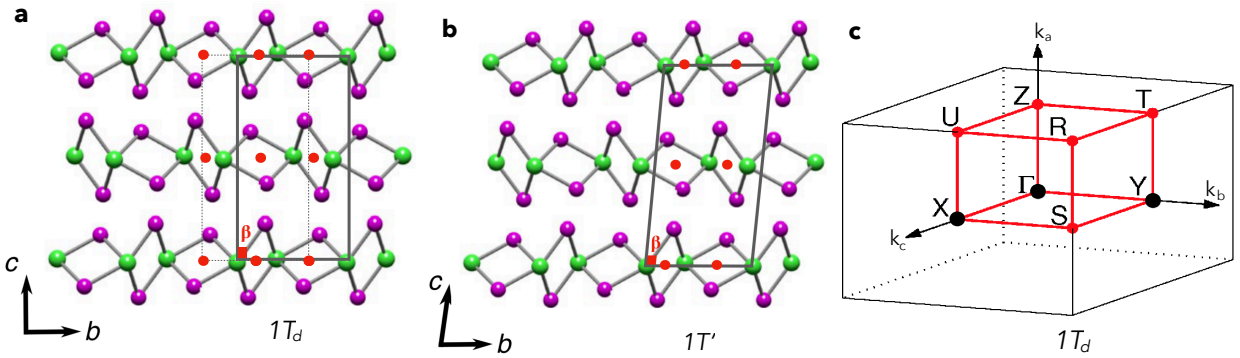

Figure 8: (a) Bulk $1T_d$ crystalline structure of bulk WTe_2. (b) Bulk $1T'$ crystalline structure. (c) First Brilloin zone and labelled high-symmetry points for bulk WTe_2.

	Bulk $1T'$	Bulk $1T_d$
Structural phase	Primitive monoclinic	Primitive orthorhombic
Lattice constants	$a \neq b \neq c$	$a \neq b \neq c$
Angles	$\alpha = \gamma = 90°$, $\beta \neq 90°$	$\alpha = \beta = \gamma = 90°$
Space group	$P2/m$ (11)	$Pmn2_1$ (31)
Point group	C_{2h}	C_{2v}
Symmetries	$\mathcal{I}$, $\mathcal{C}_{2a}$, $\mathcal{M}_a$	$\mathcal{M}_a$, $\mathcal{M}_b$, $\mathcal{C}_{2c}$

Table 1: Main structural features of the bulk $1T'$ and $1T_d$ phases.

The monolayer $1T'$ phase (resp. monolayer T_d) is obtained by directly isolating a single layer from the bulk unit cell of the bulk $1T'$ (bulk T_d) phase (figure 8). Monolayer $1T'$ has two independent symmetries: a mirror plane $\mathcal{M}_a$ and a two-fold rotational axis $\mathcal{C}_{2a}$, whose combination leads to inversion symmetry. In contrast, monolayer T_d only possesses the mirror plane $\mathcal{M}_a$. It can therefore be viewed as a distortion from monolayer $1T'$ where $\mathcal{C}_{2a}$ (and therefore inversion symmetry) is broken. Note that monolayer T_d lacks the $\mathcal{M}_b$ and $\mathcal{C}_{2c}$ symmetries present in bulk T_d (see table 1). This can be explained through the fact that $\mathcal{M}_b$ and $\mathcal{C}_{2c}$ are nonsymmorphic symmetries requiring a translation along the c direction, which naturally breaks down in the monolayer limit. When $\mathcal{C}_{2a}$ is broken, both quadrilaterals in the bc-plane side-view are expected to deviate from perfect parallelograms. In particular, in the $1T_d$ phase, the midpoint between two chalcogen atoms forming one of the quadrilaterals no longer coincide with that of the transition metal atoms, as is illustrated in figure 9 (a) and (b). As mentioned in section 2.5, these phases both showcase a dimerized structure and should therefore display important anisotropy between the directions perpendicular and parallel to the dimer, namely **a** and **b** in figure 9 (a) and (b). In particular, one finds along **a** more closely packed W-W zigzag chains while the separation between tungsten atoms may alternately be much larger along **b**. The corresponding two-dimensional Brilloin zone with important momenta labelled is displayed in figure 9 (c). Additionally, table 2 gathers the main information concerning the $1T'$ and $1T_d$ phases.

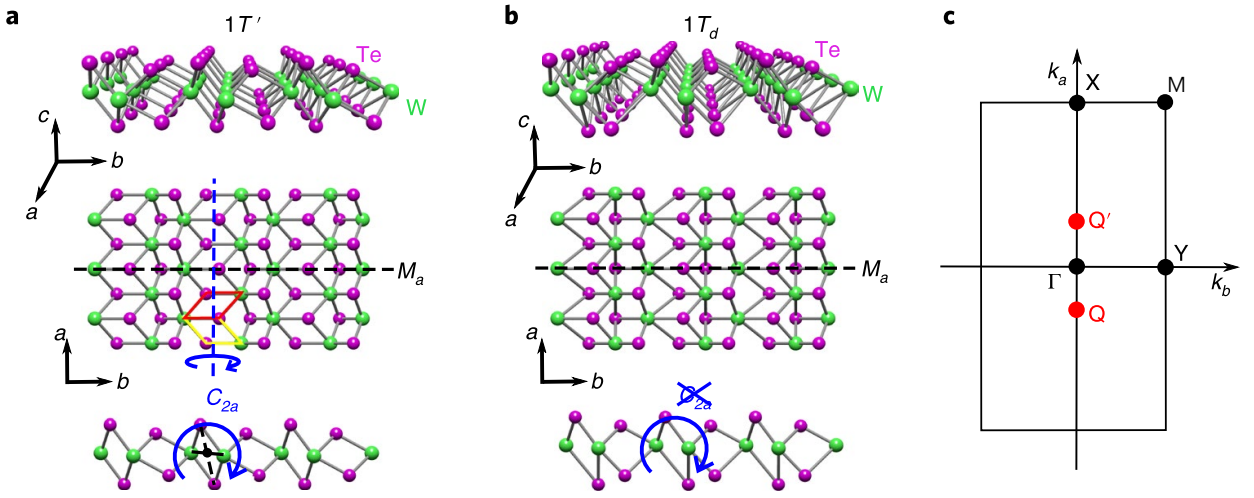

Figure 9: Crystal structure of monolayer WTe_2. (a) The $1T'$ structure of monolayer WTe_2 consists of a mirror plane $\mathcal{M}_a$ and a screw rotation symmetry $\mathcal{C}_{2a}$. $\mathcal{C}_{2a}$ is nonsymmorphic: it involves a 180° rotation about $\hat{\mathbf{a}}$ and a $\frac{a}{2}$ translation along $\hat{\mathbf{a}}$, as depicted by the yellow and red parallelograms. (b) The $1T_d$ structure has only the mirror plane $\mathcal{M}_a$. The rotational symmetry $\mathcal{C}_{2a}$ is broken (exaggerated). (c) The first Brillouin zone with important momenta labelled [63].

	Monolayer $1T'$	Monolayer $1T_d$
Structural phase	Primitive monoclinic	Primitive monoclinic
Lattice constants	$a \neq b$	$a \neq b$
Angles	$\alpha = 90°$	$\alpha = 90°$
Space group	$P2/m$ (11)	Pm (6)
Point group	C_{2h}	C_{1s}
Symmetries	$\mathcal{I}$, $\mathcal{C}_{2a}$, $\mathcal{M}_a$	$\mathcal{M}_a$

Table 2: Main structural features of the monolayer $1T'$ and $1T_d$ phases.

Although the inversion-symmetric $1T'$ structure has been widely assumed in previous work as the most stable phase for monolayer WTe_2 in free-standing conditions [35, 64–66], recent experimental evidence has suggested the stabler phase might actually be $1T_d$ [63]. This will in particular be a subject of investigation of this study. In any case, since electric fields effectively break inversion symmetry, they inevitably lead to the $1T_d$ phase.

2.7.2 Electronic structure

Topological features. Recent experimental evidence for the quantum spin Hall state in monolayer WTe_2 [35, 65–71] has pointed out the extraordinary robustness of the suppression of the bulk conduction in this layered material. In particular, the observation of the hallmarks of the quantum spin Hall state such as quantized conductance suppressed by magnetic fields have been confirmed up to 100K, the highest temperature reported so far. The observation of this state in a layered material is unprecedented and offers significant advantages with respect to the previously discovered realizations of the quantum spin Hall state (cfr. section 2.3). More particularly, it provides a platform that does not rely on buried systems or complex geometries, whose topological nature appears to be insensitive to the nature of the substrate in addition to high operational temperatures, which offers great perspectives to study this intriguing state of matter through microscopy. The topological nature of monolayer WTe_2 is predicted to result partly from a band inversion between two d-orbitals associated with tungsten, which is already somewhat unconventional, with the added complication

that the proximity in energy between W-d_{z^2} and Te-$p_{x,y}$ should lead to strong hybridization of these bands. Thus, the band inversion should be given by a mixture of the p-d and d-d inversions, which sets WTe_2 apart from other $1T'$ TMDs [41]. In particular, the presence of both W-5d and Te-5p characters close to the Fermi level has been confirmed by partial DOS computations based on first-principles [72]. Note that out-of-plane electric fields are predicted to enable a topological phase transition to the trivial phase in $1T_d$ TMDs, by effectively inverting the bands back. This would in particular allow the electrical ON-OFF switching of the helical edge states, effectively realizing a field-effect topological transistor [35].

Electronic state. Bulk WTe_2 is a semimetal. However, there is ambiguous experimental evidence with regard to the nature of the electronic state in monolayer WTe_2. Recent angle-resolved photoemission spectroscopy (ARPES) experiments suggest the existence of a fully gapped band structure [65] while scanning tunneling microscopy (STM) experiments [73] suggest a metallic state. In both cases, conduction band minima (or electron pockets in the semimetallic case) occur at $\pm Q$ (cfr. figure 9) while the valence band maxima in the Γ (hole) pocket occur either at $\pm Q$ or at Γ, leading either to an indirect or direct gap in the insulating case. When observed, metallic behavior is observed in the ΓX direction (including the $\pm Q$ points), which corresponds to the direction of W-W chains along **a** in figure 9, *i.e.* perpendicular to the dimer.

Origin of the gap. As mentioned, there is no evidence for a particularly large bulk gap in WTe_2, and in view of how significantly the bulk gap in the clean limit is usually reduced to arrive at the actual gap appearing in transport data, the enormous robustness of the quantum spin Hall state in WTe_2 poses a fundamental quest to be resolved. While STM measurements would suggest an effective suppressed bulk conductance due to electron-electron correlations [73], ARPES data seem to indicate the presence of a positive band gap. As an added complication, experiments on the monolayers are usually realized on substrates and even though Van-der-Waals coupled substrates might only have a moderate effect in terms of direct hybridization, the substrate could still strain the monolayer, which has been predicted to induce a transition from a metallic to an insulating state within the GGA framework [74,75]. Furthermore, the substrate could break the glide symmetry of the monolayer, leading to other gap opening mechanisms besides SOC [76]. Studies have also attempted to explain the presence of the gap through its temperature-dependence [63] and more exotic potential explanations based on charge-density waves have been proposed as well [66,69]. Whether it can be explained by disorder, substrate effects, correlations, temperature or more exotic effects, it is clear that the origin of the suppression of bulk conductance in monolayer WTe_2 requires further study.

Ab initio modelling. First, one should keep in ming that experiments on WTe_2 monolayers most likely cannot be directly compared with DFT calculations, for the latter does not take into account substrate effects or disorder (at edges for example). Density functional theory (DFT) calculations based on the generalized gradient approximation (GGA) predict a tilted two-dimensional Dirac fermions without spin-orbit coupling (SOC). The Dirac cones gap into overlapping hole and electron pockets once SOC is included, effectively rendering the electronic state metallic. Yet it still features a band inversion. It however remains unclear whether GGA describes the electronic structure correctly. Rather, the ARPES band structures [65] are well reproduced by HSE06 calculations of free standing monolayers. [64,76] This method relies on hybrid functionals, in which DFT is supplemented by exact exchange functionals with screening corrections. This is in agreement with quantum oscillation experiments on bulk WTe_2, hinting that GGA calculations fail to reproduce the electronic structure close to the Fermi level [77]. The inclusion of exact exchange in hybrid-functionals such as HSE06 has been shown to mitigate the effects of self-interaction errors, and therefore is expected to reverse the overlap of the electron and hole pockets. It is indeed found that the indirect band gap shows a linear dependence on the amount of exact exchange [76] and switches from indirect to direct and from negative to positive [63,64,76] with a sufficient inclusion of exact exchange. If a fully-gapped structure were to be confirmed, HSE06 computation would indicate the importance of (post-GGA) correlation effects in monolayer WTe_2.

2.7.3 Spin texture

Band splittings. While the monolayer $1T'$ phase features inversion symmetry and therefore no band-splittings due to SOC, the weak inversion symmetry breaking of $1T_d$ enables their presence. In principle, either $1T_d$ is the naturally-occurring phase of monolayer WTe_2 [63] or the inversion can be provided by the presence of a substrate or a small electric field. In any case, the $1T_d$ phase featuring band splittings remains widely accessible in experiments even if free-standing WTe_2 is found in the $1T'$ phase. In particular, first-principle calculations in monolayer $1T_d$ have shown that the $\pm Q$ pockets exhibit a spin-splitting in the meV range, while the Γ pocket remain nearly spin degenerate.

Spin textures ($\pm Q$)**.** Significant spin-splitting in the $\pm Q$ pockets enables them to display experimentally accessible spin-textures, which have been studied based on first-principle calculations [63,78]. In particular, the $\pm Q$ pockets are found to display a canted Zeeman-like (*i.e.* valley-dependant) spin texture. While the latter features a significant out-of-plane components much like valley-Zeeman coupled $2H$-TMDs (cfr. section 2.5), it also exhibits a significant (and largely k-independent) in-plane component, certainly a consequence of the lack of rotational symmetry in monolayer $1T_d$ TMDs. Figure 10 illustrates the main characteristics differentiating the SOC fields in $2H$-TMDs and WTe_2.

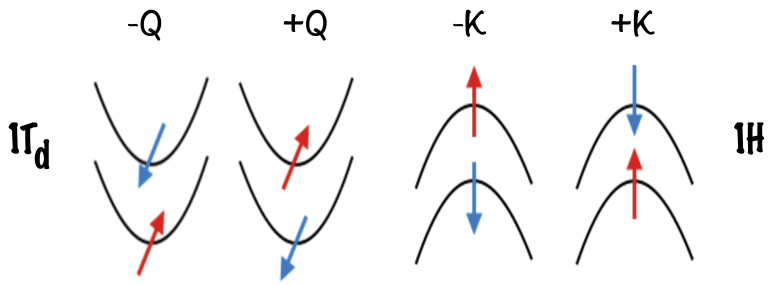

Figure 10: Illustration of the key features and differences in the SOC fields and associated spin texture in monolayer $2H$ and T_d TMDs. (Left) Spin-split $\pm Q$ conduction valleys in T_d monolayer TMDs display both a significant out-of-plane and in-plane component, the latter being relatively k-independent close to the bottom of the electron pocket. (Right) Spin-split $\pm K$ valleys in $2H$ monolayer TMDs only display an out-of-plane component at low energies.

Origin. The observation of these spin textures in the conduction bands of monolayer $1T_d$ WTe_2 has been theoretically traced back to the presence of in-plane dipoles and out-of-plane electric fields [78]. In particular, an in-plane dipole is shown to induce an out-of-plane spin polarization in the $\pm Q$ pockets, whereas as an out-of-plane electric field should generate an in-plane spin-orientation, which is illustrated in figure 11. These considerations offer the prospect of electrical control over the spin textures in the $\pm Q$ pockets, which further establishes monolayer WTe_2 as an exceptional material for spintronics applications. Note that the anisotropy of monolayer WTe_2 sets once again this compound apart from its $1H$ counterparts, for which no canted behaviour is predicted and de facto no control over directionality of the spin textures.

Spin textures (Γ)**.** While the Γ pocket in monolayer WTe_2 features near spin-degeneracy, it should still retain a spin texture. Nevertheless, no trace of a previous detailed study of its spin texture has been found in the literature besides the mention that it strongly depends on the momentum orientation (in contrast to that of the $\pm Q$ pockets) [63]. However, detailed calculations have been performed for the isomorphic Mo-based counterpart of $1T_d$ WTe_2, namely $1T_d$ $MoTe_2$, which is hence supposed to retain the most similarities in the spin texture. More specifically, monolayer $1T_d$ $MoTe_2$ is predicted to feature the same canted Zeeman-like spin-textures in the $\pm Q$ pockets and to exhibit spin polarizations rotating from out-of-plane to in-plane and out-of-plane again in the Γ pocket [79], as displayed in figure 12.

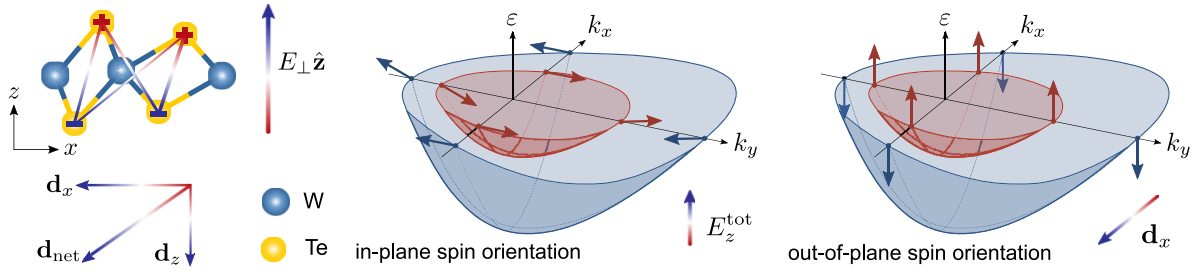

Figure 11: (Left) A net dipole moment d_x can be induced by a perpendicular electric field $E_\perp$ as a result of non-alignment of the Te atoms on the top and bottom layers. (Right) Schematic spin splitting and spin texture of the conduction bands (near the gap) induced by an applied electric field. These can be classed as in-plane spin orientation originating from an out-of-plane electric field E_z^{tot} or out-of-plane spin orientation arising from an in-plane dipole d_x.

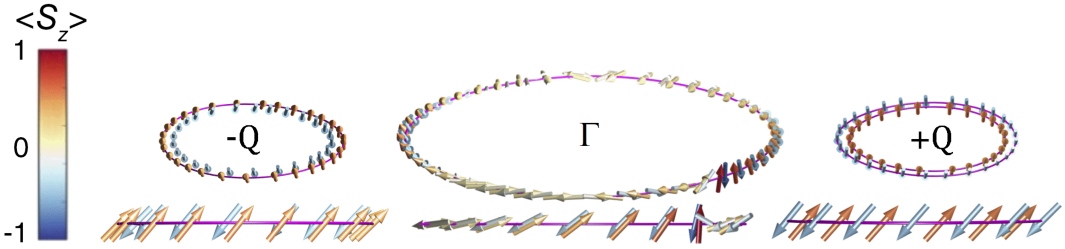

Figure 12: Calculated spin texture in monolayer T_d-$MoTe_2$ for an applied out-of-plane electric field of 0.1V/nm. The two electron pockets are spin-polarized similar to the $2H$-phase materials but with an additional tilt. In the central hole pocket, the spin within each band rotates completely from out-of-plane to in-plane to out of plane again.

All these predictions confirm the non-triviality of spin-textures in monolayer $1T_d$ WTe_2, which can be expected from the combination of high structural anisotropy and inverted band structure.

2.7.4 Strain

The effects of strain in monolayer WTe_2 are relevant to study how substrates may modify the properties of this material but also to gain insight as to how one can manipulate the main features of this layered material through strain engineering.

Stiffness and strength. Mechanical properties of monolayer WTe_2 have been investigated through first-principle computations. In particular, in-plane stiffness along parallel and perpendicular directions to the dimer have been computed [74]. These values are much smaller than that of graphene and functionalized graphene-like materials (such as $2H$-TMDs or hBN) [74, 80]. This indicates that WTe_2 is more flexible than these materials. Computed values for graphene, monolayer WTe_2 and $MoTe_2$ are gathered in table 3. In addition, the monolayer $1T'$-MX_2 phase is predicted to sustain large elastic strains up to 10% [35].

	Graphene	MoS_2	WTe_2 ($\parallel$)	WTe_2 ($\perp$)
ε (eV/Å^2)	21.42	11.23	4.45	6.56

Table 3: In-plane stiffness along parallel and perpendicular directions to the dimer to be compared with that predicted for graphene and a typical $2H$-TMD MoS_2

Effect on electronic properties. Computational studies realized with the GGA framework have reported that a few percent of in-plane elastic strain can change 1T'-WTe_2 (and $MoTe_2$) from semi-metals to small-gap quantum spin Hall insulators by lifting the band overlap and can effectively tune the gap and the overlap. In addition to electrical control, this provides an alternative route to band gap engineering [35, 74, 75]. More particularly, tensile (compressive) strain along **a** (cfr. figure 9) is predicted (within GGA) to decrease (increase) the band overlap while the opposite is true along **b**. In both cases, this gives rise to gap openings around $\pm 3\%$ [75].

Effect on topological features. The topological character of the electronic phase in monolayer WTe_2 is numerically predicted to be preserved up to at least 6% strain, including both tensile and compressive strain [74, 75].

2.7.5 Other properties

Besides the electronic and topological features and non-trivial spin-textures, a myriad of other properties justify the recent interest in WTe_2. A brief review of some of the most exciting phenomenology found to occur in WTe_2 is given here.

Superconductivity. Recent experimental evidence has has pointed out the presence of gate-tunable superconductivity in monolayer WTe_2 with transition temperatures around 1K [70, 81, 82]. An interesting feature of the superconducting state is the fact that the latter occurs at such low carrier density that it can be induced by a simple electrostatic gating. This is in contrast with previous experiments on monolayers, which have either required heavy electrostatic doping or displayed intrinsic superconductivity [83–90]. The discovery may therefore open the door to gate-controlled superconducting circuits. Another exciting trait is the simultaneous presence of non-trivial topology and superconductivity, which is unprecedented in layered materials. This offers the potential to develop topological superconducting devices in a single material, as opposed to the constructions based on chemical doping, application of pressure, or proximity effects, methods that are either ex situ or irreversible and may require fine-tuning at the interface between distinct materials. Furthermore, as mentionned in section 2.3, the simultaneous presence of non-trivial topology and correlations offers great prospects with regard to the realization of robust quantum computation based on the braiding of Majorana boundary modes. Note also that no superconductivity is found in bulk WTe_2 unless high pressure is applied [91, 92].

Non-trivial geometry. Whereas the realization of the QSH has demonstrated the nontrivial topology of the electron wavefunctions of monolayer WTe_2, the geometrical properties of the wavefunction, such as the Berry curvature [93], have recently been shown to be non-trivial as well. In particular, experimental demonstration of the further presence of an electrically-switchable Berry curvature dipole was provided, which is required for a wide range of quantum geometrical phenomena. [63] The simultaneous presence of non-trivial geometry and topology is once again unusual because most topological insulators possess inversion symmetry, in contrast to the $1T_d$ phase of monolayer WTe_2.

Magnetotransport. Experimental studies have reported extremely large positive magnetoresistance (up to tens of millions of percents) at low temperatures in bulk WTe_2. In contrast with other materials, no evidence for saturation of the magnetoresistance was found even at very high applied fields [94]. Although the magnetoresistance has been predicted to dramatically decrease with film thickness (*i.e.* to be much weaker in the case of few layers and monolayers in particular) [95], calculations have shown that it can be greatly enhanced in the monolayer via stacking on graphene to attain values even greater than that obtained for the bulk. The same investigations forecast a strong stacking-orientation-dependent behavior in agreement with the in-plane anisotropy of monolayer WTe_2 [96]. This two-dimensional topological crystal also displays unconventional spin–orbit torques when embedded in ferromagnet/WTe2 bilayers, due to the absence of

rotational symmetries in the material. In particular, it was found to produce the highly sought-after out-of-plane antidamping-like spin–orbit torque needed for devices with perpendicular magnetic anisotropy that are required for high-density applications. [97]

Ferroelectricity. Two- or three-layer WTe_2 were recently discovered as the first metallic platform to exhibit ferroelectricity [98], which was only observed in insulators and semiconductors so far. In particular, robust spontaneous out-of-plane electric polarization switching using gate electrodes has been demonstrated up to room temperature. This property naturally excludes the free-standing centrosymmetric monolayer phase $1T'$, which is de facto non-polar. In the bulk, enhanced screening of electrostatic forces by itinerant electrons is thought to forbid switching by electric fields as well as the development of spontaneous polarizations. [98]

3. Results and discussion

3.1. Methods

First-principles calculations were performed using the ABINIT code [99] and exchange-correlation functionals in the Perdew-Berke-Ernzerhof's form within the generalized-gradient approximation (GGA) of density functional theory [100, 101]. Convergence studies were performed using a tolerance of 0.2% on lattice constants and 5mHa/atom on total energy. In agreement with those studies (cfr. section 5.1), all computations including the relaxation of atomic structures and self-consistent calculations in unit cells and supercells were realized using the smallest k-point grids at least as dense as that corresponding to a sampling of $14 \times 8 \times 4$ for bulk WTe_2. The number of k-points along the direction normal to the plane for two-dimensional structures was naturally reduced to one. The variable used to compare densities is the minimum real-space length corresponding to the maximum interval between two neighbouring k-points *kptrlen* provided by ABINIT. The smallest grid (taking symmetry into account) corresponding to a given k-point density in each structure was determined using the variable *prtkpt* in ABINIT. The corresponding Monkhorst-Pack samplings were centered on $(0.5, 0.5, 0.5)$ (in reduced coordinates) in three-dimensional structures, $(0.5, 0.5, 0.0)$ in two-dimensional structures based on WTe_2 and on $(0.0, 0.0, 0.0)$ for isolated graphene. Maximum residual force for relaxation of the atomic structures were set to $5.0 \cdot 10^{-5}$ Ha/Bohr. In all cases, norm-conserving pseudopotentials were used with kinetic energy cutoff of 35 Ha and calculations were performed with a Gaussian smearing of width 0.001 Ha, in accordance with the convergence analysis (cfr. section 5.1). The inclusion of dipole corrections was realized within the DFT-D3 [102–104] framework as implemented in ABINIT and the non-collinear DFT formalism was used to include spin-orbit coupling.

Concerning post-processing, electronic band diagrams were plotted using *abipy* [105], electronic densities and spin textures were obtained using the *cut3d* post-processing tool of ABINIT [106]. Finally, the geometry and strain analysis realized for the various graphene/WTe_2 supercells was performed with the use of *pymatgen* [107].

3.2. Bulk WTe_2

Although the focus of this study is placed on the monolayer form of WTe_2, it is crucial to show that the methods used in this thesis accurately model its bulk counterpart. Hence this section presents and discusses the results of the computations relative to bulk WTe_2 performed for this thesis, including crystalline and electronic structure calculations.

3.2.1 Crystalline structure

Calculations. Full relaxation of the lattice parameters and atomic positions both in the presence and absence of dipole corrections was performed. Both the resulting lattice constants and those obtained in experiment are gathered in table 4.

Experimental data. Several experimental studies [108, 109] have reported measurements of the lattice constants of bulk WTe_2 in the bulk T_d phase, which are displayed in table 4. In addition, the corresponding Wyckoff atomic positions were obtained experimentally. Due to the symmetries in the structure, W and Te atoms occupy $2a$ Wyckoff positions corresponding to $(0, y, z)$ and $(1/2, -y, z + 1/2)$. Values of x and y predicted by experiment for this structure are reproduced in table 5 [108]. Since the measurements by [108] are performed at the lower temperature, they should be held as the more suitable reference for ab initio computations at absolute zero.

Discussion. Previous reports have stressed the strong dependence of the lattice constants and response to strain on the presence and nature of the dispersion corrections [110, 111]. According to table 4, it appears that van der Waals correction are crucial to match the experimental data. As expected, this is most true in the c direction and is found to have effects in the plane up to 0.8%. In particular, the results obtained in the presence of dipole corrections match experimental values at the lowest temperature [108] up to $\sim 0.1\%$ for a, $\sim 0.7\%$ for b and $\sim 3.5\%$ for c.

	a (Å)	b (Å)	c (Å)
Exp_1 [108]	3.477	6.249	14.018
Exp_2 [109]	3.496	6.282	14.07
VdW	3.480	6.292	14.160
No VdW	3.507	6.326	15.902

Table 4: Lattice parameters obtained in previous experimental studies as well as those computed ab initio both in the absence and presence of dipole corrections.

	W_1	W_2	Te_1	Te_2	Te_3	Te_4
y	0.60062	0.03980	0.85761	0.64631	0.29845	0.20722
z	0.5	0.01522	0.65525	0.11112	0.85983	0.40387

Table 5: According to experimental findings [108], W and Te atoms in bulk WTe_2 occupy the $2a$ Wyckoff positions corresponding to $(0, y, z)$ and $(1/2, -y, z + 1/2)$.$(0, y, z)$ and $(1/2, -y, z + 1/2)$.

3.2.2 Electronic structure

Experimental data and previous computational studies. Several experimental and computational studies have reported measurements and predictions concerning the band structures of bulk WTe_2 [112–115]. A particularly crucial point that this study aims at reproducing is the large band splittings ($\sim$ 50meV) predicted in this material in the presence of SOC.

Calculations. Different approaches were adopted to attempt to reproduce the band structures obtained in previous work for bulk WTe_2 and in particular the large band splittings they predicted. To do so, band structures have been computed in the presence of spin-orbit coupling for input atomic structures with (a) experimentally-obtained lattice parameters and atomic positions at lower temperature [108] (b,c) relaxed atomic positions in the presence/absence of van der Waals corrections and lattice parameters fixed according to [108] (d) relaxed atomic positions in the presence of van der Waals corrections and lattice parameters fixed according to experimental data at slightly higher temperature [109] (e,f) fully relaxed structure in the presence/absence of van der Waals corrections. The corresponding band structures are displayed in figure 14. Since the full experimental case produces the largest band splittings and closely matches previous calculations [112–115], the corresponding computed band structures in the absence/presence of spin-orbit coupling are reproduced in figure 13.

Discussion. The electronic structure is found to display strong dependence on the input atomic structures and on the relaxation schemes undertaken. It is found that relaxing the atomic positions while keeping the lattice parameter fixed at the experimentally found value both in the presence and absence of dipole corrections significantly reduces the band splittings due to the inclusion of spin-orbit coupling, and more so in the case including Van der Waals interactions. Moreover, using the experimental lattice parameters obtained at higher temperatures and utilizing the same scheme renders the band splittings invisible on the scales considered. So do the full relaxation of the structure including and excluding dipole corrections. As expected, excluding these corrections within the full relaxation scheme lead to strong deviations of the band structure from previous findings, showing the importance of long-range interactions in layered materials such as WTe_2. In particular, the large band splittings due to relativistic corrections are best reproduced by using the experimentally-obtained structure at the lower temperature, including both the lattice parameters and atomic positions [108]. Although a first glance at the band structure in the spinless case hints at the presence of two massless Dirac cones around the Fermi level, a closer look reveals small gaps of about 2 meV which can be related to the weak in-plane mirror-glide symmetry breaking of the T_d phase [76]. The same goes for the apparent degeneracy around the Fermi level in the spinfull case as shown in figure 14 (c) and (d).

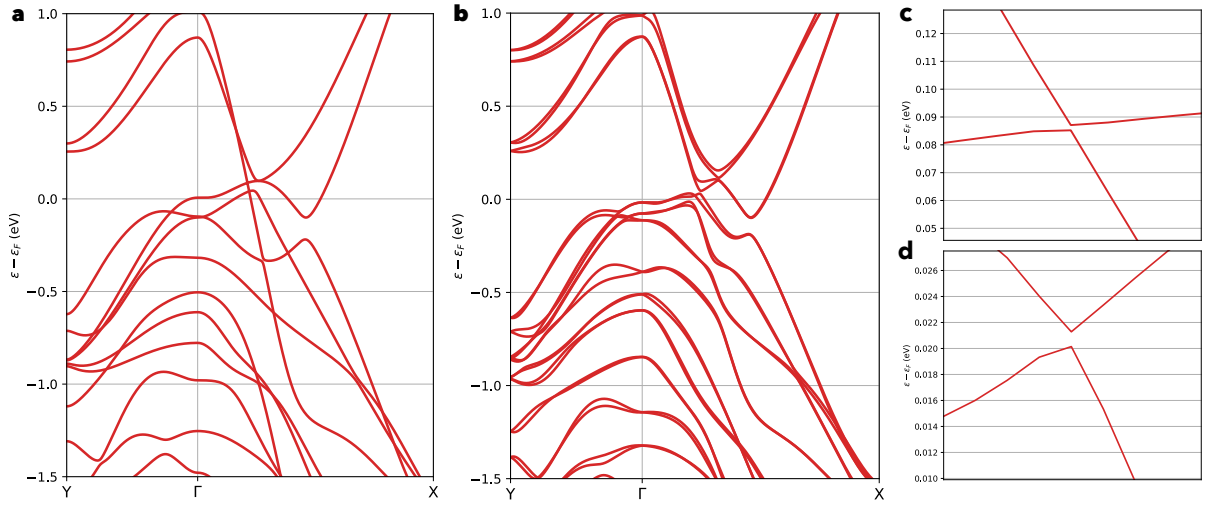

Figure 13: Electronic band structure of bulk WTe_2 for the experimentally obtained atomic structure [108] (a) without SOC (b) with SOC. (c,d) Mirror-glide symmetry breaking in the bulk T_d ensures that degeneracies at the Fermi level are not fulfilled.

3.3. Monolayer WTe_2

The first-principle results obtained with regards to monolayer WTe_2 are presented and discussed in this section, including the structural and electronic structures of this material.

3.3.1 Crystalline structure

Calculations. In order to further investigate the relative stability of the different structural phases potentially adopted by monolayer WTe_2, full relaxation of the lattice parameters and atomic positions of the $1T'$ and $1T_d$ phases both in the absence and presence of spin-orbit coupling and dipole corrections were performed. The resulting lattice constants are gathered in 6.

		No SOC		SOC	
		No VdW	VdW	No VdW	VdW
a (Å)	T'	3.50505	3.46131	3.52281	3.47296
	T_d	3.50481	3.46094	3.52354	3.47318
b (Å)	T'	6.32536	6.30250	6.31707	6.30238
	T_d	6.32526	6.30182	6.31739	6.30230

Table 6: Relaxed lattice parameters for monolayer WTe_2 in the $1T'$ and $1T_d$ phases in the presence and absence of relativistic and dipolar corrections, both of which have significant effect on the results. Similarities between the $1T'$ and $1T_d$ suggests the $1T_d$ phase relaxes to $1T'$.

Discussion. According to table 6, both spin-orbit coupling and dipole corrections are found to have (unusually) significant effects on lattice constants. In particular, deviations up to 1.5% (resp. 0.6%) are observed through the inclusion of van der Waals (relativistic) corrections, which is in agreement with previous studies [64]. Nevertheless, the proximity between lattice parameters of the T_d phase and the T' strongly suggests that the T_d phase relaxes to the T' phase. More specifically, lattice parameters within the same relaxation

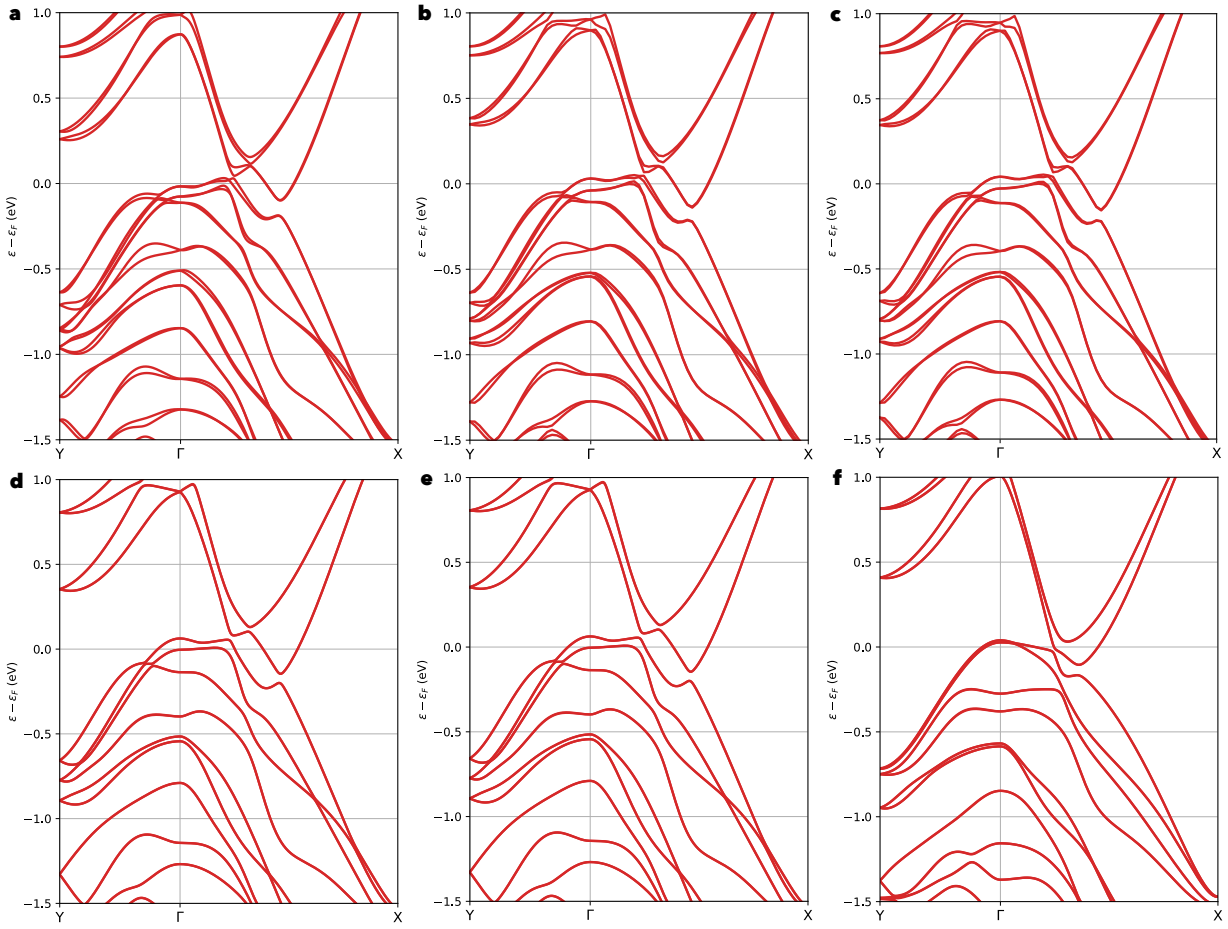

Figure 14: Band structures computed in the presence of spin-orbit coupling for input atomic structures with (a) experimentally-obtained lattice parameters and atomic positions at lower temperature [108] (b,c) relaxed atomic positions in the presence/absence of van der Waals corrections and lattice parameters fixed according to [108] (d) relaxed atomic positions in the presence of van der Waals corrections and lattice parameters fixed according to experimental data at slightly higher temperature [109] (e,f) fully relaxed structure in the presence/absence of van der Waals corrections.

framework only differ by lengths of the order of $\sim 10^{-4}$Å. Further confirmation of this trend is obtained by comparing the computed total energies of both unit cells in calculations using rigorously identical parameters. The obtained absolute total energies are shown in table 7.

		No SOC		SOC	
		No VdW	VdW	No VdW	VdW
ϵ (10^4 eV)	T'	-1.55412736734	-1.55426290631	-1.55440530594	-1.55454016494
	T_d	-1.55412736739	-1.55426290603	-1.55440530617	-1.55454016496
$\Delta\epsilon$ (eV)		$5 \cdot 10^{-7}$	$3.2 \cdot 10^{-6}$	$2.3 \cdot 10^{-6}$	$2 \cdot 10^{-7}$

Table 7: Computed absolute total energies of the relaxed $1T'$ and $1T_d$ phases of monolayer WTe_2 in the presence and absence of relativistic and dipolar corrections.

Differences of a few μeV are observed, which is unsignificant in terms of total energy from a computational point of view. This, along with the absence of imaginary frequencies in the phonon spectra of the $1T'$ phase computed in previous work [35], constitutes further confirmation that the $1T'$ phase is the stabler phase in the monolayer limit (in free-standing conditions) and hints at the absence of energy barrier between the $1T'$ and the $1T_d$ phase. Note that the presence of parity-breaking perturbations such as electric fields should results in the $1T_d$ phase.

3.3.2 Electronic structure

Calculations. Selecting the supposedly more stable $1T'$ phase, band structures of monolayer WTe_2 are computed both in the presence and absence of spin-orbit coupling and dipole corrections. The resulting dispersion relations are presented in figure 15.

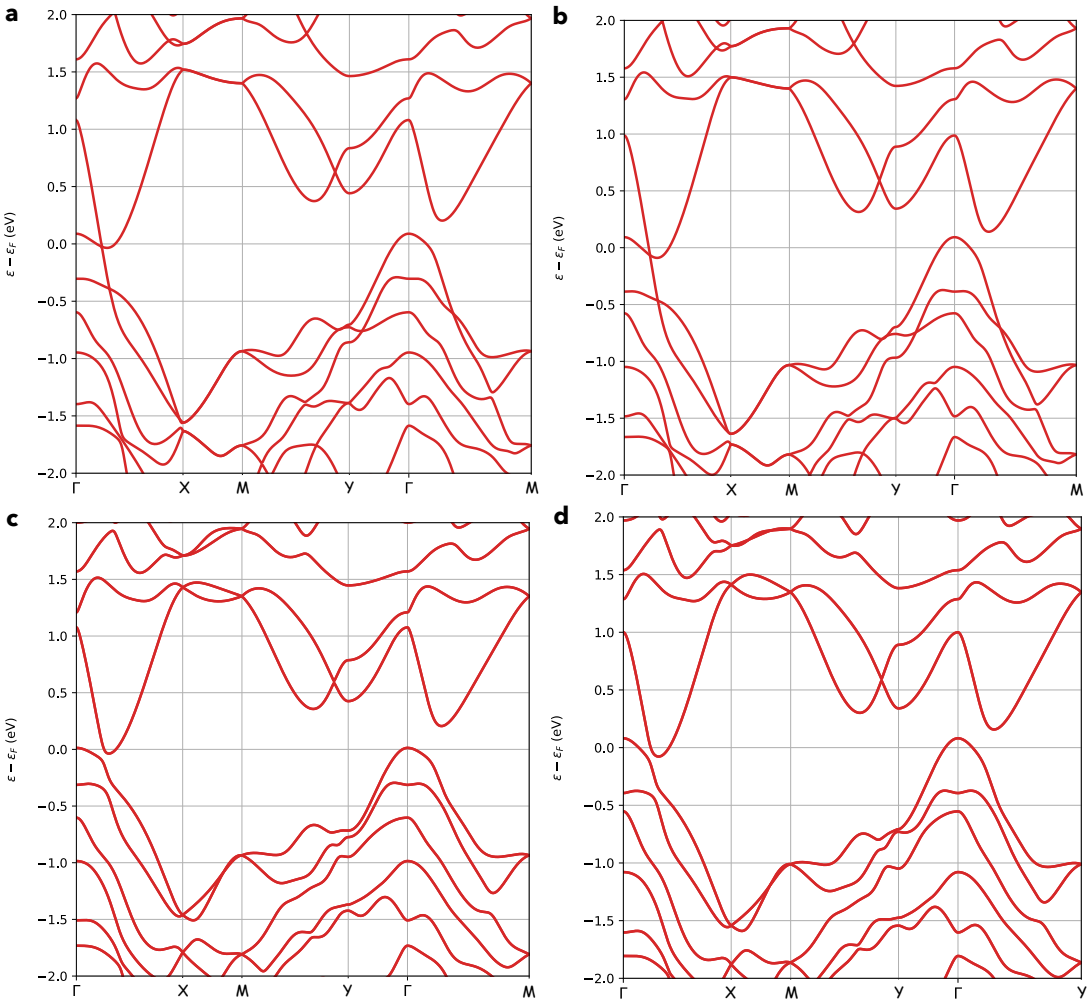

Figure 15: Computed electronic band structure for monolayer $1T'$ WTe_2 (a) in the presence of dipole corrections (b) in the absence of dipole corrections (c) in the presence of both relativistic and dipole corrections (d) in the presence of relativistic corrections.

Discussion. Besides the modest effects of the small in-plane strain induced by the dipole corrections, which is known to modulate slightly the (negative) bandgap within the GGA scheme [74, 75] (cfr. section 2.7.4), the results with and without Van der Waals interactions are highly similar, as shown in figure 15. In the absence of spin-orbit interaction, the presence of two Dirac points is protected by the in-plane mirror-glide symmetry of the $1T'$ phase [76]. The degeneracy is lifted when relativistic corrections are included and the anticrossing band inversion mechanism leading to non-trivial topological phases occurs to create the observed negative bandgap. No band splittings are observed since the simultaneous presence of both time-reversal and inversion symmetries ensures spin-degeneracy for all points in reciprocal space (cfr. section 2.1.3). In particular, this is in agreement with previous results based on the GGA scheme [35] for which the topological nature of the electronic phase was confirmed through the computation of the topological invariant. Whereas these predictions match experiments is still debated (cfr. section 2.7.2).

3.4. Graphene

In this section, the crystalline and electronic structures obtained based on first-principles for graphene are provided and discussed.

3.4.1 Crystalline structure

Full relaxation of the atomic structure in graphene has been performed. In particular, values obtained for the lattice parameters $|\mathbf{a}_1| = |\mathbf{a}_2| = 2.4663$Å are found in agreement with the commonly used value of 2.46Å. [116]

3.4.2 Electronic structure

The electronic band structure of graphene was computed and is displayed in figure 16. In particular, the inclusion of relativistic corrections induce a gap of about $1\mu eV$, which is in agreement with [31].

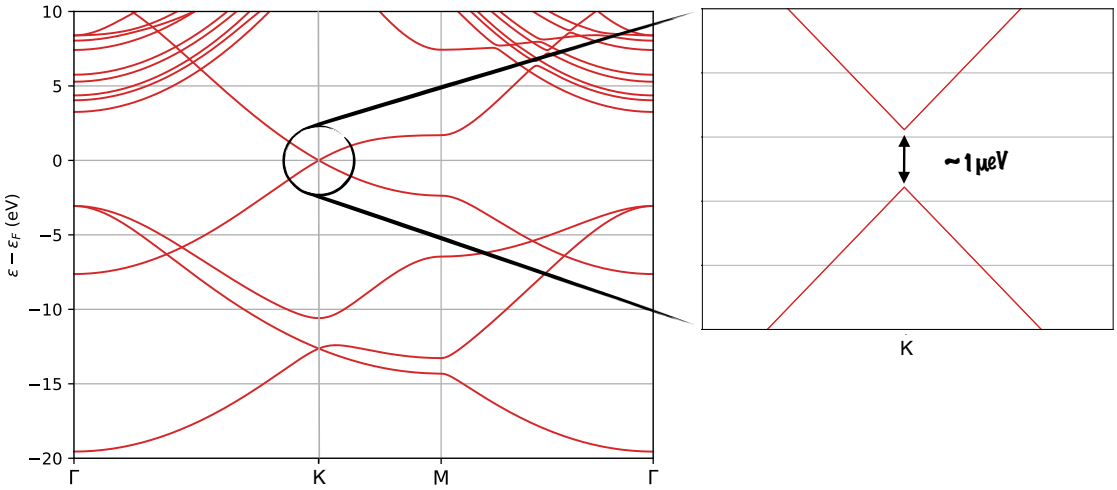

Figure 16: (Left) Computed electronic band structures for single-layer graphene in the absence of SOC. (Right) Occurrence of a small gap of $\sim 1\mu eV$ at the Dirac cone in the presence of relativistic corrections.

3.5. Graphene/WTe_2 bilayer heterostructures

In this section, the ab initio results relative to the investigation of graphene/WTe_2 bilayer heterostructures are provided and discussed. This includes in particular results concerning the crystalline and electronic structures of the supercells considered in this study, as well as an analysis of the electronic density distribution and an examination of the presence of an electric dipole and non-trivial spin textures in the structure.

3.5.1 Crystalline structure

Geometry. In order to investigate graphene/WTe_2 bilayer heterostructures, two supercells of 30 atoms (resp. 72) containing 3×3 (resp. 3×7) supercells of graphene and 2 supercells (resp. 5) of WTe_2 are considered. The geometry is such that the primitive lattice vectors of the supercells are collinear with those of graphene as well as the **a**-axis and $\mathbf{a} + \mathbf{b}$ direction in monolayer WTe_2 (cfr. figure 9). Those supercells were embedded in a slab geometry with vacuum of about 11Å, sufficient according to our convergence criteria (car. section 3.1) and convergence studies (cfr. section 5.1). The resulting supercells possess a lattice mismatch characterized by (Lagrangian) strain tensors displayed in table 8 along with the associated principal and equivalent strains as well as the coordinates of the lattice vectors of the supercells in the primitive basis of graphene and monolayer WTe_2. In particular, strain tensors are computed in the Cartesian basis corresponding to the axis of monolayer WTe_2 (cfr. figure 9). Additionally, a schematic view of these supercells as well as the primitive cells of graphene and WTe_2 is displayed in figure 17 along with a side view of the resulting heterostructure.

	$\mathbf{a}_H, \mathbf{b}_H$ (WTe_2)	$\mathbf{a}_H, \mathbf{b}_H$ (Gr)	ϵ_{eq}^{tot}	ϵ_1^{tot}	ϵ_2^{tot}	ϵ^{tot}
H_1	(1 1 0),(2 0 0)	(0 3 0),(3 0 0)	0.0699	0.0172	0.0678	$\begin{pmatrix} +0.0546 & +0.0218 \\ +0.0218 & +0.0294 \end{pmatrix}$
H_2	(1 1 0),(5 0 0)	(0 3 0),(7 0 0)	0.0333	0.0290	-0.0164	$\begin{pmatrix} +0.0176 & -0.0194 \\ -0.0194 & -0.0059 \end{pmatrix}$

Table 8: Lattice vectors of supercells H_1 and H_2 in terms of the primitive vectors of monolayer WTe_2 and graphene. Corresponding lattice mismatch in the form of Lagrangian strain tensor (in the Cartesian basis corresponding to the axis of monolayer WTe_2) as well as the associated equivalent and principal values.

As stacking graphene on monolayer $1T'$ WTe_2 breaks both the mirror glide symmetry $\mathcal{C}_{2a}$ (and hence inversion symmetry) as well as the mirror symmetry in WTe_2, virtually all symmetries are broken in the heterostructure, the resulting supercell is left with no symmetries. This enables in particular the presence of band splittings (cfr. section 2.1.3).

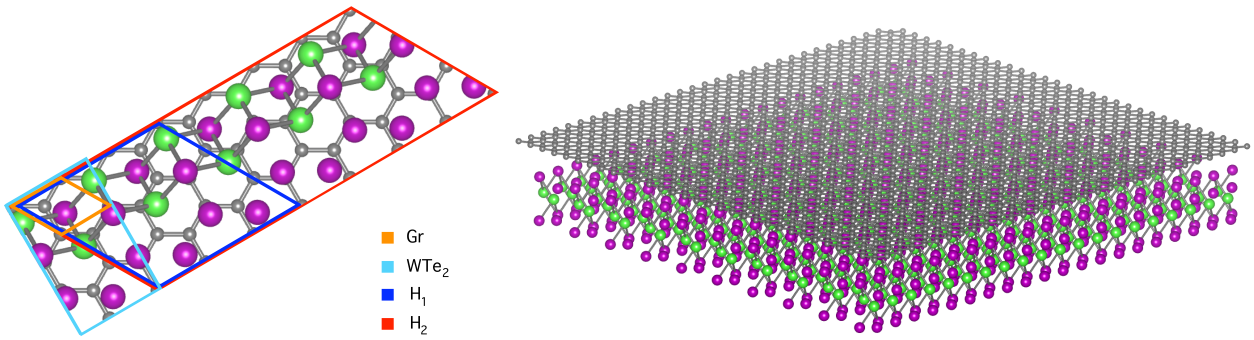

Figure 17: (Left) Unit cell of the two supercells considered in this thesis in perspective with the unit cells of graphene and WTe_2. (Right) Side view of the resulting heterostructure.

Since the interest of this investigation lies in the modification of graphene's electronic and spin-related properties near the Fermi level, one might want to know where graphene's Dirac cones unfold in the first Brillioin zone of the supercells. This can be easily obtained by using the relation between the direct and reciprocal lattice vectors as well as the definition of the supercells' lattice vectors with respect to the primitive vectors of graphene.

$$\left\{ \begin{array}{rcl} \mathbf{a}_{\mathrm{H}} & = & 3\mathbf{b}_{\mathrm{Gr}} \\ \mathbf{b}_{\mathrm{H}} & = & \zeta\mathbf{a}_{\mathrm{Gr}} \end{array} \right. \Rightarrow \left\{ \begin{array}{rcl} \mathbf{a}^*_{\mathrm{Gr}} & = & \zeta\mathbf{b}^*_{\mathrm{Gr}} \\ \mathbf{b}^*_{\mathrm{Gr}} & = & 3\mathbf{a}^*_H \end{array} \right. \Rightarrow \left\{ \begin{array}{ll} \mathbf{K} & \equiv \frac{2}{3}\mathbf{a}^*_{\mathrm{Gr}} + \frac{1}{3}\mathbf{b}^*_{\mathrm{Gr}} = \frac{2}{3}\zeta\mathbf{b}^*_{\mathrm{H}} + 1\mathbf{a}^*_{\mathrm{H}} \\ \mathbf{K}' & \equiv \frac{1}{3}\mathbf{a}^*_{\mathrm{Gr}} + \frac{2}{3}\mathbf{b}^*_{\mathrm{Gr}} = \frac{1}{3}\zeta\mathbf{b}^*_{\mathrm{H}} + 2\mathbf{a}^*_{\mathrm{H}} \end{array} \right. \quad (\zeta = 3, 7)$$

This leads respectively for H_1 and H_2 to

$$\begin{cases} \mathbf{K} &= 2\mathbf{b}^*_{\mathrm{H}_1} + 1\mathbf{a}^*_{\mathrm{H}_1} \sim \Gamma \\ \mathbf{K}' &= 1\mathbf{b}^*_{\mathrm{H}_1} + 2\mathbf{a}^*_{\mathrm{H}_1} \sim \Gamma \end{cases} \quad \text{and} \quad \begin{cases} \mathbf{K} &= \frac{14}{3}\mathbf{b}^*_{\mathrm{H}_2} + 1\mathbf{a}^*_{\mathrm{H}_2} \sim -\frac{1}{3}\mathbf{b}^*_{\mathrm{H}_2} \\ \mathbf{K}' &= \frac{7}{3}\mathbf{b}^*_{\mathrm{H}_2} + 2\mathbf{a}^*_{\mathrm{H}_2} \sim +\frac{1}{3}\mathbf{b}^*_{\mathrm{H}_2} \end{cases}$$

Calculations and discussion. Different configurations are considered with regards to relaxation. Complete relaxation of H_1 is first considered. The significantly higher stiffness of graphene with respect to WTe_2 makes unstrained graphene a good starting point. Given the structural anisotropy in monolayer WTe_2 (cfr. section 2.7.4), the resulting strain in graphene is anisotropic as well, effectively breaking the three-fold rotational symmetry. In particular, this should lead to an angle different from 60° between the supercell lattice vectors upon relaxation even if the latter are collinear with those of graphene before relaxation. Relaxation leads to the following strain tensor in graphene, which basically constitutes mainly a compressive strain of 1.17% along x and 0.59% along y.

$$\epsilon^{tot}_{\mathrm{Gr}} = \begin{pmatrix} -0.0117 & +0.00001 \\ +0.00001 & -0.0059 \end{pmatrix}$$

In particular, the resulting lattice vectors form an angle of 60.148°, which slightly deviates from that in graphene (60°). Besides the effects of a global compressive strain, one should therefore observe the effects of strain anisotropy in graphene mainly in the x direction. The remaining (important) tensile strain is left on WTe_2.

$$\epsilon^{tot}_{\mathrm{WTe_2}} = \epsilon^{tot} + \epsilon^{tot}_{\mathrm{Gr}} = \begin{pmatrix} +0.0429 & +0.0218 \\ +0.0218 & +0.0235 \end{pmatrix}$$

According to previous studies [74, 75], the strong tensile strength along x is expected to lead to the opening of a positive bandgap in monolayer WTe_2. Similarly, the electronic phase supposedly remains topologically non-trivial (cfr. section 2.7.4).

In order to avoid important anisotropic effects of strain in graphene, which should either not be present or to a lesser extent in real heterostructures, relaxation of the atomic positions with lattice parameters fixed at those corresponding to unstrained graphene is also performed in H_1 and H_2. Upon relaxation, the void separating the graphene layer and the WTe_2 is found to be $\Delta c = 3.28$Å in H_1 and $\Delta c = 3.30$Å in H_2.

3.5.2 Electronic structure

Calculations. The computed band structures in the fully relaxed case for H_1 both in the presence and absence of relativistic corrections are displayed in figure 18 including closer views of the Dirac cones associated with graphene in the supercell along the principal axis of monolayer WTe_2 (cfr. figure 9). For comparison, the Dirac cones of the isolated graphene layer (as present in the relaxed supercell) are also included in order to identify the effects of the proximity of monolayer WTe_2. Figure 19 and 20 displays the corresponding results for H_1 and H_2 in the case of unstrained graphene.

Discussion. Starting with figure 18 (a) and (b), one first notices that the band inversion leads to the presence of a small positive band gap when considering only bands associated with WTe_2. In particular, this was expected from the important strain in the x direction in WTe_2. The Dirac point associated with graphene occurs within the gap, close in energy to the conduction bands minimum in the Q electron pocket. The semi-metallic character and linear dispersion of graphene additionally appear to be preserved to a large extent. Taking a closer look at figure 18 (e) and (f) one finds that strain anisotropy in the x direction on graphene induce a splitting of the Dirac into two subcones displaced from Γ along X. This band topology forms a double cross on the $X\Gamma$-X path, therefore leading effectively to 4 crossing points, two at Γ and two along $X\Gamma$ and Γ-X. These points all display avoided crossing with small gaps at each of the crossing points and that already in the absence of stacking on WTe_2 and SOC, *i.e.* only as a results of strain (and potential miniripples in graphene). Looking at figure 18 (c) and (d), one finds that the stacking on WTe_2 results

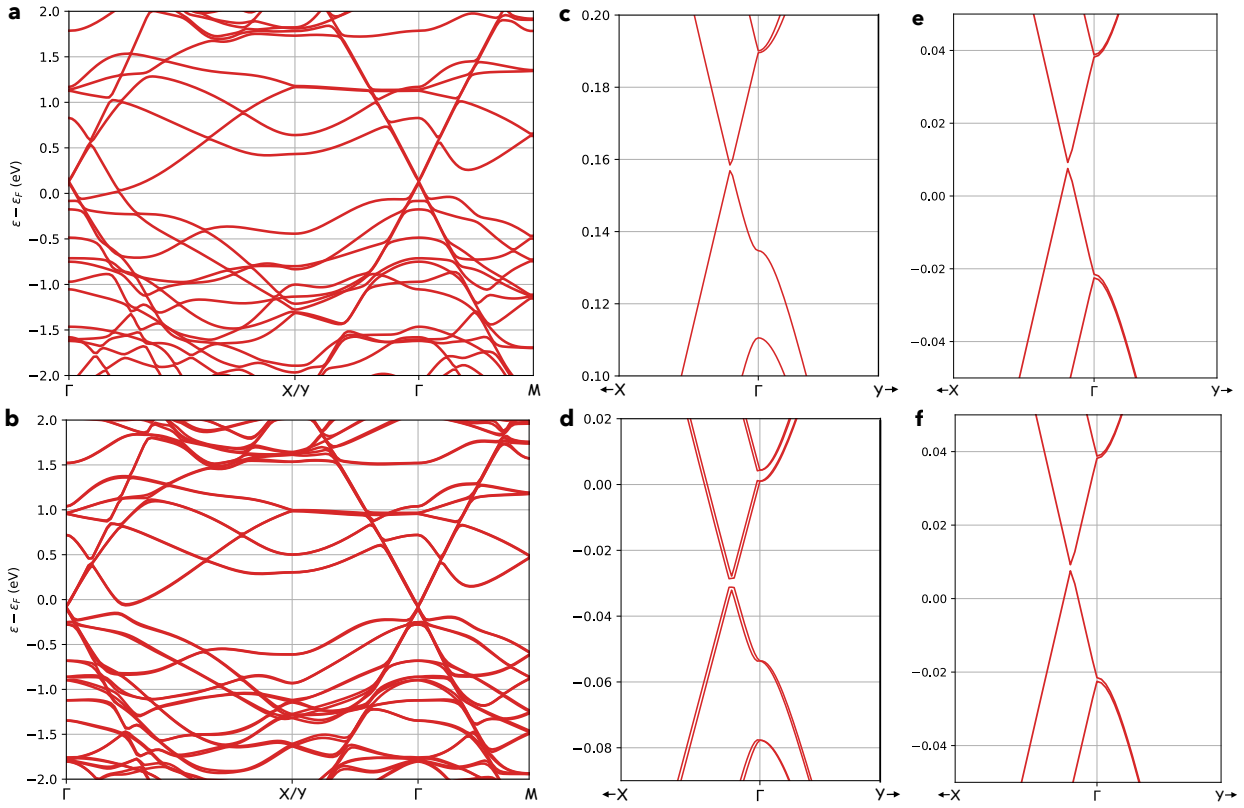

Figure 18: Band structures corresponding to fully relaxed supercell H_1. (a) Without SOC (b) With SOC (c) Dirac cone without SOC (d) Dirac cone with SOC (e) Dirac cone of the isolated graphene layer without SOC (f) Dirac cone of the isolated graphene layer with SOC.

in an important orbital (*i.e.* independent from spin and SOC) splitting at the lower crossing point located in Γ and from SOC to a smaller widening of the higher crossing point at Γ. One might think that these orbital splittings should effectively disappear for larger supercells, since the difference in potential felt by the inequivalent sublattices of graphene should average out given the distinction between the atomic structures of graphene and monolayer WTe_2. In addition, SOC and inversion-breaking allow the presence of small band splittings in the meV range, which somehow feature a clear anisotropy along k_x and k_y, being much larger along k_x (*i.e.* along the W-W chains and perpendicular to the dimer). Note that meV band splittings in the Dirac cone suggest that the proximity-induced SOC is already potentially 1000 times higher than intrinsic SOC in graphene.

Figure 19 displays the corresponding results (for H_1) in the case of unstrained graphene. In particular, virtually no difference if found in figure 19 (a) and (b) with respect to the preceding case. The topology of the Dirac cone is however found to be dramatically different close to the Fermi level. Figure 19 (e) and (f) confirm that the effects on the Dirac cones of the relaxation of atomic positions are minimal in the absence of net strain in graphene and on the scales considered. Taking a closer look at figure 19 (c) and (d), proximity effects once again induce orbital splittings (widened by the presence of SOC) and an effective orbital gap at the Fermi level (The Dirac point is no longer protected by the symmetries of graphene). In addition, large spin splittings are found in the case including relativistic corrections. In comparison to the fully-relaxed case, the latter are much larger and reach $\sim$ 6meV. Again, an important anisotropy is found and features much larger spin splittings along the k_x direction.

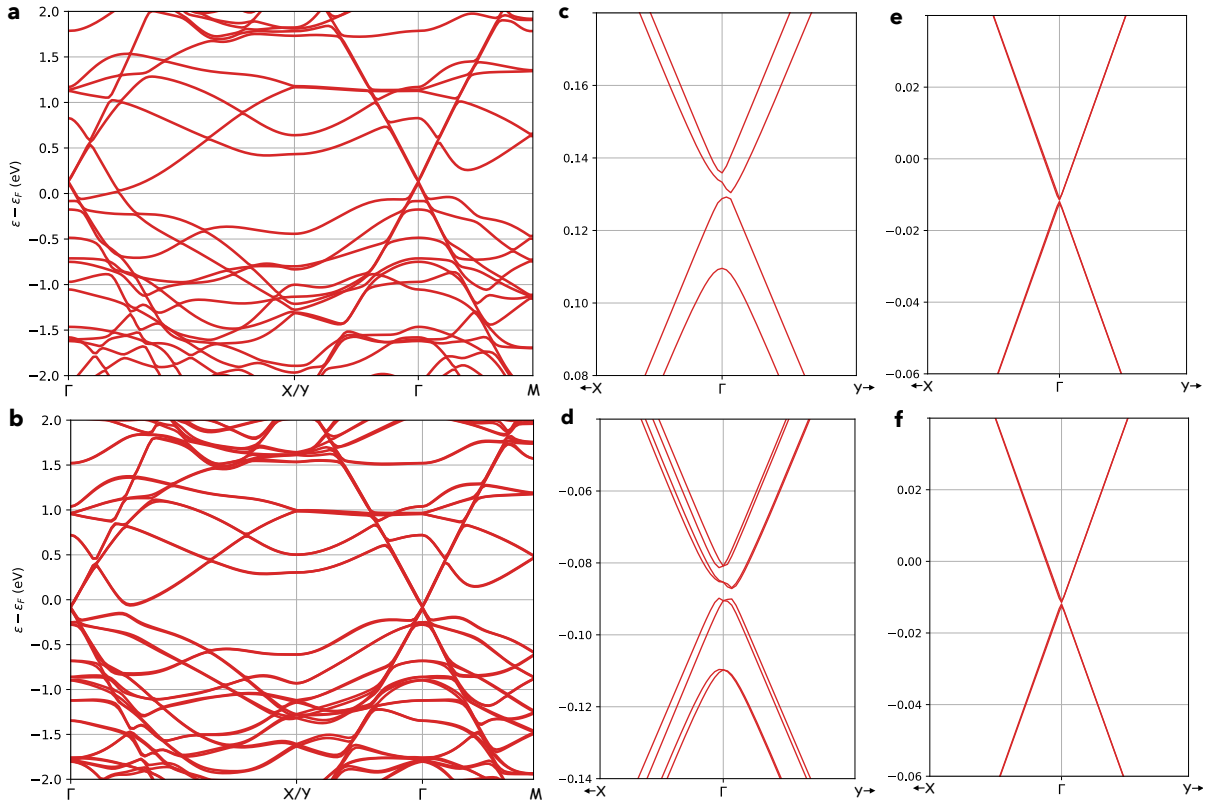

Figure 19: Band structures corresponding to supercell H_1 with relaxed atomic positions and lattice parameters fixed so that the graphene layer is unstrained. (a) Without SOC (b) With SOC (c) Dirac cone without SOC (d) Dirac cone with SOC (e) Dirac cone of the isolated graphene layer without SOC (f) Dirac cone of the isolated graphene layer with SOC.

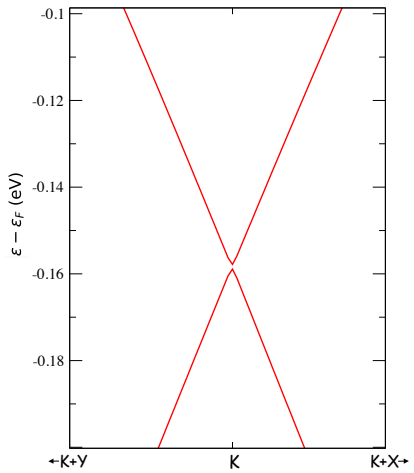

Figure 20: Computed dispersion at the Dirac cone in supercell H_2 in the absence of SOC.

Similarly, the dispersion corresponding to supercell H_2 are presented in figure 20. Due to the size of the supercell, successful calculations were only obtained in the absence of relativistic corrections. The inclusion of SOC requires an amount of computing power that has so far exceeded the resources at hand. Nevertheless, figure 20 shows that in this larger supercell, the orbital splittings and gap virtually vanish, as was expected, and the Dirac cone appears almost unperturbed in the absence of both relativistic corrections and net strain.

Overall, one can conclude the presence of a giant spin-orbit proximity effect similar in strength to that induced by $2H$-TMDs (cfr. section 2.6) featuring an additional anisotropy along the axis of monolayer WTe_2.

3.5.3 Electronic density.

It is interesting to study how the electronic density is distributed in the heterostructures considered. In particular, to investigate the electrostatic effects induced by the proximity of monolayer WTe_2 on graphene, a comparison between the electronic density of the isolated monolayers and that in the heterostructure is relevant. Additionally, one can compare the electronic density associated with the bands corresponding to the Dirac cone in the heterostructure to those in isolated graphene.

Calculations. Figure 21 displays the difference between the total density in heterostructure H_1 (fully-relaxed) and that of the isolated monolayers. For clarity, *total density* here formally refers to

$$n(\mathbf{r}) \equiv \int_0^{\epsilon_F} d\epsilon \sum_{n\mathbf{k}} |\psi_{n\mathbf{k}}(\mathbf{r})|^2 \delta(\epsilon - \epsilon_{n\mathbf{k}})$$

respectively for the monolayers and the heterostructure. Similarly, figure 22 displays the densities associated with the bands of the Dirac cone at Γ in supercell H_1. In order to identify the effects of stacking on WTe_2, figure 23 shows the densities corresponding to the same bands for isolated graphene as found in the heterostructure. More specifically, these densities formally refer to

$$n_{n\Gamma}(\mathbf{r}) \equiv |\psi_{n\Gamma}(\mathbf{r})|^2$$

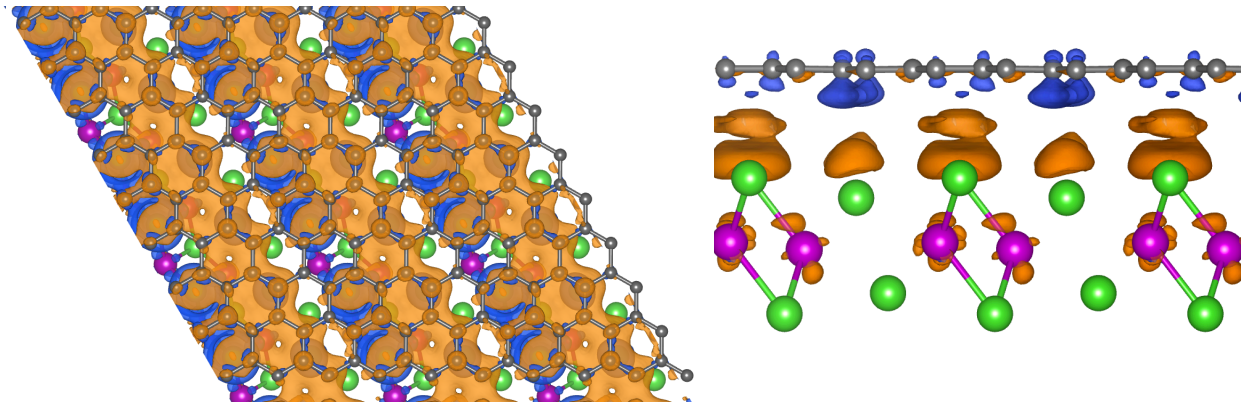

Figure 21: Isosurfaces for the difference in total electronic density between heterostructure H_1 and its two isolated monolayers in order to investigate electrostatic interaction between the two layers. Electronic density excess/depletion are respectively portrayed in blue/orange. (Left) Top view. (Right) Side-view in the bc-plane for monolayer WTe_2 (cfr. figure 9).

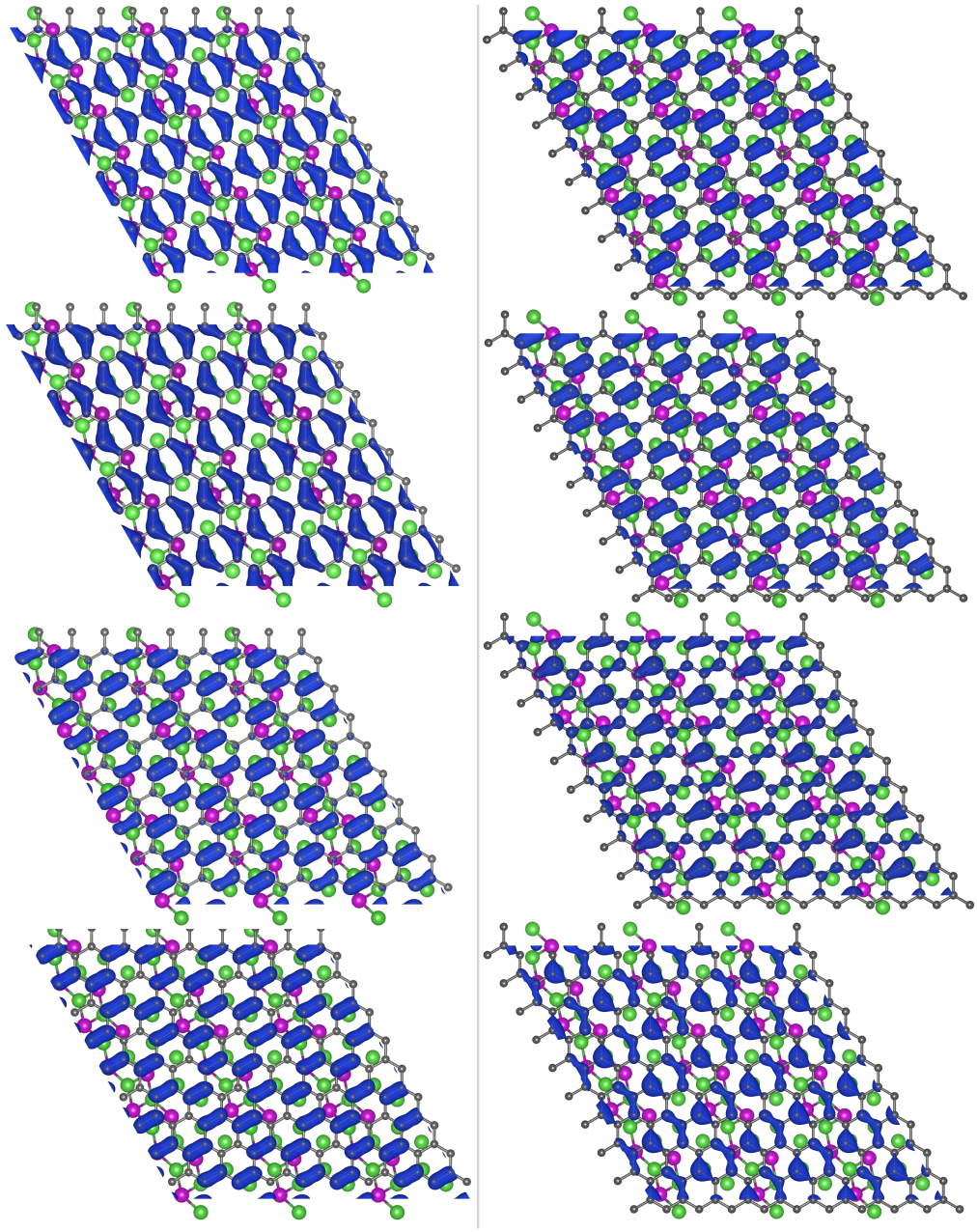

Figure 22: Module of the electronic Bloch functions associated with the Dirac cone at the Dirac point $n_{n\Gamma}(\mathbf{r}) \equiv |\psi_{n\Gamma}(\mathbf{r})|^2$ in supercell H_1 (From top to bottom) Last valence bands and first conduction bands. (Left) Fully relaxed supercell. (Right) Supercell with unstrained graphene.

Discussion. As displayed in figure 21, the total density analysis shows that stacking graphene on WTe_2 globally induces a net gain in electronic density for graphene and correspondingly a net loss for WTe_2. In particular, this indicates that the heterostructure might display a significant dipole moment, whose presence will be investigated at a later stage. Additionally, figure 21 identifies preferential channels for electrons in graphene, situated above the wider quadrilateral along the direction **a** in the unit cell of monolayer WTe_2 (cfr. figure 9). Moving on to figure 22, one first observes that strain in graphene may have important effects on the local (in energy) densities. Comparing to 23, one finds that stacking on monolayer WTe_2 may strongly

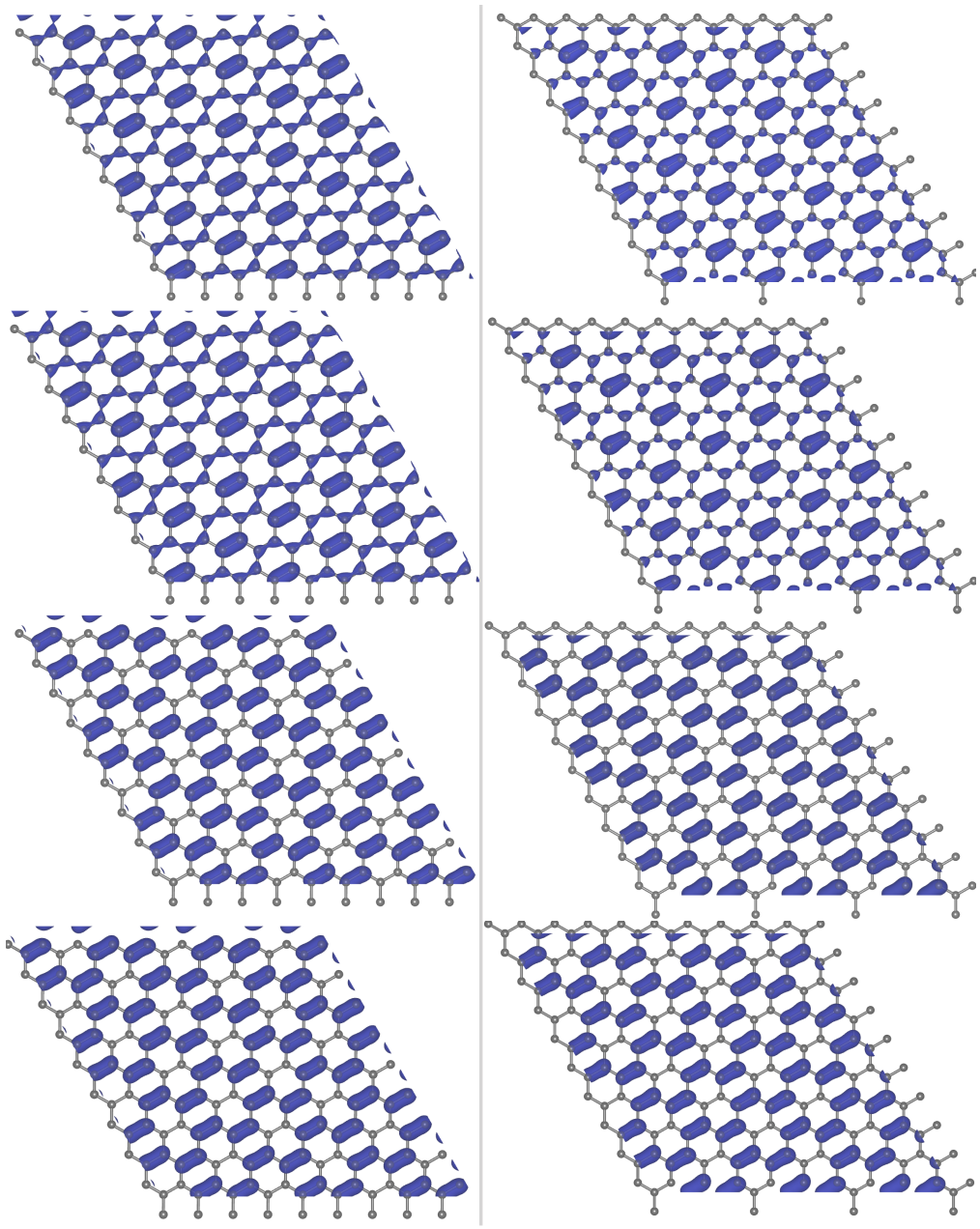

Figure 23: Module of the electronic Bloch functions associated with the Dirac cone at the Dirac point $n_{n\Gamma}(\mathbf{r}) \equiv |\psi_{n\Gamma}(\mathbf{r})|^2$ in graphene as found in supercell H_1 (From top to bottom) Last valence bands and first conduction bands. (Left) Fully relaxed supercell. (Right) Supercell with unstrained graphene.

modify the densities associated with certain bands, indicating the possibility of significant hybridisation. Additionally, comparing the left-hand sides of figure 23 and 22 seems to point that the order of the bands may be inverted in the case of the supercell with graphene left unstrained, when the latter is stacked on WTe_2. Although a band inversion mechanism is not particularly apparent in the computed band structures in figure 19 (c) and (d), this may in fact indicate the occurrence of a topological phase in graphene induced by proximity. This assumption however requires further confirmation.

3.5.4 Dipole

The electronic density analysis has pointed out the potential presence of an electrostatic dipole moment in the heterostructure. As stated in section 2.7.3, this might have crucial effects on the spin textures observed in monolayer WTe_2, which might in turn induce non-trivial spin-textures in graphene. Therefore the presence of a dipole is explored in this section.

Atom		Z_{ion}	Z_{e^-}	Z_{net}
C	1	4	-4.004397	$-4.397195\cdot10^{-3}$
	2	4	-4.007350	$-7.350190\cdot10^{-3}$
	3	4	-4.002780	$-2.779914\cdot10^{-3}$
	4	4	-4.005511	$-5.511389\cdot10^{-3}$
	5	4	-4.005434	$-5.434429\cdot10^{-3}$
	6	4	-4.002780	$-2.779599\cdot10^{-3}$
	7	4	-4.005512	$-5.511631\cdot10^{-3}$
	8	4	-4.007350	$-7.350317\cdot10^{-3}$
	9	4	-4.003488	$-3.488204\cdot10^{-3}$
	10	4	-4.007419	$-7.419043\cdot10^{-3}$
	11	4	-4.005234	$-5.233958\cdot10^{-3}$
	12	4	-4.003397	$-3.396677\cdot10^{-3}$
	13	4	-4.005503	$-5.502907\cdot10^{-3}$
	14	4	-4.005234	$-5.234494\cdot10^{-3}$
	15	4	-4.002910	$-2.910310\cdot10^{-3}$
	16	4	-4.007419	$-7.418690\cdot10^{-3}$
	17	4	-4.004562	$-4.562369\cdot10^{-3}$
	18	4	-4.002910	$-2.909885\cdot10^{-3}$
Te	1	16	-15.95971	$4.029310\cdot10^{-2}$
	2	16	-15.95962	$4.038344\cdot10^{-2}$
	3	16	-15.92644	$7.356436\cdot10^{-2}$
	4	16	-15.92639	$7.360753\cdot10^{-2}$
	5	16	-15.98081	$1.919466\cdot10^{-2}$
	6	16	-15.98158	$1.842047\cdot10^{-2}$
	7	16	-16.00238	$-2.377686\cdot10^{-3}$
	8	16	-16.00238	$-2.383246\cdot10^{-3}$
W	1	14	-14.04297	$-4.296571\cdot10^{-2}$
	2	14	-14.04218	$-4.218004\cdot10^{-2}$
	3	14	-14.04270	$-4.269945\cdot10^{-2}$
	4	14	-14.04328	$-4.328267\cdot10^{-2}$
Total		256	-255.9996	$3.835561\cdot10^{-4}$

Table 9: Computed Hirshfeld charges in fully-relaxed supercell H_1. The labelling of the atoms in the supercell is illustrated in figure 24.

Calculations. In order to investigate the presence of an electrical dipole in the heterostructure, computation of the Hirshfeld charges [117] for all atoms in supercell H_1 (fully relaxed) is performed. These charges are defined with respect to the so-called deformation density, *i.e.* the difference between the molecular and free atomic charge densities. The method divides a system into well-defined atomic fragments and shares the charge density at each point between the atoms in proportion to their free-atom densities at the corresponding distances from the nuclei. This prescription yields well-localized bonded-atom distributions, each of which closely resembles the molecular density in its vicinity. Integration of the atomic deformation densities defines the net atomic charges and multipole moments, which concisely summarize the molecular charge reorganization. The corresponding atomic charges are displayed in table 9.

Based on these calculations, the resulting dipole moment in the supercell is estimated:

$$\mathbf{d} = \sum_i \left(Z^i_{net}|e|\right)\,\mathbf{r}_i = \begin{pmatrix} +0.009\,e\text{Å} \\ +0.029\,e\text{Å} \\ +0.282\,e\text{Å} \end{pmatrix} = \begin{pmatrix} +0.043\,\text{Debye} \\ +0.140\,\text{Debye} \\ +1.352\,\text{Debye} \end{pmatrix}$$

Discussion. Similar orders of magnitude to those obtained for $2H$-TMDs are found [61] although the normalization of this dipole moment remains unclear in those studies (*e.g.* whether it is computed for the entire supercell). A crucial difference however is the presence of a significant y-component in the dipole, which stems from the effective in-plane breaking of inversion symmetry. As stated before (cfr. section 2.5), out-of-plane and in-plane dipoles should respectively induce in-plane and out-of-plane spin polarization components in the conduction bands (associated with the $\pm Q$ electron pockets) of monolayer WTe_2, which might in turn be imported through proximity effects in graphene.

In particular, a gate-tunable canted dipole governing the spin textures in WTe_2 may offer through proximity effects the prospect of partial electrostatic control over spin-textures in graphene, both in terms of strength and directionality. This is of course a great perspective for the integration of graphene in spintronics.

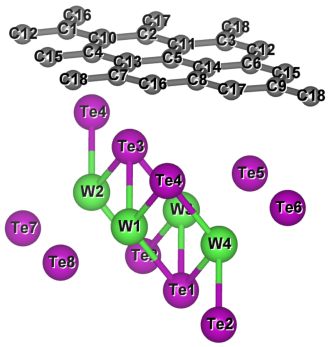

Figure 24: Labels of the atoms in supercell H_1 in correspondence with the associated computed Hirshfeld charges gathered in table 9.

3.5.5 Spin texture

Finally, spin textures in the heterostructure are investigated. Since the main interest of this study lies in the proximity-induced spin-textures in graphene through hybridisation of the bands associated with the Dirac cone by those corresponding to WTe_2 close to the Fermi level, the focus is placed on the spin textures in the last valence bands and first conduction bands of the heterostructure.

Calculations. Figure 25 displays the spin textures obtained in H_1 (with graphene left unstrained) for the two last valence bands and two first conduction bands associated with WTe_2 in the heterostructure. Figure 26 and 27 similarly display the corresponding textures in the last valence bands and first conduction bands of the Dirac cone respectively. All spin textures are centered on the Dirac point situated at Γ. More specifically, these figures display cuts along the *bc*-plane of monolayer WTe_2 (cfr. figure 9), which are found to be the most relevant to the analysis. The full spin textures obtained on a mesh in reciprocal space are provided in appendix 5.2. Note that the fully-relaxed case for H_1 also provided in appendix 5.2 qualitatively displays similar results. The effects of larger scales in the first Brilloin zone and stricter criteria on the wavefunction residuals were explored. In particular, the spin textures were found to be relatively insensitive to these parameters (cfr. appendix 5.2).

Discussion. The expected behaviour for the Γ hole pocket of monolayer WTe_2 is a texture rotating from out-of-plane to in-plane and vice-versa as stated in section 2.7.3. This is in particular in good agreement with the predictions displayed on the left of figure 25. Similarly, the forecast for the bands associated the $\pm Q$ pockets in the presence of both an in-plane and an out-of-plane dipole is a canted Zeeman-like pattern with both in-plane and out-of-plane components, which should remain largely independent of momentum. This is once again consistent with the predictions shown on the right of figure 25. Since computations are performed close to Γ, which is a TRIM, band splittings are negligible and spin-polarizations are expected to be very small. Therefore, the numerical value of the spin polarization bears no experimental significance since the latter is virtually inaccessible (for reference, the maximum value reached in any direction for the polarisation is about $\sim 8\%$ compared to 60% predicted around the $\pm Q$ points in previous studies [63]). This should however not be the case for the spin textures predicted at $\pm K$ in graphene.

Moving on to the bands associated with the Dirac cone in figure 26 and 27, one can naively expect a mixture of Rashba SOC, Kane-Mele SOC and/or canted Zeeman-like induced by WTe_2 in graphene. The predictions feature an important out-of-plane component, which suggests that Rashba SOC is not the dominant mechanism. Given the fact that both valleys in graphene $\pm K$ fold onto the same point, it remains unclear whether the type of SOC induced in graphene is valley-dependant. This should however be the case given the transformation of the energy spectrum under time-reversal symmetry which relates the two valleys of

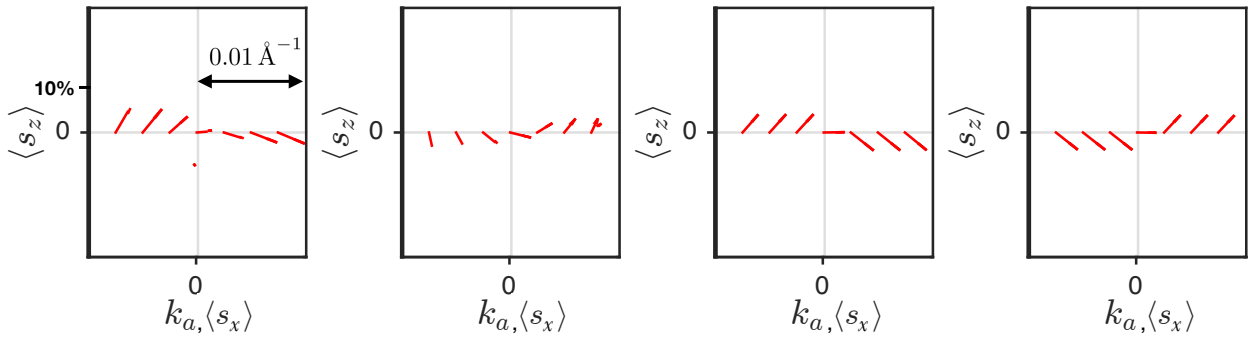

Figure 25: Spin textures at Γ in H_1 (graphene-unstrained) of the bands at the Fermi level associated with monolayer WTe_2. The scales are identical on both axis for spin polarization. (Left) Last valence bands corresponding to the Γ pocket. (Right) First conduction bands corresponding to the $\pm Q$ pockets.

graphene in terms of spin (cfr. equation 2) in the presence of the observed spin splittings (cfr. figure 19). The canted nature is most pronounced for the conduction bands as shown in figure 27 and suggests the canted nature of the SOC field in monolayer WTe_2 is effectively transferred in graphene in those bands. Besides the canted behaviour observed mostly in the conduction bands, a mix of exclusively out-of-plane and in-plane to out-of-plane rotating behaviour (typical of WTe_2's last valence bands) seems to be present in the Dirac cone, indicating possible complex electron-hole asymmetric hybridisation schemes. Overall, these findings point towards highly non-trivial spin textures induced in graphene through proximity effects. It however remains clear that further investigations are needed to identify the dominant trends and symmetries as well as origins of the proximity-induced SOC field.

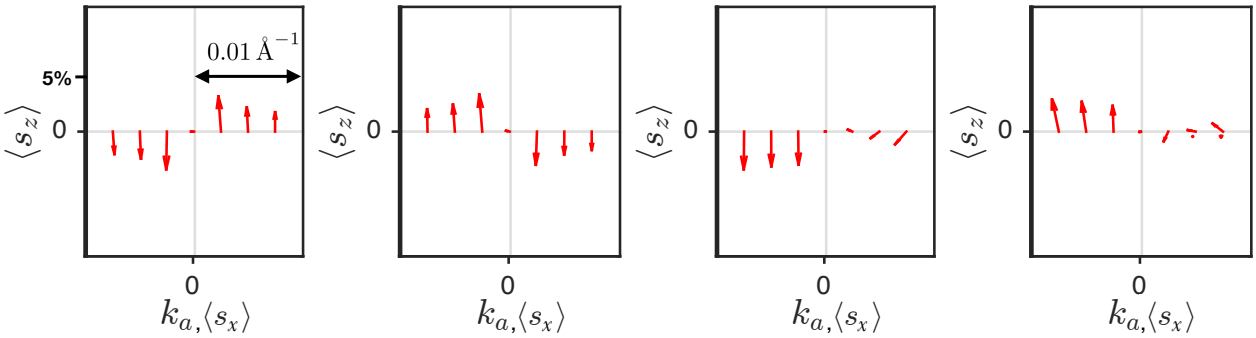

Figure 26: Spin textures at Γ in H_1 (graphene-unstrained) of the bands at the Fermi level associated with the last valence bands in the Dirac cone of graphene. The scales are identical on both axis for spin polarization.

Given the consistency of the predictions obtained for WTe_2 with previous studies, one should be allowed to think that the predictions regarding the symmetries of the spin textures of graphene are accurate to some extent. It is however unclear whether the numerical values for the spin polarisation are accurate, since the latter only reach 3% in the Dirac cones at most along any given direction. An explanation for these results could be the fact that in the considered supercells, K and $-K$ fold onto the same point in reciprocal space, namely Γ. This implies theoretically that the Dirac point becomes a time-reversal invariant momentum, which ensures both the vanishing of bands splittings due to SOC at these points and potentially highly reduced spin polarizations. This guess is further reaffirmed by the fact that our predictions predict an exact numerical spin degeneracy at Γ (which corresponds to the Dirac point in supercell H_1) even in the presence of SOC as illustrated in figure 18 (c,d) and figure 19 (c,d). In principle, this exact numerical degeneracy

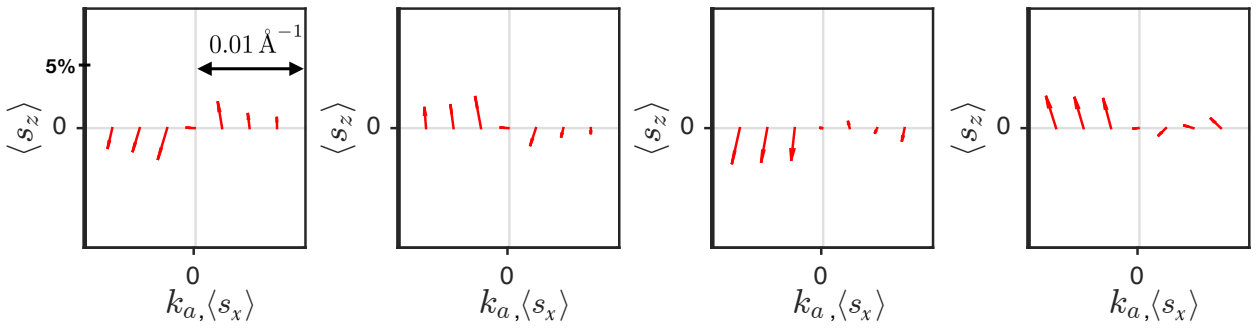

Figure 27: Spin textures at Γ in H_1 (graphene-unstrained) of the bands at the Fermi level associated with the first conduction bands in the Dirac cone of graphene. The scales are identical on both axis for spin polarization.

should not occur since (in-plane and out-of-plane) inversion symmetry is effectively broken in graphene when it is stacked on monolayer WTe_2. This should indeed lead to spin splittings at $\pm K$. It seems however hard to believe that considering different supercells should yield different results concerning this point. In any case, it is clear that the reason for this degeneracy and the reduced size of the spin polarizations around the Dirac point in supercell H_1 requires further study. If considering supercells in which $\pm K$ fold onto each other is found to affect the band structures and spin textures as explained, this may lead to the conclusion that those supercells are unsuitable for the study of SOC-related phenomena in graphene heterostructures.

3.6. Prospects

Several of the results obtained in this thesis call for further investigations to confirm or infirm their potential implications. In particular, the topological nature of the heterostructure needs to be confirmed. A possible way to assess the non-trivial nature of the electronic phase is the computation of a $\mathbb{Z}_2$ invariant. One could similarly study nanoribbon geometries to investigate the presence of edge states. Additionally, one should determine whether the occurrence of a spin degeneracy at the Dirac point is a characteristic of the system or a numerical artefact due to the fact the supercells considered here feature $\pm K$ valleys for graphene folding onto the same point in reciprocal space. The consequences of this choice on the spin textures and spin polarizations induced in graphene should be investigated as well. Considering supercells in which both valleys are not concurrent (*e.g.* H_2 in the presence of SOC) would constitute a potential solution and would allow a valley-resolved analysis for the spin-textures in the heterostructure. This would in particular help in the determination of the symmetries in the proximity-induced SOC field. Exploring larger cells (such as H_2) by including SOC would further confirm the universality of our results and provide results in principle closer to experimental reality due to the reduced lattice mismatch.

4. Conclusion

To summarize, among transition metal dichalcogenides, WTe_2 stands out with a distinct highly anisotropic structure. Furthermore, the non-trivial behaviour of this material in terms of topology, geometry, correlations and spin-transport establish WTe_2 as an outstanding platform to study the interplay between these properties and offers great perspectives for next-generation electronics and quantum computation. This quantum spin Hall material is predicted to feature highly anisotropic gate-tunable spin textures and displays strong spin-orbit coupling. Therefore, it is naturally an exceptional candidate to induce topological phases, strong spin-orbit coupling and/or potentially non-trivial spin-textures in graphene through proximity effects. This would in particular provide a royal way for the realization of graphene-based spintronics.

For these reasons, this dissertation investigated the structural, electronic, topological and spin-related properties of WTe_2 and WTe_2/graphene bilayer heterostructures. In particular, in addition to reproducing the results obtained in the literature in terms of atomic and electronic structure for WTe_2, this project further confirms that the $1T'$ phase is the structure in which the monolayer is found in free-standing conditions. This work predicts that monolayer WTe_2 induces strong spin-orbit coupling in graphene, which should be of the order of 1 to 10 meV, *i.e.* up to 10000 times the spin-orbit coupling in isolated single-layer graphene. It further identifies a sizable anisotropy in this spin-orbit coupling. Moreover, the calculations realized in this thesis point out the presence of a small electric dipole moment in bilayer graphene/WTe_2, which should govern the spin textures in the heterostructure and potentially offer perspectives of electrical control. More, this work suggest that a canted spin texture and a topological phase are indeed transferred to graphene through proximity with WTe_2 although more light is to be shed onto these issues. In any case, this thesis identifies WTe_2/graphene bilayers as a promising platform to enable control over the spin degree of freedom in graphene and calls for further experimental and theoretical investigations.

5. Appendix

5.1. Convergence studies

Figure 28 displays the results of the computations needed for the convergence studies. In particular, the choice of computational parameters undertaken in this study (such as Monkhorst-Pack samplings, kinetic energy cutoff, smearing width, void in supercells describing bidimensional systems made) was based on these results.

5.2. Spin textures

Figure 29, 30 and 31 display various spin textures computed in this study. In particular, they can be used to assess the universality and quality of the results provided in section 3.5.5. The corresponding in-plane components are displayed in figure 32, 33 and 34. Whereas stricter criteria on wavefunction residuals and larger scales in reciprocal space are found to have little consequences on the spin textures, differences in strain (between fully-relaxed cells and those with unstrained graphene) are found to have non-negligible effects on the spin textures both in the bands associated with graphene and WTe_2. Nevertheless, all spin textures qualitatively display the same behaviour as that described in 3.5.5.

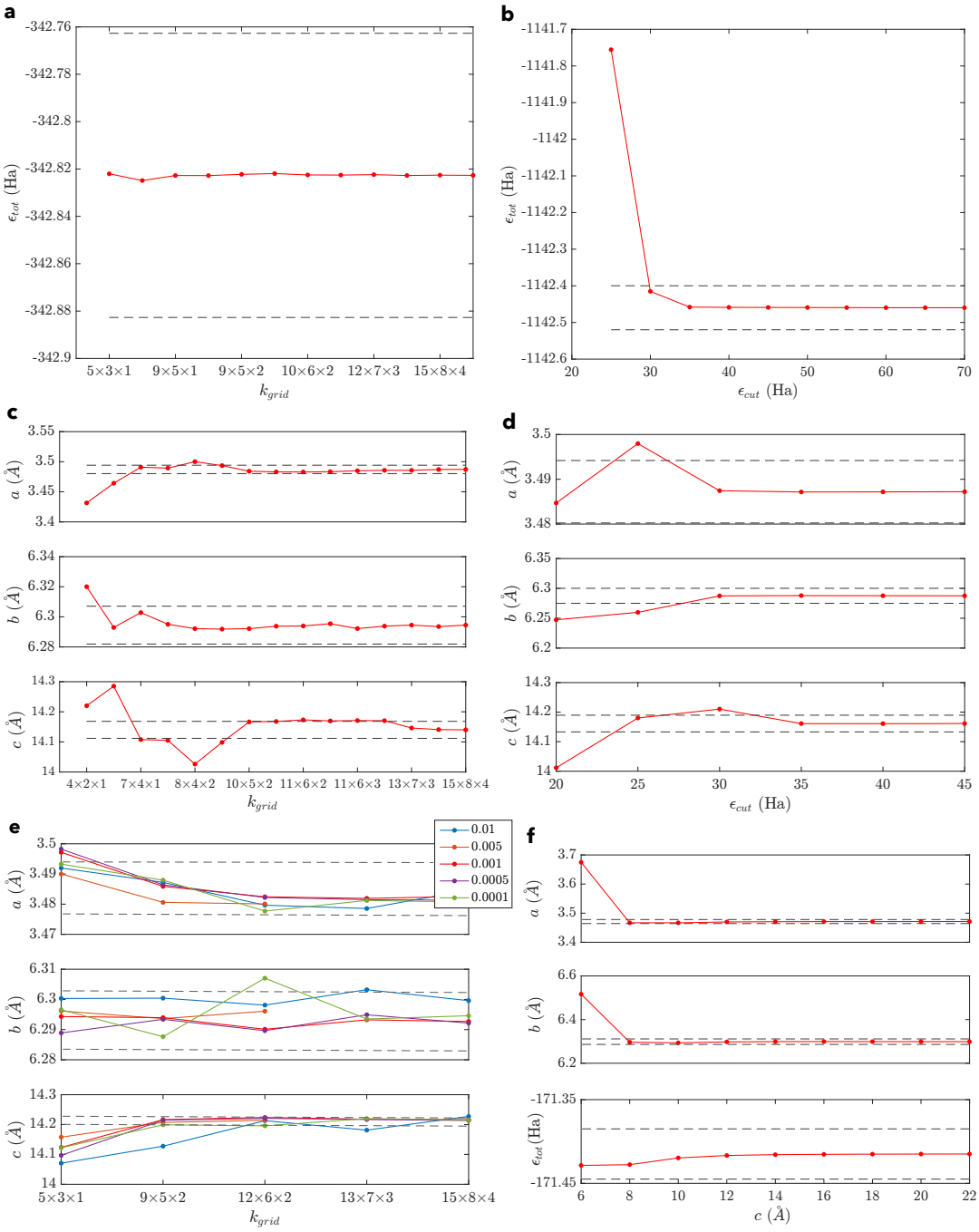

Figure 28: Convergence studies. Dashed grey lines indicate a 0.2% criterion on lattice constants and 5mHa/atom on total energy. (a) Total energy in bulk WTe_2 as a function of the size of k-point grid. (b) Total energy in bulk WTe_2 as a function of the energy cutoff. (c) Lattice constants in bulk WTe_2 as a function of the size of k-point grid. (d) Lattice constants in bulk WTe_2 a function of the energy cutoff. (e) Lattice constants in bulk WTe_2 as a function of the size of k-point grid for different Gaussian smearing widths. (f) Lattice constants and total energy in monolayer WTe_2 as a function of the size of the cell considered along the normal to the plane.

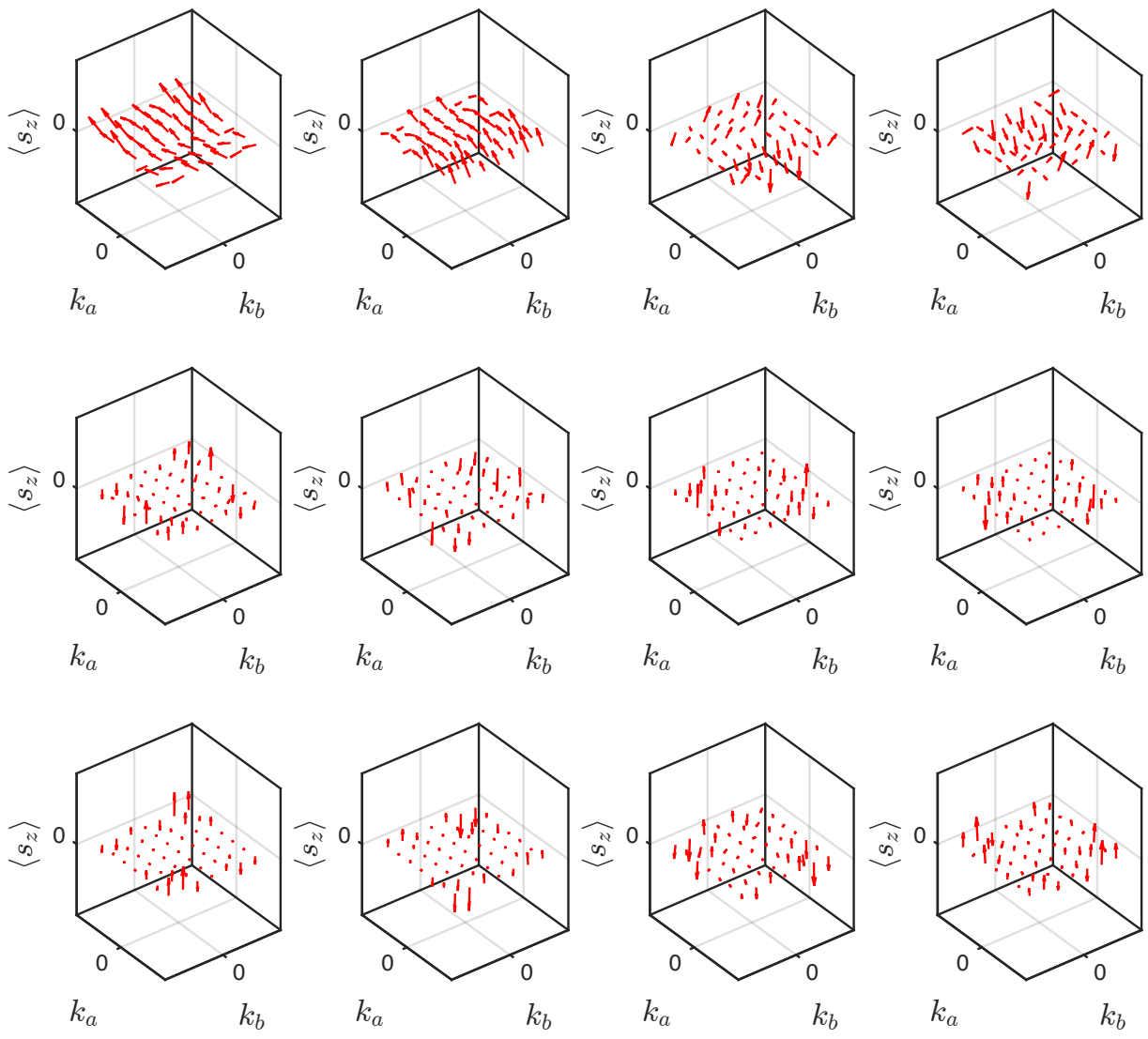

Figure 29: Spin textures in H_1 (fully-relaxed) obtained on a 7×7 mesh centered on the Dirac cone at Γ in reciprocal space for bands around the Fermi level. (From top to bottom) Valence and conduction bands associated with WTe_2; Valence bands in the Dirac cone associated with graphene; Conduction bands in the Dirac cone associated with graphene. The same scale as that considered in section 3.5.5 is used.

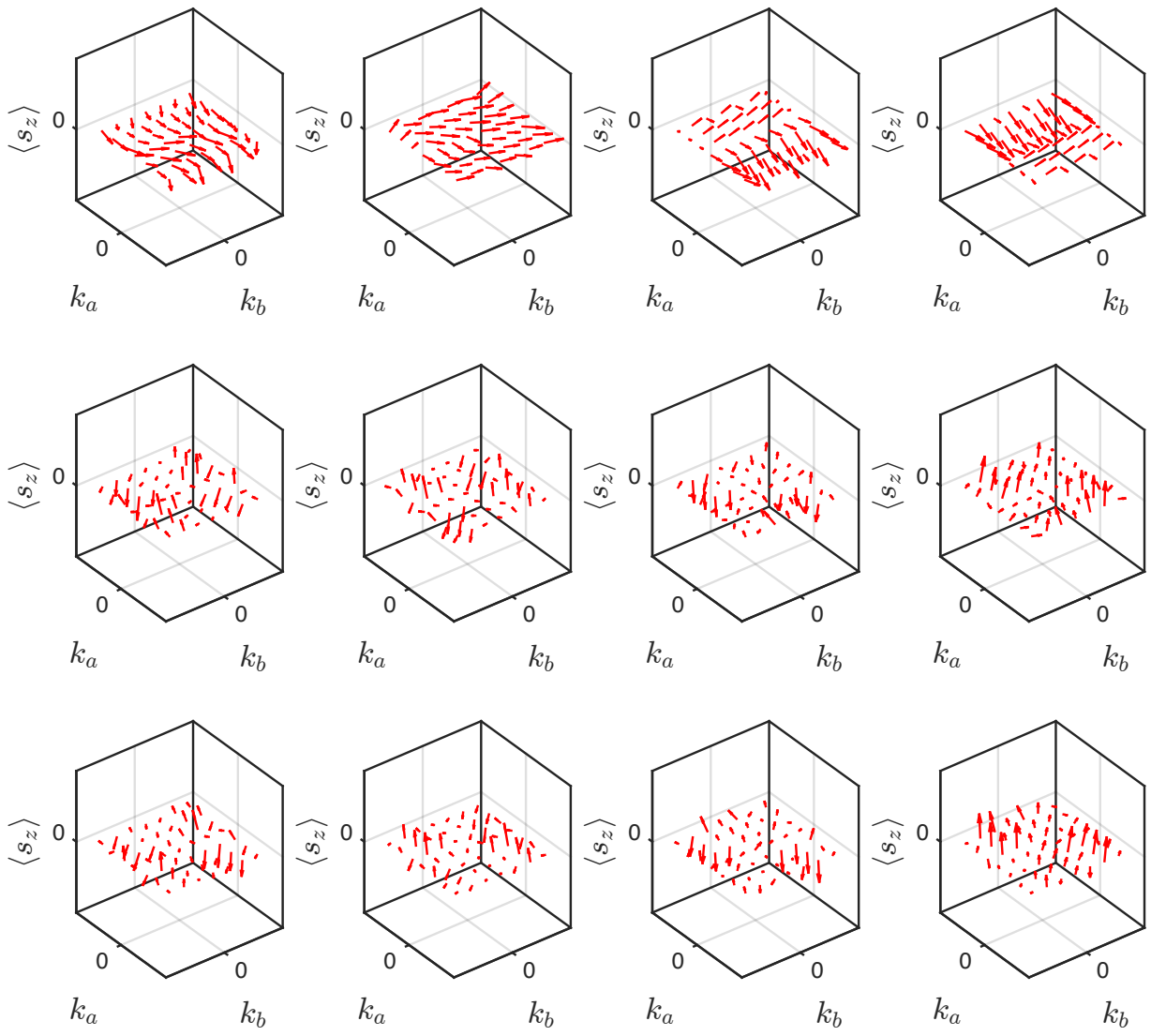

Figure 30: Spin textures in H_1 (graphene unstrained) obtained on a 7×7 mesh centered on the Dirac cone at Γ in reciprocal space for bands around the Fermi level. (From top to bottom) Valence and conduction bands associated with WTe_2; Valence bands in the Dirac cone associated with graphene; Conduction bands in the Dirac cone associated with graphene. The same scale as that considered in section 3.5.5 is used.

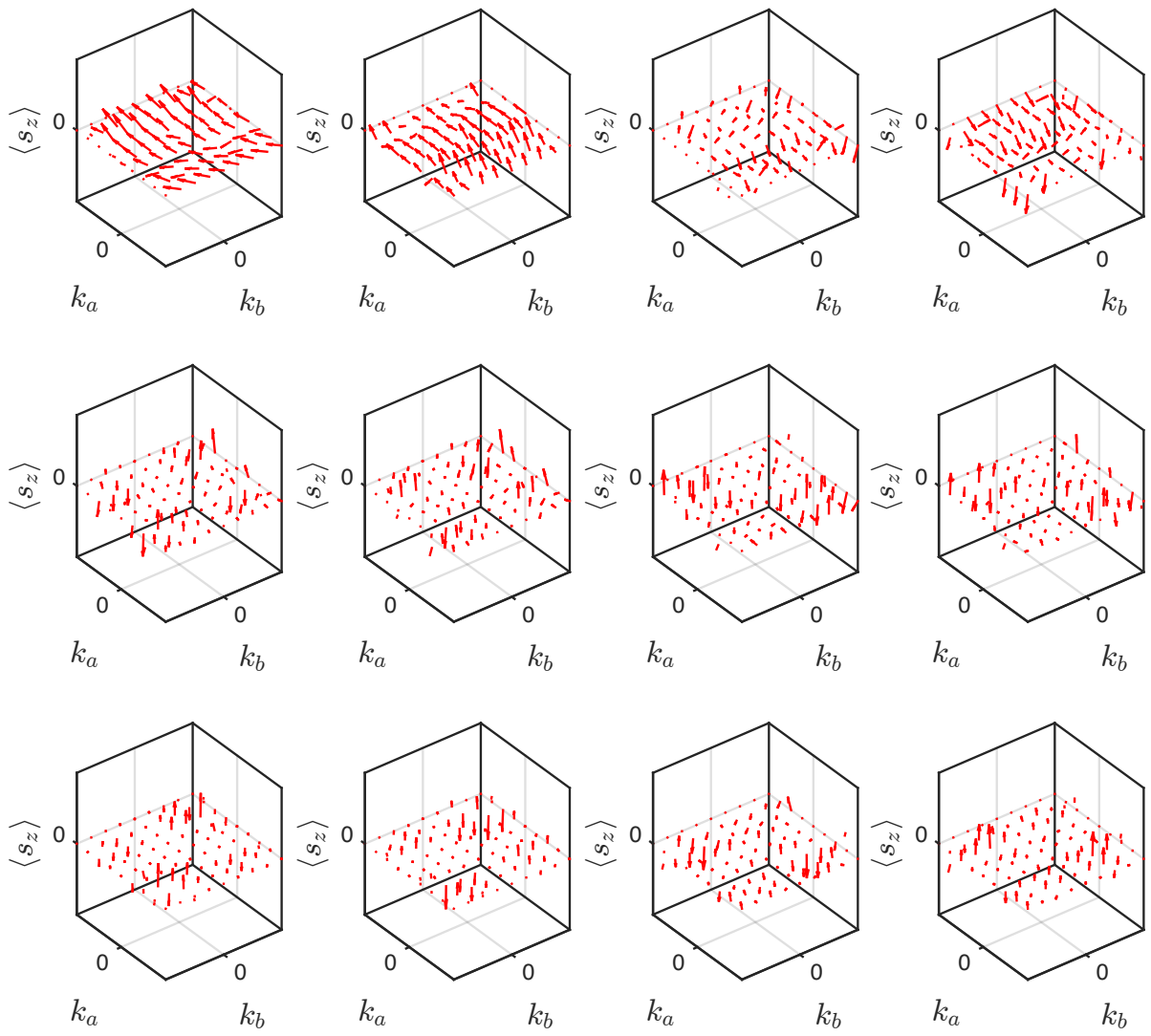

Figure 31: Spin textures in H_1 (graphene unstrained) obtained on a 9×9 mesh centered on the Dirac cone at Γ in reciprocal space for bands around the Fermi level. (From top to bottom) Valence and conduction bands associated with WTe_2; Valence bands in the Dirac cone associated with graphene; Conduction bands in the Dirac cone associated with graphene. The scale investigated here in reciprocal space is 1.5 that considered for all other spin textures. Additionally, a 10^8 times stricter criterion on wavefunction residuals is used.

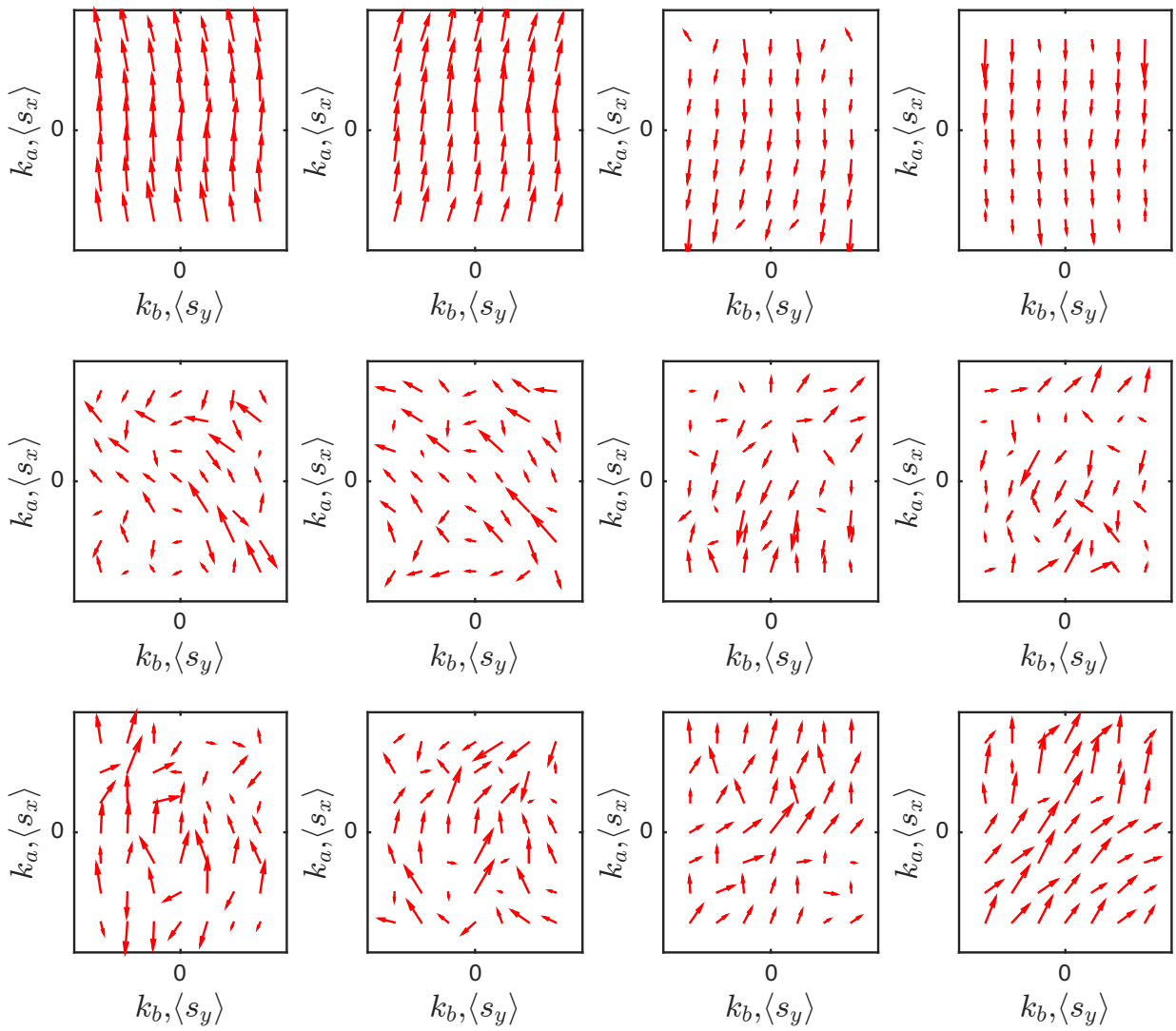

Figure 32: In-plane spin textures in H_1 (fully-relaxed) obtained on a 7×7 mesh centered on the Dirac cone at Γ in reciprocal space for bands around the Fermi level. (From top to bottom) Valence and conduction bands associated with WTe_2; Valence bands in the Dirac cone associated with graphene; Conduction bands in the Dirac cone associated with graphene. The same scale as that considered in section 3.5.5 is used.

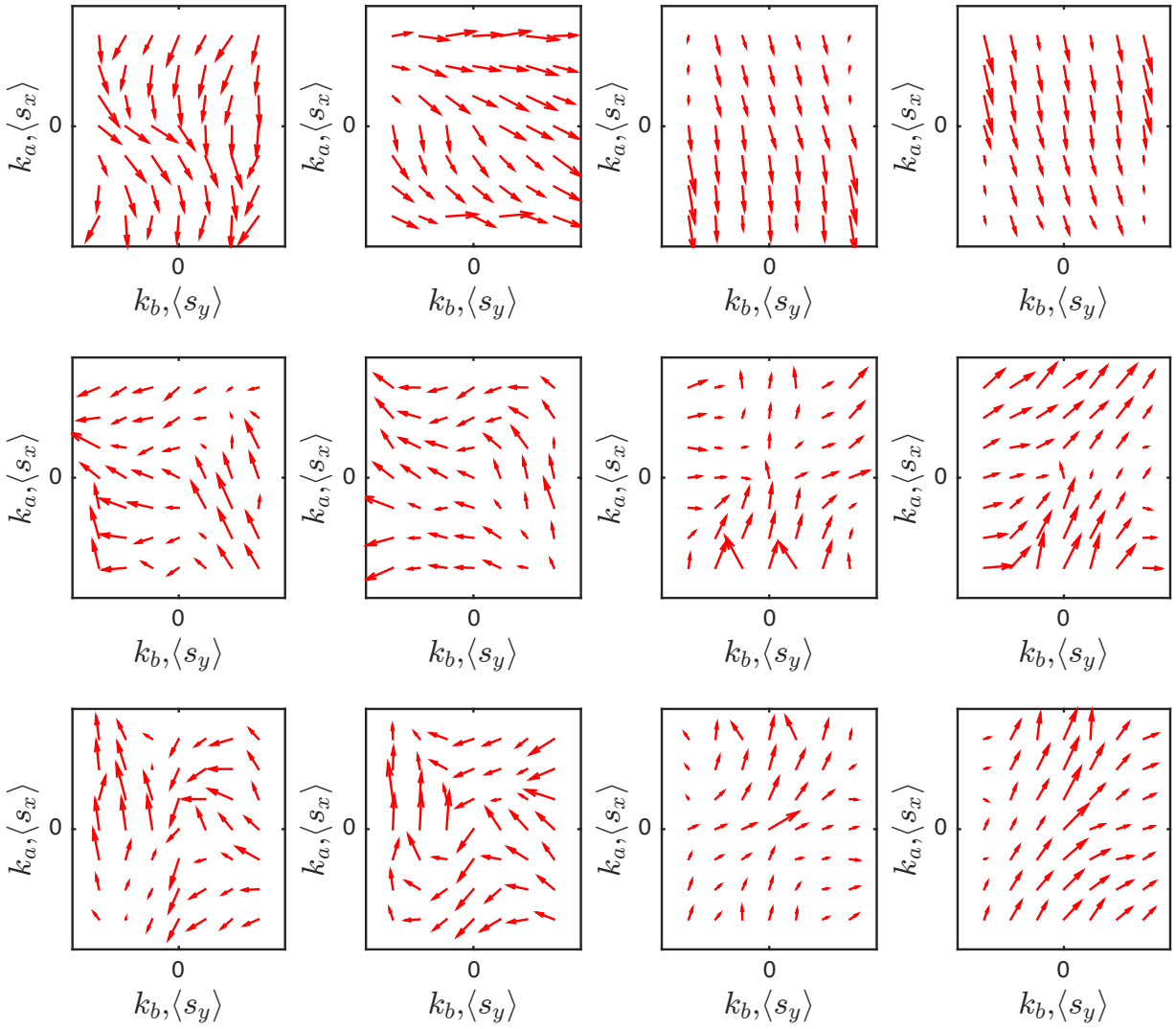

Figure 33: In-plane spin textures in H_1 (graphene unstrained) obtained on a 7×7 mesh centered on the Dirac cone at Γ in reciprocal space for bands around the Fermi level. (From top to bottom) Valence and conduction bands associated with WTe_2; Valence bands in the Dirac cone associated with graphene; Conduction bands in the Dirac cone associated with graphene. The same scale as that considered in section 3.5.5 is used.

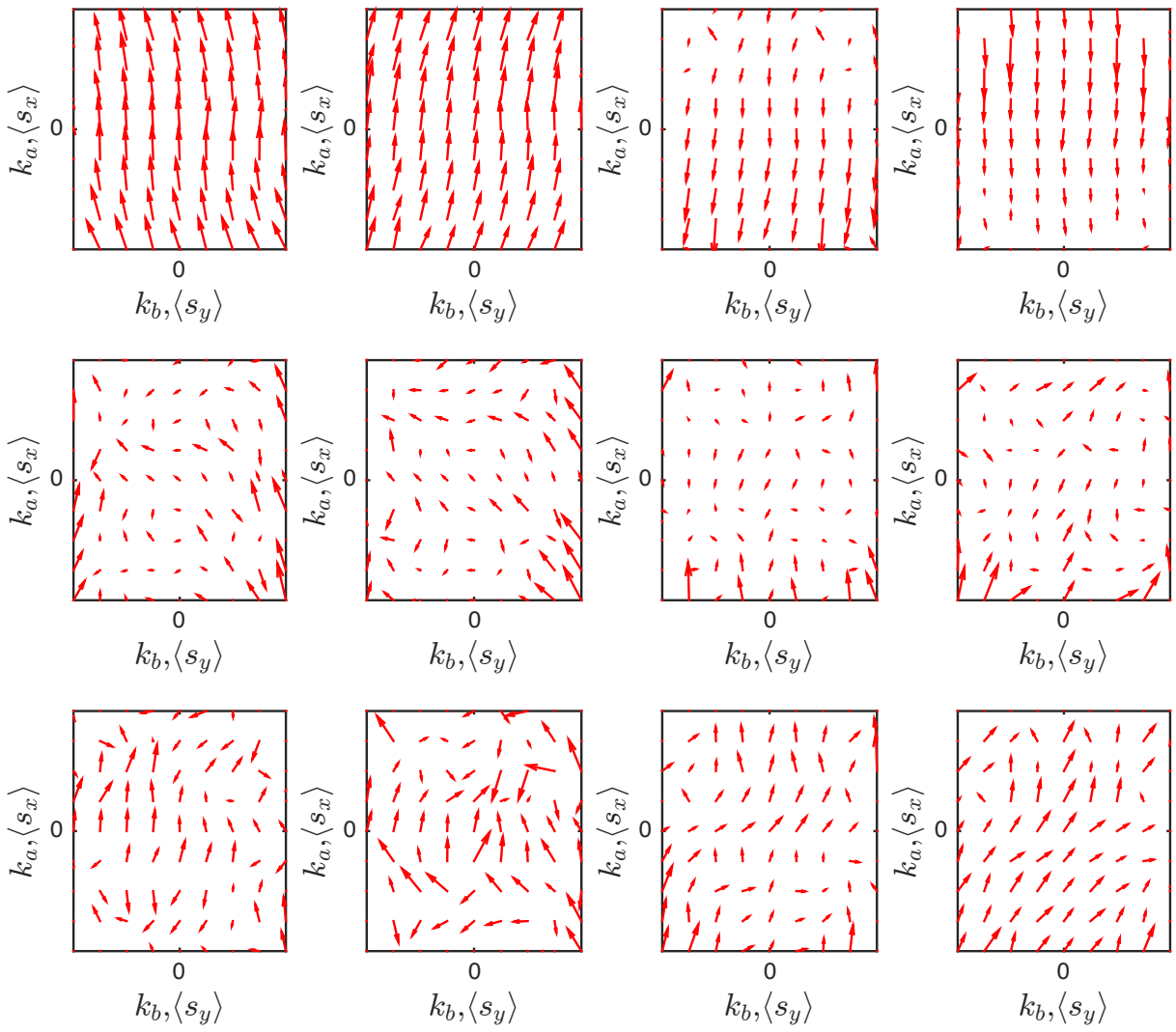

Figure 34: In-plane spin textures in H_1 (fully-relaxed) obtained on a 9×9 mesh centered on the Dirac cone at Γ in reciprocal space for bands around the Fermi level. (From top to bottom) Valence and conduction bands associated with WTe_2; Valence bands in the Dirac cone associated with graphene; Conduction bands in the Dirac cone associated with graphene. The scale investigated here in reciprocal space is 1.5 that considered for all other spin textures. Additionally, a 10^8 times stricter criterion on wavefunction residuals is used.

References

[1] J. J. Sakurai, *Modern quantum mechanics; rev. ed.* Reading, MA: Addison-Wesley, 1994.

[2] M. Dresselhaus, G. Dresselhaus, and A. Jorio, *Group Theory: Application to the Physics of Condensed Matter*. SpringerLink: Springer e-Books, Springer Berlin Heidelberg, 2007.

[3] C. Cohen-Tannoudji, B. Diu, and F. Laloe, *Quantum Mechanics*. No. v. 1 in Quantum Mechanics, Wiley, 1991.

[4] L. D. Landau and E. M. Lifshitz, *Lehrbuch der theoretischen Physik: Quantenmechanik*. Akademie Verlag Berlin, 1971.

[5] Y. A. Bychkov and E. I. Rashba, "Properties of a 2d electron-gas with lifted spectral degeneracy," *Sov. Phys. JETP Lett*, vol. 39, no. 78, 1984.

[6] Y. A. Bychkov and E. I. Rashba, "Oscillatory effects and the magnetic susceptibility of carriers in inversion layers," *Journal of Physics C: Solid State Physics*, vol. 17, pp. 6039–6045, nov 1984.

[7] M. L. Franz, M., *Topological Insulators*. Burlington: Elsevier Science, 2013.

[8] G. M. Graf and M. Porta, "Bulk-edge correspondence for two-dimensional topological insulators," *Communications in Mathematical Physics*, vol. 324, pp. 851–895, Dec 2013.

[9] J. E. Moore, "The birth of topological insulators," *Nature*, vol. 464, pp. 194–198, Mar. 2010.

[10] C. Brüne, A. Roth, H. Buhmann, E. M. Hankiewicz, L. W. Molenkamp, J. Maciejko, X.-L. Qi, and S.-C. Zhang, "Spin polarization of the quantum spin Hall edge states," *Nature Physics*, vol. 8, pp. 485–490, May 2012.

[11] B. A. Bernevig and T. L. Hughes, *Topological Insulators and Topological Superconductors*. Princeton University Press, student edition ed., 2013.

[12] M. König, S. Wiedmann, C. Brüne, A. Roth, H. Buhmann, L. W. Molenkamp, X.-L. Qi, and S.-C. Zhang, "Quantum spin Hall insulator state in HgTe quantum wells," *Science*, vol. 318, no. 5851, pp. 766–770, 2007.

[13] B. A. Bernevig, T. L. Hughes, and S.-C. Zhang, "Quantum spin Hall effect and topological phase transition in HgTe quantum wells," *Science*, vol. 314, no. 5806, pp. 1757–1761, 2006.

[14] L. Du, I. Knez, G. Sullivan, and R.-R. Du, "Robust helical edge transport in gated InAs/GaSb bilayers," *Phys. Rev. Lett.*, vol. 114, p. 096802, Mar 2015.

[15] C. Liu, T. L. Hughes, X.-L. Qi, K. Wang, and S.-C. Zhang, "Quantum spin Hall effect in inverted type-II semiconductors," *Phys. Rev. Lett.*, vol. 100, p. 236601, Jun 2008.

[16] F. Reis, G. Li, L. Dudy, M. Bauernfeind, S. Glass, W. Hanke, R. Thomale, J. Schäfer, and R. Claessen, "Bismuthene on a SiC substrate: A candidate for a high-temperature quantum spin Hall material," *Science*, vol. 357, no. 6348, pp. 287–290, 2017.

[17] B. Rasche, A. Isaeva, M. Ruck, S. Borisenko, V. Zabolotnyy, B. Büchner, K. Koepernik, C. Ortix, M. Richter, and J. van den Brink, "Stacked topological insulator built from bismuth-based graphene sheet analogues," *Nature Materials*, vol. 12, pp. 422–425, Mar. 2013.

[18] C. Pauly, B. Rasche, K. Koepernik, M. Liebmann, M. Pratzer, M. Richter, J. Kellner, M. Eschbach, B. Kaufmann, L. Plucinski, C. M. Schneider, M. Ruck, J. van den Brink, and M. Morgenstern, "Subnanometre-wide electron channels protected by topology," *Nature Physics*, vol. 11, pp. 338–343, Mar. 2015.

[19] L. Fu and C. L. Kane, "Superconducting proximity effect and Majorana fermions at the surface of a topological insulator," *Phys. Rev. Lett.*, vol. 100, p. 096407, Mar 2008.

[20] M. Z. Hasan and C. L. Kane, "Colloquium: Topological insulators," *Rev. Mod. Phys.*, vol. 82, pp. 3045–3067, Nov 2010.

[21] X.-L. Qi and S.-C. Zhang, "Topological insulators and superconductors," *Rev. Mod. Phys.*, vol. 83, pp. 1057–1110, Oct 2011.

[22] J. Alicea, "New directions in the pursuit of Majorana fermions in solid state systems," *Reports on Progress in Physics*, vol. 75, p. 076501, jun 2012.

[23] S. D. Sarma, M. Freedman, and C. Nayak, "Majorana zero modes and topological quantum computation," *npj Quantum Information*, vol. 1, Oct. 2015.

[24] C. L. Kane and E. J. Mele, "Quantum spin Hall effect in graphene," *Phys. Rev. Lett.*, vol. 95, p. 226801, Nov 2005.

[25] M. Gmitra, S. Konschuh, C. Ertler, C. Ambrosch-Draxl, and J. Fabian, "Band-structure topologies of graphene: Spin-orbit coupling effects from first principles," *Phys. Rev. B*, vol. 80, p. 235431, Dec 2009.

[26] N. Tombros, C. Jozsa, M. Popinciuc, H. T. Jonkman, and B. J. van Wees, "Electronic spin transport and spin precession in single graphene layers at room temperature," *Nature*, vol. 448, pp. 571–574, July 2007.

[27] W. Han, K. Pi, K. M. McCreary, Y. Li, J. J. I. Wong, A. G. Swartz, and R. K. Kawakami, "Tunneling spin injection into single layer graphene," *Phys. Rev. Lett.*, vol. 105, p. 167202, Oct 2010.

[28] P. J. Zomer, M. H. D. Guimarães, N. Tombros, and B. J. van Wees, "Long-distance spin transport in high-mobility graphene on hexagonal boron nitride," *Phys. Rev. B*, vol. 86, p. 161416, Oct 2012.

[29] T.-Y. Yang, J. Balakrishnan, F. Volmer, A. Avsar, M. Jaiswal, J. Samm, S. R. Ali, A. Pachoud, M. Zeng, M. Popinciuc, G. Güntherodt, B. Beschoten, and B. Özyilmaz, "Observation of long spin-relaxation times in bilayer graphene at room temperature," *Phys. Rev. Lett.*, vol. 107, p. 047206, Jul 2011.

[30] W. Han and R. K. Kawakami, "Spin relaxation in single-layer and bilayer graphene," *Phys. Rev. Lett.*, vol. 107, p. 047207, Jul 2011.

[31] Y. Yao, F. Ye, X.-L. Qi, S.-C. Zhang, and Z. Fang, "Spin-orbit gap of graphene: First-principles calculations," *Phys. Rev. B*, vol. 75, p. 041401, Jan 2007.

[32] T. Wakamura, F. Reale, P. Palczynski, M. Q. Zhao, A. T. C. Johnson, S. Guéron, C. Mattevi, A. Ouerghi, and H. Bouchiat, "Spin-orbit interaction induced in graphene by transition metal dichalcogenides," *Phys. Rev. B*, vol. 99, p. 245402, Jun 2019.

[33] D. H. Keum, S. Cho, J. H. Kim, D.-H. Choe, H.-J. Sung, M. Kan, H. Kang, J.-Y. Hwang, S. W. Kim, H. Yang, K. J. Chang, and Y. H. Lee, "Bandgap opening in few-layered monoclinic $MoTe_2$," *Nature Physics*, vol. 11, pp. 482–486, May 2015.

[34] S. Manzeli, D. Ovchinnikov, D. Pasquier, O. V. Yazyev, and A. Kis, "2d transition metal dichalcogenides," *Nature Reviews Materials*, vol. 2, June 2017.

[35] X. Qian, J. Liu, L. Fu, and J. Li, "Quantum spin Hall effect in two-dimensional transition metal dichalcogenides," *Science*, vol. 346, no. 6215, pp. 1344–1347, 2014.

[36] F. Y. Bruno, A. Tamai, Q. S. Wu, I. Cucchi, C. Barreteau, A. de la Torre, S. McKeown Walker, S. Riccò, Z. Wang, T. K. Kim, M. Hoesch, M. Shi, N. C. Plumb, E. Giannini, A. A. Soluyanov, and F. Baumberger, "Observation of large topologically trivial fermi arcs in the candidate type-II Weyl semimetal WTe_2," *Phys. Rev. B*, vol. 94, p. 121112, Sep 2016.

[37] P. Chen, W. W. Pai, Y.-H. Chan, W.-L. Sun, C.-Z. Xu, D.-S. Lin, M. Y. Chou, A.-V. Fedorov, and T.-C. Chiang, "Large quantum-spin-Hall gap in single-layer 1T' WSe_2," *Nature Communications*, vol. 9, May 2018.

[38] M. M. Ugeda, A. Pulkin, S. Tang, H. Ryu, Q. Wu, Y. Zhang, D. Wong, Z. Pedramrazi, A. Martín-Recio, Y. Chen, F. Wang, Z.-X. Shen, S.-K. Mo, O. V. Yazyev, and M. F. Crommie, "Observation of topologically protected states at crystalline phase boundaries in single-layer WSe_2," *Nature Communications*, vol. 9, Aug. 2018.

[39] D. Xiao, G.-B. Liu, W. Feng, X. Xu, and W. Yao, "Coupled spin and valley physics in monolayers of MoS_2 and other group-VI dichalcogenides," *Phys. Rev. Lett.*, vol. 108, p. 196802, May 2012.

[40] J. H. Garcia, M. Vila, A. W. Cummings, and S. Roche, "Spin transport in graphene/transition metal dichalcogenide heterostructures," *Chem. Soc. Rev.*, vol. 47, pp. 3359–3379, 2018.

[41] D.-H. Choe, H.-J. Sung, and K. J. Chang, "Understanding topological phase transition in monolayer transition metal dichalcogenides," *Phys. Rev. B*, vol. 93, p. 125109, Mar 2016.

[42] T. Völkl, T. Rockinger, M. Drienovsky, K. Watanabe, T. Taniguchi, D. Weiss, and J. Eroms, "Magnetotransport in heterostructures of transition metal dichalcogenides and graphene," *Phys. Rev. B*, vol. 96, p. 125405, Sep 2017.

[43] B. Yang, M.-F. Tu, J. Kim, Y. Wu, H. Wang, J. Alicea, R. Wu, M. Bockrath, and J. Shi, "Tunable spin–orbit coupling and symmetry-protected edge states in graphene/WS_2," *2D Materials*, vol. 3, p. 031012, sep 2016.

[44] Z. Wang, D.-K. Ki, J. Y. Khoo, D. Mauro, H. Berger, L. S. Levitov, and A. F. Morpurgo, "Origin and magnitude of 'designer' spin-orbit interaction in graphene on semiconducting transition metal dichalcogenides," *Phys. Rev. X*, vol. 6, p. 041020, Oct 2016.

[45] J. H. Garcia, A. W. Cummings, and S. Roche, "Spin Hall effect and weak antilocalization in graphene/transition metal dichalcogenide heterostructures," *Nano Letters*, vol. 17, pp. 5078–5083, July 2017.

[46] A. Avsar, J. Y. Tan, T. Taychatanapat, J. Balakrishnan, G. Koon, Y. Yeo, J. Lahiri, A. Carvalho, A. S. Rodin, E. O'Farrell, G. Eda, A. H. C. Neto, and B. Özyilmaz, "Spin–orbit proximity effect in graphene," *Nature Communications*, vol. 5, Sept. 2014.

[47] Z. Wang, D. Ki, H. Chen, H. Berger, A. H. MacDonald, and A. F. Morpurgo, "Strong interface-induced spin–orbit interaction in graphene on WS_2," *Nature Communications*, vol. 6, Sept. 2015.

[48] Z. Wang, D.-K. Ki, J. Y. Khoo, D. Mauro, H. Berger, L. S. Levitov, and A. F. Morpurgo, "Origin and magnitude of 'designer' spin-orbit interaction in graphene on semiconducting transition metal dichalcogenides," *Phys. Rev. X*, vol. 6, p. 041020, Oct 2016.

[49] B. Yang, M.-F. Tu, J. Kim, Y. Wu, H. Wang, J. Alicea, R. Wu, M. Bockrath, and J. Shi, "Tunable spin–orbit coupling and symmetry-protected edge states in graphene/WS_2," *2D Materials*, vol. 3, p. 031012, sep 2016.

[50] T. Völkl, T. Rockinger, M. Drienovsky, K. Watanabe, T. Taniguchi, D. Weiss, and J. Eroms, "Magnetotransport in heterostructures of transition metal dichalcogenides and graphene," *Phys. Rev. B*, vol. 96, p. 125405, Sep 2017.

[51] M. Offidani, M. Milletarì, R. Raimondi, and A. Ferreira, "Optimal charge-to-spin conversion in graphene on transition-metal dichalcogenides," *Phys. Rev. Lett.*, vol. 119, p. 196801, Nov 2017.

[52] S. Zihlmann, A. W. Cummings, J. H. Garcia, M. Kedves, K. Watanabe, T. Taniguchi, C. Schönenberger, and P. Makk, "Large spin relaxation anisotropy and valley-zeeman spin-orbit coupling in WSe_2/graphene/h-BN heterostructures," *Phys. Rev. B*, vol. 97, p. 075434, Feb 2018.

[53] A. W. Cummings, J. H. Garcia, J. Fabian, and S. Roche, "Giant spin lifetime anisotropy in graphene induced by proximity effects," *Phys. Rev. Lett.*, vol. 119, p. 206601, Nov 2017.

[54] T. S. Ghiasi, J. Ingla-Aynés, A. A. Kaverzin, and B. J. van Wees, "Large proximity-induced spin lifetime anisotropy in transition-metal dichalcogenide/graphene heterostructures," *Nano Letters*, vol. 17, pp. 7528–7532, Nov. 2017.

[55] L. A. Benítez, J. F. Sierra, W. S. Torres, A. Arrighi, F. Bonell, M. V. Costache, and S. O. Valenzuela, "Strongly anisotropic spin relaxation in graphene–transition metal dichalcogenide heterostructures at room temperature," *Nature Physics*, vol. 14, pp. 303–308, Dec. 2017.

[56] A. W. Cummings, J. H. Garcia, J. Fabian, and S. Roche, "Giant spin lifetime anisotropy in graphene induced by proximity effects," *Phys. Rev. Lett.*, vol. 119, p. 206601, Nov 2017.

[57] M. Gmitra and J. Fabian, "Graphene on transition-metal dichalcogenides: A platform for proximity spin-orbit physics and optospintronics," *Phys. Rev. B*, vol. 92, p. 155403, Oct 2015.

[58] Y. K. Luo, J. Xu, T. Zhu, G. Wu, E. J. McCormick, W. Zhan, M. R. Neupane, and R. K. Kawakami, "Opto-valleytronic spin injection in monolayer MoS_2/few-layer graphene hybrid spin valves," *Nano Letters*, vol. 17, pp. 3877–3883, May 2017.

[59] A. Avsar, D. Unuchek, J. Liu, O. L. Sanchez, K. Watanabe, T. Taniguchi, B. Özyilmaz, and A. Kis, "Optospintronics in graphene via proximity coupling," *ACS Nano*, vol. 11, pp. 11678–11686, Nov. 2017.

[60] T. Frank, P. Högl, M. Gmitra, D. Kochan, and J. Fabian, "Protected pseudohelical edge states in Z_2-trivial proximitized graphene," *Phys. Rev. Lett.*, vol. 120, p. 156402, Apr 2018.

[61] M. Gmitra, D. Kochan, P. Högl, and J. Fabian, *Proximity Spin-orbit Coupling Physics of Graphene in Transition-metal Dichalcogenides*, pp. 18–39.

[62] Y. Li and M. Koshino, "Twist-angle dependence of the proximity spin-orbit coupling in graphene on transition-metal dichalcogenides," *Phys. Rev. B*, vol. 99, p. 075438, Feb 2019.

[63] S.-Y. Xu, Q. Ma, H. Shen, V. Fatemi, S. Wu, T.-R. Chang, G. Chang, A. M. M. Valdivia, C.-K. Chan, Q. D. Gibson, J. Zhou, Z. Liu, K. Watanabe, T. Taniguchi, H. Lin, R. J. Cava, L. Fu, N. Gedik, and P. Jarillo-Herrero, "Electrically switchable Berry curvature dipole in the monolayer topological insulator WTe_2," *Nature Physics*, vol. 14, no. 9, pp. 900–906, 2018.

[64] F. Zheng, C. Cai, S. Ge, X. Zhang, X. Liu, H. Lu, Y. Zhang, J. Qiu, T. Taniguchi, K. Watanabe, S. Jia, J. Qi, J.-H. Chen, D. Sun, and J. Feng, "On the quantum spin Hall gap of monolayer 1T'-WTe_2," *Advanced Materials*, vol. 28, no. 24, pp. 4845–4851, 2016.

[65] S. Tang, C. Zhang, D. Wong, Z. Pedramrazi, H.-Z. Tsai, C. Jia, B. Moritz, M. Claassen, H. Ryu, S. Kahn, J. Jiang, H. Yan, M. Hashimoto, D. Lu, R. G. Moore, C.-C. Hwang, C. Hwang, Z. Hussain, Y. Chen, M. M. Ugeda, Z. Liu, X. Xie, T. P. Devereaux, M. F. Crommie, S.-K. Mo, and Z.-X. Shen, "Quantum spin Hall state in monolayer 1T'-WTe_2," *Nature Physics*, vol. 13, pp. 683 EP –, Jun 2017.

[66] Z. Fei, T. Palomaki, S. Wu, W. Zhao, X. Cai, B. Sun, P. Nguyen, J. Finney, X. Xu, and D. H. Cobden, "Edge conduction in monolayer WTe_2," *Nature Physics*, vol. 13, pp. 677 EP –, Apr 2017.

[67] F. Zheng, C. Cai, S. Ge, X. Zhang, X. Liu, H. Lu, Y. Zhang, J. Qiu, T. Taniguchi, K. Watanabe, S. Jia, J. Qi, J.-H. Chen, D. Sun, and J. Feng, "On the quantum spin Hall gap of monolayer 1T'-WTe_2," *Advanced Materials*, vol. 28, no. 24, pp. 4845–4851, 2016.

[68] S. Wu, V. Fatemi, Q. D. Gibson, K. Watanabe, T. Taniguchi, R. J. Cava, and P. Jarillo-Herrero, "Observation of the quantum spin Hall effect up to 100 kelvin in a monolayer crystal," *Science*, vol. 359, no. 6371, pp. 76–79, 2018.

[69] Z.-Y. Jia, Y.-H. Song, X.-B. Li, K. Ran, P. Lu, H.-J. Zheng, X.-Y. Zhu, Z.-Q. Shi, J. Sun, J. Wen, D. Xing, and S.-C. Li, "Direct visualization of a two-dimensional topological insulator in the single-layer 1T' WTe_2," *Phys. Rev. B*, vol. 96, p. 041108, Jul 2017.

[70] S. e. a. Wu, "Observation of topological insulating and superconducting ground states of monolayer WTe_2.," *Bull. Am. Phys. Soc.*, 2018.

[71] Y. Shi, J. Kahn, B. Niu, Z. Fei, B. Sun, X. Cai, B. A. Francisco, D. Wu, Z.-X. Shen, X. Xu, D. H. Cobden, and Y.-T. Cui, "Imaging quantum spin Hall edges in monolayer WTe_2," *Science Advances*, vol. 5, no. 2, 2019.

[72] M. K. Jana, A. Singh, D. J. Late, C. R. Rajamathi, K. Biswas, C. Felser, U. V. Waghmare, and C. N. R. Rao, "A combined experimental and theoretical study of the structural, electronic and vibrational properties of bulk and few-layer t_d-WTe_2," *Journal of Physics: Condensed Matter*, vol. 27, p. 285401, jun 2015.

[73] Y.-H. Song, Z.-Y. Jia, D. Zhang, X.-Y. Zhu, Z.-Q. Shi, H. Wang, L. Zhu, Q.-Q. Yuan, H. Zhang, D.-Y. Xing, and S.-C. Li, "Observation of coulomb gap in the quantum spin Hall candidate single-layer 1T'-WTe_2," *Nature Communications*, vol. 9, oct 2018.

[74] E. Torun, H. Sahin, S. Cahangirov, A. Rubio, and F. M. Peeters, "Anisotropic electronic, mechanical, and optical properties of monolayer WTe_2," *Journal of Applied Physics*, vol. 119, no. 7, p. 074307, 2016.

[75] H. Xiang, B. Xu, J. Liu, Y. Xia, H. Lu, J. Yin, and Z. Liu, "Quantum spin Hall insulator phase in monolayer WTe_2 by uniaxial strain," *AIP Advances*, vol. 6, no. 9, p. 095005, 2016.

[76] S. Ok, L. Muechler, D. Di Sante, G. Sangiovanni, R. Thomale, and T. Neupert, "Custodial glide symmetry of quantum spin Hall edge modes in monolayer WTe_2," *Phys. Rev. B*, vol. 99, p. 121105, Mar 2019.

[77] D. Rhodes, S. Das, Q. R. Zhang, B. Zeng, N. R. Pradhan, N. Kikugawa, E. Manousakis, and L. Balicas, "Role of spin-orbit coupling and evolution of the electronic structure of WTe_2 under an external magnetic field," *Phys. Rev. B*, vol. 92, p. 125152, Sep 2015.

[78] L.-k. Shi and J. C. W. Song, "Symmetry, spin-texture, and tunable quantum geometry in a WTe_2 monolayer," *Phys. Rev. B*, vol. 99, p. 035403, Jan 2019.

[79] D. Rhodes, N. F. Yuan, Y. Jung, A. Antony, H. Wang, B. Kim, Y.-c. Chiu, T. Taniguchi, K. Watanabe, K. Barmak, L. Balicas, C. R. Dean, X. Qian, L. Fu, A. N. Pasupathy, and J. Hone, "Enhanced Superconductivity in Monolayer T_d-$MoTe_2$ with Tilted Ising Spin Texture," *arXiv e-prints*, p. arXiv:1905.06508, May 2019.

[80] S. Bertolazzi, J. Brivio, and A. Kis, "Stretching and breaking of ultrathin MoS_2," *ACS Nano*, vol. 5, pp. 9703–9709, Nov. 2011.

[81] E. Sajadi, T. Palomaki, Z. Fei, W. Zhao, P. Bement, C. Olsen, S. Luescher, X. Xu, J. A. Folk, and D. H. Cobden, "Gate-induced superconductivity in a monolayer topological insulator," *Science*, vol. 362, no. 6417, pp. 922–925, 2018.

[82] V. Fatemi, S. Wu, Y. Cao, L. Bretheau, Q. D. Gibson, K. Watanabe, T. Taniguchi, R. J. Cava, and P. Jarillo-Herrero, "Electrically tunable low-density superconductivity in a monolayer topological insulator," *Science*, vol. 362, no. 6417, pp. 926–929, 2018.

[83] A. W. Tsen, B. Hunt, Y. D. Kim, Z. J. Yuan, S. Jia, R. J. Cava, J. Hone, P. Kim, C. R. Dean, and A. N. Pasupathy, "Nature of the quantum metal in a two-dimensional crystalline superconductor," *Nature Physics*, vol. 12, pp. 208–212, Dec. 2015.

[84] X. Xi, Z. Wang, W. Zhao, J.-H. Park, K. T. Law, H. Berger, L. Forró, J. Shan, and K. F. Mak, "Ising pairing in superconducting NbSe2 atomic layers," *Nature Physics*, vol. 12, pp. 139–143, Nov. 2015.

[85] L. J. Li, E. C. T. O'Farrell, K. P. Loh, G. Eda, B. Özyilmaz, and A. H. C. Neto, "Controlling many-body states by the electric-field effect in a two-dimensional material," *Nature*, vol. 529, pp. 185–189, Dec. 2015.

[86] Y. Fu, E. Liu, H. Yuan, P. Tang, B. Lian, G. Xu, J. Zeng, Z. Chen, Y. Wang, W. Zhou, K. Xu, A. Gao, C. Pan, M. Wang, B. Wang, S.-C. Zhang, Y. Cui, H. Y. Hwang, and F. Miao, "Gated tuned superconductivity and phonon softening in monolayer and bilayer MoS_2," *npj Quantum Materials*, vol. 2, Sept. 2017.

[87] Y. Saito, T. Nojima, and Y. Iwasa, "Gate-induced superconductivity in two-dimensional atomic crystals," *Superconductor Science and Technology*, vol. 29, p. 093001, July 2016.

[88] K. Ueno, S. Nakamura, H. Shimotani, A. Ohtomo, N. Kimura, T. Nojima, H. Aoki, Y. Iwasa, and M. Kawasaki, "Electric-field-induced superconductivity in an insulator," *Nature Materials*, vol. 7, pp. 855–858, Oct. 2008.

[89] J. M. Lu, O. Zheliuk, I. Leermakers, N. F. Q. Yuan, U. Zeitler, K. T. Law, and J. T. Ye, "Evidence for two-dimensional ising superconductivity in gated MoS_2," *Science*, vol. 350, pp. 1353–1357, Nov. 2015.

[90] R. A. Klemm, "Pristine and intercalated transition metal dichalcogenide superconductors," *Physica C: Superconductivity and its Applications*, vol. 514, pp. 86–94, July 2015.

[91] X.-C. Pan, X. Chen, H. Liu, Y. Feng, Z. Wei, Y. Zhou, Z. Chi, L. Pi, F. Yen, F. Song, X. Wan, Z. Yang, B. Wang, G. Wang, and Y. Zhang, "Pressure-driven dome-shaped superconductivity and electronic structural evolution in tungsten ditelluride," *Nature Communications*, vol. 6, jul 2015.

[92] D. Kang, Y. Zhou, W. Yi, C. Yang, J. Guo, Y. Shi, S. Zhang, Z. Wang, C. Zhang, S. Jiang, A. Li, K. Yang, Q. Wu, G. Zhang, L. Sun, and Z. Zhao, "Superconductivity emerging from a suppressed large magnetoresistant state in tungsten ditelluride," *Nature Communications*, vol. 6, jul 2015.

[93] N. Nagaosa, J. Sinova, S. Onoda, A. H. MacDonald, and N. P. Ong, "Anomalous Hall effect," *Rev. Mod. Phys.*, vol. 82, pp. 1539–1592, May 2010.

[94] M. N. Ali, J. Xiong, S. Flynn, J. Tao, Q. D. Gibson, L. M. Schoop, T. Liang, N. Haldolaarachchige, M. Hirschberger, N. P. Ong, and R. J. Cava, "Large, non-saturating magnetoresistance in WTe_2," *Nature*, vol. 514, pp. 205–208, Sept. 2014.

[95] L. Wang, I. Gutiérrez-Lezama, C. Barreteau, N. Ubrig, E. Giannini, and A. F. Morpurgo, "Tuning magnetotransport in a compensated semimetal at the atomic scale," *Nature Communications*, vol. 6, Nov. 2015.

[96] L. Hu, L. Kang, J. Yang, B. Huang, and F. Liu, "Significantly enhanced magnetoresistance in monolayer WTe_2 via heterojunction engineering: a first-principles study," *Nanoscale*, vol. 10, pp. 22231–22236, 2018.

[97] D. MacNeill, G. M. Stiehl, M. H. D. Guimaraes, R. A. Buhrman, J. Park, and D. C. Ralph, "Control of spin-orbit torques through crystal symmetry in WTe_2/ferromagnet bilayers," *Nature Physics*, vol. 13, pp. 300 EP –, Nov 2016. Article.

[98] Z. Fei, W. Zhao, T. A. Palomaki, B. Sun, M. K. Miller, Z. Zhao, J. Yan, X. Xu, and D. H. Cobden, "Ferroelectric switching of a two-dimensional metal," *Nature*, vol. 560, pp. 336–339, July 2018.

[99] X. Gonze, F. Jollet, F. Abreu Araujo, D. Adams, B. Amadon, T. Applencourt, C. Audouze, J.-M. Beuken, J. Bieder, A. Bokhanchuk, E. Bousquet, F. Bruneval, D. Caliste, M. Côté, F. Dahm, F. Da Pieve, M. Delaveau, M. Di Gennaro, B. Dorado, C. Espejo, G. Geneste, L. Genovese, A. Gerossier, M. Giantomassi, Y. Gillet, D. Hamann, L. He, G. Jomard, J. Laflamme Janssen, S. Le Roux, A. Levitt, A. Lherbier, F. Liu, I. Lukačević, A. Martin, C. Martins, M. Oliveira, S. Poncé, Y. Pouillon, T. Rangel, G.-M. Rignanese, A. Romero, B. Rousseau, O. Rubel, A. Shukri, M. Stankovski, M. Torrent, M. Van Setten, B. Van Troeye, M. Verstraete, D. Waroquiers, J. Wiktor, B. Xu, A. Zhou, and J. Zwanziger, "Recent developments in the ABINIT software package," *Comput. Phys. Commun.*, vol. 205, pp. 106–131, August 2016.

[100] J. P. Perdew, K. Burke, and M. Ernzerhof, "Generalized gradient approximation made simple," *Phys. Rev. Lett.*, vol. 77, pp. 3865–3868, Oct 1996.

[101] J. Heyd, G. E. Scuseria, and M. Ernzerhof, "Hybrid functionals based on a screened coulomb potential," *The Journal of Chemical Physics*, vol. 118, no. 18, pp. 8207–8215, 2003.

[102] S. Grimme, J. Antony, S. Ehrlich, and H. Krieg, "A consistent and accurate ab initio parametrization of density functional dispersion correction (DFT-d) for the 94 elements h-pu," *The Journal of Chemical Physics*, vol. 132, p. 154104, Apr. 2010.

[103] I. Hamada, "van der waals density functional made accurate," *Phys. Rev. B*, vol. 89, p. 121103, Mar 2014.

[104] B. Van Troeye, M. Torrent, and X. Gonze, "Interatomic force constants including the DFT-d dispersion contribution," *Phys. Rev. B*, vol. 93, p. 144304, April 2016.

[105] M. Giantomassi, "Abipy." `https://github.com/gmatteo/abipy`, consulted July 2019.

[106] "The *cut3d* utility." `https://docs.abinit.org/guide/cut3d/`, consulted July 2019.

[107] S. P. Ong, W. D. Richards, A. Jain, G. Hautier, M. Kocher, S. Cholia, D. Gunter, V. L. Chevrier, K. A. Persson, and G. Ceder, "Python materials genomics (pymatgen): A robust, open-source python library for materials analysis," *Computational Materials Science*, vol. 68, pp. 314–319, Feb. 2013.

[108] A. Mar, S. Jobic, and J. A. Ibers, "Metal-metal vs tellurium-tellurium bonding in WTe_2 and its ternary variants $TaIrTe_4$ and $NbIrTe_4$," *Journal of the American Chemical Society*, vol. 114, pp. 8963–8971, Nov. 1992.

[109] B. E. Brown, "The crystal structures of WTe_2 and high-temperature $MoTe_2$," *Acta Crystallographica*, vol. 20, pp. 268–274, feb 1966.

[110] H.-J. Kim, S.-H. Kang, I. Hamada, and Y.-W. Son, "Origins of the structural phase transitions in $mote_2$ and wte_2," *Phys. Rev. B*, vol. 95, p. 180101, May 2017.

[111] E. J. Sie, C. M. Nyby, C. D. Pemmaraju, S. J. Park, X. Shen, J. Yang, M. C. Hoffmann, B. K. Ofori-Okai, R. Li, A. H. Reid, S. Weathersby, E. Mannebach, N. Finney, D. Rhodes, D. Chenet, A. Antony, L. Balicas, J. Hone, T. P. Devereaux, T. F. Heinz, X. Wang, and A. M. Lindenberg, "An ultrafast symmetry switch in a Weyl semimetal," *Nature*, vol. 565, pp. 61–66, Jan. 2019.

[112] S. Thirupathaiah, R. Jha, B. Pal, J. S. Matias, P. K. Das, I. Vobornik, R. A. Ribeiro, and D. D. Sarma, "Temperature-independent band structure of WTe_2 as observed from angle-resolved photoemission spectroscopy," *Phys. Rev. B*, vol. 96, p. 165149, Oct 2017.

[113] M. N. Ali, J. Xiong, S. Flynn, J. Tao, Q. D. Gibson, L. M. Schoop, T. Liang, N. Haldolaarachchige, M. Hirschberger, N. P. Ong, and R. J. Cava, "Large, non-saturating magnetoresistance in WTe_2," *Nature*, vol. 514, pp. 205–208, sep 2014.

[114] A. A. Soluyanov, D. Gresch, Z. Wang, Q. Wu, M. Troyer, X. Dai, and B. A. Bernevig, "Type-II Weyl semimetals," *Nature*, vol. 527, pp. 495–498, nov 2015.

[115] P. K. Das, D. D. Sante, I. Vobornik, J. Fujii, T. Okuda, E. Bruyer, A. Gyenis, B. E. Feldman, J. Tao, R. Ciancio, G. Rossi, M. N. Ali, S. Picozzi, A. Yadzani, G. Panaccione, and R. J. Cava, "Layer-dependent quantum cooperation of electron and hole states in the anomalous semimetal WTe_2," *Nature Communications*, vol. 7, Feb. 2016.

[116] R. Saito, G. Dresselhaus, and M. Dresselhaus, *Physical Properties of Carbon Nanotubes*. Imperial College Press, 1998.

[117] "Hirshfeld charges." https://www.tcm.phy.cam.ac.uk/castep/documentation/WebHelp/content/modules/castep/thcastephirshfeld.html, consulted June 2019.

UNIVERSITÉ CATHOLIQUE DE LOUVAIN
École polytechnique de Louvain
Rue Archimède, 1 bte L6.11.01, 1348 Louvain-la-Neuve, Belgique | **www.uclouvain.be/epl**